der Bundeswehr
Universität München

Fakultät für Luft- und Raumfahrttechnik
Institut für Angewandte Physik und Messtechnik

Improvement of the Pulsed Low Energy Positron System (PLEPS) for complex problems in materials science

Dissertation of Luca Ravelli

Improvement of the Pulsed Low Energy Positron System (PLEPS) for complex problems in materials science

M. Sc. Ravelli Luca

Vollständiger Abdruck der von der Fakultät für Luft- und Raumfahrttechnik der Universität der Bundeswehr München zur Erlangung des akademischen Grades eines

Doktors der Naturwissenschaften (Dr. rer. nat.)

genehmigten Dissertation.

Gutachter/Gutachterin: 1. Prof. Dr. rer. nat. G. Dollinger
2. Prof. R. S. Brusa

Die Dissertation wurde am 14.03.2014 bei der Universität der Bundeswehr München eingereicht und durch die Fakultät für Luft- und Raumfahrttechnik am 19.03.2014 angenommen.
Die mündliche Prüfung fand am 29.04.2014 statt.

Abstract

This thesis concerns the application and the improvement of the Pulsed Low Energy Positron System (PLEPS) at the high intensity positron source NEPOMUC at the Munich research reactor FRM-II. This system is used for the defect study in complex materials.

Positrons are the ideal probe for non-destructive investigations of vacancy-like defects in matter. The combination of positron lifetime spectroscopy with a pulsed, monochromatic positron beam of variable energy conveys information on the type and the concentration of defects down to the sub-ppm range and their depth-profile with nm resolution.

Defect structures in two materials were investigated with PLEPS for this thesis. First, we studied strontium titanate (STO), which is a material of great relevance in modern oxide electronics. The cation vacancies (strontium and titanium vacancies, V_{Sr} and V_{Ti}, respectively) were identified in STO films deposited by Pulsed Laser Deposition (PLD). It was also shown, that in commercially available STO substrates only titanium vacancies with a concentration of (1.26 ± 0.16) ppm could be detected and that upon annealing in the same conditions as for the PLD procedure a 400 nm thick layer of titanium - oxygen divacancies $V_{\mathrm{Ti-O}}$ was introduced. The second investigation was performed in permanently densified silica glasses. In combination with XRD measurements the structure evolution upon densification was analyzed. In particular, it was demonstrated that the average inter-tetrahedral void radius measured with PLEPS permits to predict the shift of the first sharp diffraction peak of the static structure factor as a function of the density.

In the second part of this work, from the experience gained with PLEPS in the course of this thesis, the limits of the apparatus were analyzed, measures to improve the quality of the positron lifetime spectra measured with PLEPS were identified and tested. Comprehensive simulations were performed to understand the structures in the background of the measured lifetime spectra and possible countermeasures were found. Modifications of the pulsing system allowed to *a)* improve the time resolution of PLEPS to about 250 ps, *b)* measure precisely positron lifetime longer than 3 ns, which enhances the capabibility of PLEPS for the determination of free volumes in polymer samples and membranes and *c)* get rid of disturbing structures in the background of the positron lifetime spectra.

Thus, PLEPS in combination with the high intensity positron source NEPOMUC can be considered as the most productive pulsed positron beam for defect depth-profiling in materials currently available world-wide.

Contents

Chapter 1

Introduction

For the development of new materials the knowledge of type, concentration and distribution of open volume defects is of crucial importance. In metals and alloys, many physical properties, *e. g.* the mechanical stability and the strength, are related to the presence and concentration of vacancies, dislocations, vacancy clusters, grain boundaries and precipitates. The conductivity in semiconductors is strongly affected by charged and uncharged defects and in some cases, *e. g.* strontium titanate, the introduction of certain types of defects can even turn an insulator into a good electrical conductor. Open volume defects play a very important role also in disordered materials like polymers and glasses. For example, they affect the mechanical properties in polymers and the permittivity and selectivity of membranes. Furthermore, also the glass transition temperature is related to the size and distribution of the voids in polymers and glasses.

The positron is the ideal probe to detect non - destructively the different kind of open-volume defects in all materials. Due to their positive charge, positrons are extremely sensitive to the lack of ions in the crystal lattice. In particular, positrons can be very efficiently trapped into defects and concentrations in the sub-ppm range can be revealed in metals and semiconductors. After the implantation and diffusion in the sample, the positrons will eventually annihilate with an electron of the crystal, either from the delocalized bulk state or after being trapped in a defect.

The analysis of the annihilation radiation can give information on type, concentration, distribution and chemical environment of the annihilation site. In particular, a broadening of the energy distribution of the 511 keV annihilation gamma quanta is observed. Since after the thermalization process the kinetic energy of the positron is small with respect to the energy of the electrons of the solid, this Doppler shift can only be due to the momentum of the electron annihilating with the positron. As a consequence, with the

Doppler Broadening Spectroscopy (DBS) one can distinguish between annihilations with valence or core electrons and therefore DBS is very sensitive to the presence of defects and their chemical environment. On the other hand, Positron Annihilation Lifetime Spectroscopy (PALS) measures the time between the implantation of the positron in the sample and its annihilation. By accumulating several millions of events a lifetime spectrum, consisting of a sum of different exponential decay functions, is obtained. Since the positron lifetime is correlated to the local electron density at the annihilation site, each defect and every material have a characteristic positron lifetime. The lifetimes and intensities obtained with the decomposition of the lifetime spectrum give information on the defect type and its concentration.

Conventional PALS is performed by depositing a β^+ radioactive source directly onto the sample or in a sandwich configuration. Since the positrons emitted by radioactive source have a broad energy distribution with an end point energy of several hundreds of keV, with this method only bulk samples can be investigated (spatial resolution in the order of mm^3). For this reason, this technique can not be applied to many modern materials science problems, such as defect investigations in subsurface regions, in layered structures, thin films and nano-structured samples. To overcome this limitation, monoenergetic positron beams of variable energy were developed. By varying the positron implantation energy, the mean positron implantation depth can be tuned from the surface down to some microns in depth, allowing the investigation of defect distributions with a depth resolution in the nm range.

Continuous, monochromatic positron beams of variable energy for DBS are nowadays available in many laboratories around the world. To perform PALS, pulsed positron beams are required. In the mid 80's, the development of the Pulsed Low Energy Positron System (PLEPS) started at the Universität der Bundeswehr München with the dissertation of Schödlbauer [1]. Many improvements were accomplished over the years (Willutzki [2],Bauer-Kugelmann [3]). Because of the stringent requirements (time resolution on the order of 100 ps with repetition rates in the MHz range) and the complex interplay of ultra high vacuum technique, high frequency and high voltage, only few similar system existed all over the world. By now only a handful of pulsed beams are in operation [4, 5, 6, 7] and few others are under construction [8, 9]. Due to the low count rate (about 500 counts/s) obtainable with the ^{22}Na laboratory source, in 2007 PLEPS was transfered to the research reactor FRM-II to take advantage of the high intensity positron source NEPOMUC (NEutron-induced POsitron source MUniCh). In this combination, PLEPS is undoubtedly the most advanced and most productive positron lifetime system worldwide. However, a high price had to be paid for this success, because of the new, very demanding challenge to match the stringent requirements

of the pulsing system of PLEPS with the new NEPOMUC beam. In fact, the remoderated NEPOMUC beam has a much higher intensity compared to the laboratory, but at the price of a two times broader energy distribution resulting in worse time resolution (between (260-300) ps compared to 230 ps in the laboratory).

From 2008 to 2010 about 200 depth profiles in about 100 days of operation were measured in cooperation with external users. Two examples of the measurements performed with PLEPS at NEPOMUC were chosen to demonstrate the capabilities of positron annihilation lifetime spectroscopy in combination with a high intensity pulsed positron beam. The first example deals with defects identification in strontium titanate. Many studies can be found in literature about the doping of oxygen vacancies and its effect on the electrical conductivity in this material, but little is known about the cation vacancies (strontium and titanium vacancies). Ohnishi *et al.* [10] showed that varying the laser fluence in Pulsed Laser Deposited strontium titanate films results in deviations in the stoichiometry that can strongly affect the electrical properties of the system. Since the cation vacancies are negatively charged, positrons were the perfect probe for such samples. The investigation on PLD deposited STO films allowed to identify the two cation vacancies [11]. Furthermore, a STO single crystal was analyzed after the same annealing treatment used in the growth of film with PLD.

The second example answers a fundamental question about the structure of disordered systems, specifically the Short and Medium Range Orders in permanently densified silica glasses were investigated with the combination of X-ray diffraction and PALS [12].

During these first years of operation at the high intensity source NEPOMUC some limits of the setup were evidenced:

a) The investigations of free volume in polymers and membranes has increased dramatically in the last decade and the standard 20 ns time window is in some cases not suited for the measurements with long lifetimes.
b) Modern materials are more and more complex and, especially in layered structures or when inhomogeneous defect distribution are present, four lifetime components are not enough to fully describe the system.
c) With the much higher peak-to-background ratio satellite structures due to backscattered positrons appear in the lifetime spectra.

Because of the large demand for PLEPS beam-time from external users, technical improvements had to be accomplished mainly in parallel to the experiments. Between 2011 and 2012 there was a complete shut down of PLEPS because of the upgrade of the NEPOMUC source. During this break

also PLEPS had to be dismantled and only in this period it was possible to complete all the necessary modifications to improve the system.

It was the aim of the present work not only to clarify the reasons for the aforementioned deficiencies of PLEPS, but also to remove them as far as possible.

This thesis is organized as follows:
In chapter 2 an introduction about positrons in general and as a probe for defect investigation in materials science is given. In the first two sections of this chapter we will give an overview on the positron production, from radioactive to high intensity LINAC and reactor based sources, and on positron beams, focusing in particular on pulsed positron beams. Sections 2.3 and 2.4 describe the "fate" of the positrons after the implantation in a solid and the properties of the positron - electron bound state (positronium), respectively. The last section presents the two positron techniques relevant for this work, namely Positron Annihilation Lifetime Spectroscopy (section 2.5.2) and Doppler Broadening Spectroscopy (section 2.5.1).

Chapter 3 describes the Pulsed Low Energy Positron System (PLEPS) and its performance after the installation at the high intensity positron source NEPOMUC at the research reactor FRM2.

Two examples of applications of PLEPS in materials science are described in chapter 4. Specifically, the defect characterization in strontium titanate thin films and bulk crystals are discussed in section 4.1, while the investigation on permanently densified silica glasses is presented in 4.2. A third example is discussed in section 7.2 and concerns samples with long positron lifetimes, in particular a Polymer of Intrinsic Microporosity and Teflon AF ©.

The above mentioned limits of the setup are described in chapter 5 and the countermeasures are discussed in the last two chapters.

Firstly, the simulations of the background structure present in the lifetime spectra measured with PLEPS caused by backscattered positron will be discussed (chapter 6).

Finally, in chapter 7 the constructive improvements of the pulsing system are described. The modifications of the prebuncher and of the main buncher to improve the time resolution are discussed in sections 7.1.1 and 7.1.2, respectively. The extension of the time window together with the results of the first tests and the effect on the analysis of two different polymer systems are shown in section 7.2.

Chapter 2

Positrons in material science

In this chapter we will give an overview of the positrons in matter. A more detailed account may be found in [13, 14].

After the prediction of Dirac [15, 16], the existence of the positron was proved by Anderson [17, 18] by studying cosmic rays with a cloud chamber. Later on it was found that the positron has, within experimental errors, the mass ($m_e = 0.510998917(44)\,\mathrm{MeV}/c^2$) and spin ($s = 1/2$) of the electron, but opposite charge ($q_e = 1.602176462(63) \cdot 10^{-19}\,\mathrm{C}$) and hence magnetic moment. It is stable in vacuum ($\tau > 10^{21}\,\mathrm{y}$), but, since it is the anti-particle of the electron, a positron in matter will annihilate in a finite time. As the annihilation rate depends on the local electron density, the positron lifetime is related to the structure of the crystal and to the presence of defects in it.

The most probable annihilation process is the one via two gamma quanta, since the probability for a three gamma decay is 372 times smaller than for a two gamma decay. From conservation of energy and momentum considerations the two gamma quanta are emitted collinearly with an energy of 511 keV each if both particles are at rest. If this condition is not fulfilled, an angular deviation and also a Doppler shift of the two emitted gamma quanta are observed in the laboratory frame. Since after the thermalization process the kinetic energy of the positron is small with respect to the energy of the electrons of the solid, the angular deviation and the Doppler shift can give information on the momentum of the electron annihilating with the positron.

Under certain circumstances, a positron and an electron can also form a bound state, called positronium. The existence of this "exotic" atom was proposed by Mohorovicic [19] and was observed for the first time by Deutsch [20]. The positronium is similar to an hydrogen atom, but with the proton replaced by a positron. It has two possible states depending on the total spin of the system with very different annihilation characteristics.

In this chapter we will first give an overview on the production of positrons,

on their moderation and on the positron beams (section 2.1).
We will then briefly describe the thermalization and diffusion process after the implantation of a positron in matter and the properties of positronium, in sections 2.3 and 2.4, respectively.
Finally, the two positron techniques relevant for this work, namely Doppler Broadening Spectroscopy (DBS) and Positron Annihilation Lifetime Spectroscopy (PALS), are illustrated (section 2.5).

2.1 Positron production

2.1.1 Radioactive sources

In the beginning, positrons were obtained from radioactive sources, deposited directly onto the sample or used in a sandwich configuration. The disadvantage of this method is that the positrons emitted from radioactive sources have a broad energy distribution and an end–point energy greater than $\approx 500\,\mathrm{keV}$. The characteristics of the most commonly used positron sources are summarized in table 2.1.

Nuclide	Half life	I_{e^+}	$E_{max}\ [keV]$	$E_{av}\ [keV]$	I_γ	$E_\gamma\ [keV]$
^{22}Na	2.60 y	0.898	545.4	215.5	0.999	1275
		0.001	1819.7	835.0		
^{58}Co	70.8 d	0.150	475.2	201.3	0.994	811
^{64}Cu	12.7 h	0.179	652.5	278.1	0.005	1346

Table 2.1: β^+ emitters often used in positron experiments. Half life, positron yield I_{e^+}, end–point energy E_{max}, average energy E_{av}, intensity of the emitted gammas I_γ and corresponding energy E_γ (data from [21])

The implantation profile of positrons emitted by a radioactive source can be described by an exponential function with a characteristic penetration depth α [22]:

$$\alpha \approx 16 \frac{\rho\,[g/cm^3]}{E_{max}^{1.4}\,[MeV]} cm^{-1}\,. \tag{2.1}$$

As an example, equation 2.1 gives a characteristic implantation depth of $110\,\mu m$ in Si and $14\,\mu m$ in W with a ^{22}Na source. As a consequence, only information about the bulk of the target can be obtained.

Moderator	Geometry	Efficiency
W(110)	Reflection	$2 \cdot 10^{-3}$
W	Vanes	$7 \cdot 10^{-4}$
W(100)	Transmission	$6 \cdot 10^{-4}$
W poly	Transmission	$2.6 \cdot 10^{-4}$
Ni(100)	Transmission	$7 \cdot 10^{-4}$
Ni poly	Transmission	$2.5 \cdot 10^{-4}$

Table 2.2: Moderator efficiency for different materials and geometries (from [14])

2.1.2 Positron moderation

The observation of moderated positrons from surfaces by Groce *et al.* [23] opened the possibility of the development of mono-energetic positron beams of variable energy. This finding gave a big boost to the positron methods in materials science, since it allowed not only to investigate bulk samples, but also near surface defects and layered samples.

In the 70's many groups focused their attention on the moderation properties of negative-work-function materials in order to find an efficient moderator with a narrow energy distribution (see [14] for a more detailed description). Many materials (*e. g.* W(110), Ni(100), rare gas solids like Ne) and a large variety of different geometries have been tested. It was shown that positrons are re-emitted from the moderator crystal with a narrow energy distribution centered at some eV (depending on the material, *e. g.* 2.48 eV for W(110)). The spread of this energy distribution is caused only by the thermal energy. In table 2.2 some of the moderator materials/configurations are summarized together with their corresponding efficiency.

2.1.3 High intensity positron sources

In the last decades also reactor and LINAC based sources have been developed. In both cases positrons are produced via pair production using high energy gamma quanta, coming either from the decay of excited nuclear states or from bremsstrahlung radiation, respectively, and a high Z converter, such as W, Pt or Ta. Table 2.3 summarizes some of the available large scale facilities with a high intensity positron source. A brief description of the NEPOMUC (NEutron - induced POsitron source MUniCh) at the Heinz-Maier Leibnitz

(FRM - II) research reactor (Munich) can be found in section 3.1.

Reactor based

Name	Process	Converter	Intensity
NEPOMUC [24]	n - capture in Cd	Pt	$9 \cdot 10^8$
PULSTAR [25]	n - capture in Cd	W	$5 \cdot 10^8$
POSH [26]	fission γ	W	$8 \cdot 10^7$

LINAC based

Name	e^- energy	Repetition rate	Converter	Intensity
KEK [27]	50 MeV	50 Hz	W	$5 \cdot 10^7$
AIST [28]	70 MeV	100 Hz	Ta	$\approx 10^7$
EPOS [29]	40 MeV	13 MHz	W	$5 \cdot 10^8$

Table 2.3: High intensity positron sources at large scale facilities.

2.2 Positron beams

After the positrons are extracted from the moderation stage, a beam can be formed and then guided to the target either in a magnetic or an electrostatic field in order to prevent the increase of the angular spread of the beam. Usually a magnetic transport is preferred, especially if the beam has to be transported over long distances. In this case, a longitudinal magnetic field is created by means of solenoidal coils or a series of Helmholtz coils. For the benefit of the reader a brief account on charged particle motion in electromagnetic fields is given in the next section. It follows closely the treatment found in many standard textbooks, *e. g.* [30, 31].

2.2.1 Motion of particles in electromagnetic fields

Even if the trajectory of a particle of mass m and electric charge q in an electromagnetic field $(\vec{E}, \vec{B})$ can be described by solving the equation of motion

$$\frac{\mathrm{d}\,(m\vec{v})}{\mathrm{dt}} = q \cdot \left[\vec{E} + \frac{\vec{v}}{c} \times \vec{B}\right] , \tag{2.2}$$

it is often more convenient to use the Lagrangian formalism in which the generalized coordinates $q_i(t)$ and $\dot{q}_i(t)$ are used to describe the system. As can be found in many textbooks [31], such a system can be described (in the case of a relativistic particle, $\beta = v/c$) by a Lagrangian $\mathcal{L}$ of the form:

$$\mathcal{L} = m_0 c^2 \left(1 - \sqrt{1-\beta^2}\right) + q\left(\vec{v} \cdot \vec{A} - \Phi\right) . \tag{2.3}$$

Here, $\vec{A}$ and Φ are the magnetic vector potential and the electric potential, respectively. The first term is the Lagrangian of the free particle and the second one describes the interaction of the particle with the electromagnetic field. The trajectories can be obtained by solving the Euler – Lagrange equation:

$$\frac{\mathrm{d}}{\mathrm{dt}}\left(\frac{\partial\,\mathcal{L}}{\partial\dot{q}_i}\right) - \frac{\partial\,\mathcal{L}}{\partial q_i} = 0\,. \tag{2.4}$$

A very important quantity in this formalism is the canonical momentum defined as:

$$P_{q_i} = \frac{\partial\,\mathcal{L}}{\partial\dot{q}_i} = p_{q_i} + qA_{q_i}(\vec{r}, t) \tag{2.5}$$

where p_{q_i} is the ordinary kinetic momentum.

When the Lagrangian does not depend explicitly on a coordinate q_i, the Euler – Lagrange equation 2.4 becomes

$$\frac{\mathrm{d}}{\mathrm{dt}}\left(\frac{\partial\,\mathcal{L}}{\partial\dot{q}_i}\right) = 0$$

and the corresponding canonical momentum is constant. In this case, the action integral defined as:

$$J_{q_i} = \oint P_{q_i} \mathrm{d}q_i \tag{2.6}$$

is a constant of motion.

Motion in a homogeneous magnetic field

In a positron beam system, for many sections the magnetic field can be assumed as homogeneous and pointing in the $\vec{z}$ direction, $\vec{B} = (0, 0, B_0)$. With this assumption equation 2.2 can be written as:

$$\begin{cases} m\ddot{x} &= qB_0\dot{y} \\ m\ddot{y} &= -qB_0\dot{x} \\ m\ddot{z} &= 0 \end{cases} \tag{2.7}$$

Solving this set of equations the velocity of the particle is obtained:

$$\vec{v}(t) = v_\perp(\hat{y} - i\hat{x})e^{i\omega t} + v_\parallel \hat{z} \tag{2.8}$$

which, integrated once, gives the position $\vec{r}(t)$ as a function of the time:

$$\vec{r}(t) = -i\frac{v_\perp}{\omega}(\hat{y} - i\hat{x})e^{i\omega t} + v_\parallel t\hat{z}\,. \tag{2.9}$$

Equation 2.9 describes a circular motion in the plane perpendicular to the magnetic field $\vec{B}$ with angular velocity $\omega = \frac{qB_0}{m}$ and a constant motion in the $\vec{z}$ direction. The gyration radius and length can be calculated:

$$r_g = \frac{v_\perp}{\omega} = \frac{p_\perp}{qB_0} = \frac{\sqrt{2m}}{q} \cdot \frac{\sqrt{E_\perp}}{B_0} \tag{2.10}$$

$$l_g = 2\pi\frac{v_\parallel}{\omega} = 2\pi\frac{p_\parallel}{qB_0} = 2\pi\frac{\sqrt{2m}}{q} \cdot \frac{\sqrt{E_\parallel}}{B_0}\,. \tag{2.11}$$

Here $v_\perp$, $p_\perp$, and $E_\perp$ and $v_\parallel$, $p_\parallel$, and $E_\parallel$ are the components of $\vec{v}$, $\vec{p}$ and E perpendicular and parallel to the direction of motion, respectively.

Using the Lagrangian formalism previously described and with cylindrical coordinates (r, θ, z), it can be easily shown that the canonical momentum associated with θ and z are conserved. The Lagrangian in the case of a

homogeneous magnetic field in the $\vec{z}$ direction (with the vector potential $\vec{A} = \frac{1}{2}\vec{B} \times \vec{r} = (0, \frac{rB_0}{2}, 0)$) is:

$$\begin{aligned} \mathcal{L} &= m_0 c^2 \left(1 - \sqrt{1 - \tfrac{\dot{r}^2 + r^2\dot{\theta}^2 + \dot{z}^2}{c^2}}\right) + qr\dot{\theta}A_\theta = \\ &= m_0 c^2 \left(1 - \sqrt{1 - \tfrac{\dot{r}^2 + r^2\dot{\theta}^2 + \dot{z}^2}{c^2}}\right) + qr\dot{\theta}\tfrac{B_0}{2} \end{aligned} \tag{2.12}$$

Since this Lagrangian does not depend explicitly from the coordinates θ and z, the corresponding canonical momenta P_θ and P_z are constant:

$$P_\theta = mr^2\dot{\theta} + qrA_0 = mr^2\dot{\theta} + qr^2\frac{B_0}{2} \tag{2.13}$$

$$P_z = m\dot{z} \tag{2.14}$$

These two equations describe the conservation of the axial components of the angular momentum and of the ordinary kinetic momentum, respectively. The Euler – Lagrange equation (equation 2.4) for the radial component can be written as:

$$\frac{\mathrm{d}}{\mathrm{dt}}(m\dot{r}) - mr\dot{\theta}^2 = qr\dot{\theta}B_0 \tag{2.15}$$

The stationary solution of equations 2.13 and 2.15 is found for constant r and $\dot{\theta} = -\frac{qB_0}{m}$. Combining this solution with equation 2.13, it can be shown that the canonical momentum of θ is proportional to r^2B_0:

$$P_\theta \propto r^2 B_0 = \text{constant} \tag{2.16}$$

and the corresponding action integral (integrating over one gyration period):

$$J_\theta = -\frac{qB_0r^2}{2}\int_0^{2\pi} \mathrm{d}\theta = -q\pi r^2 B_0 \tag{2.17}$$

Equation 2.17 shows that the number of field lines crossing one orbit remains constant. This is also valid for small variations of the magnetic field B. As a consequence, if the positrons are moving from a region with magnetic field B_1 with a gyration radius r_1 to a region were a magnetic field B_2 is present, the gyration radius r_2 becomes:

$$r_2 = r_1\sqrt{\frac{B_1}{B_2}}\,. \tag{2.18}$$

Thus, if the magnetic field is adiabatically increased ($B_2 > B_1$), the gyration radius decreases.

2.2.2 Pulsed beams

To perform depth - resolved Positron Annihilation Lifetime Spectroscopy measurements with positron beams, the exact time of implantation of the positrons is required. To achieve a time resolution good enough for materials science investigations ($\sim 100\,\mathrm{ps}$), a time structure is applied to a continuous beam. There are essentially two techniques, described in the next sections: *bunching* and *chopping*.

Bunching

The theory of bunching was developed in the 60's by Whiteway [32] for ion beams. This technique consists in modulating the longitudinal velocity of the particles by applying a time dependent electric field to accelerate (decelerate) the particles that would arrive too late (too early) at the time focus. The main advantage of the bunching method is that a compression in the time space is done and therefore in the ideal case no intensity loss is observed. The working principle of a buncher is illustrated schematically in the upper part of figure 2.1. In the lower part the phase space is shown. In particular, the left plot shows the phase space at the entrance of the buncher, *i. e.* a continuous beam with average energy E_0 and an energy spread ΔE. After the energy modulation at the buncher gap the phase space changes and at the target, the beam has a time structure of width Δt at expense of its monochromaticity ($\Delta E_{buncher} < \Delta E_{target}$).

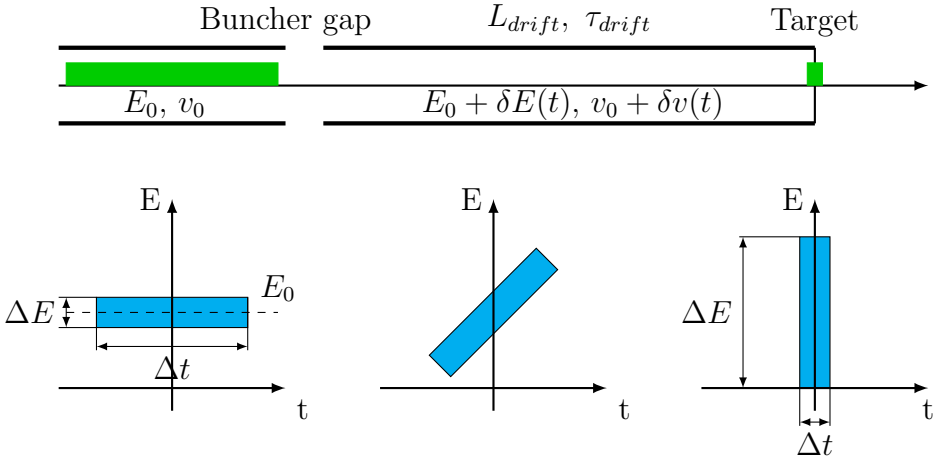

Figure 2.1: Upper part: geometry of the buncher with the relevant quantities and dimensions used in the text. Lower part: time compression of the bunched pulse.

Considering a non relativistic beam with no space charge effects, which is

valid for a low energy positron beam of $E < 30\,\mathrm{keV}$, the ideal modulation energy $\delta E(t)$ can be described by the equation:

$$\delta E(t) = E_0 \left[\left(1 - \frac{t}{\tau} \right)^{-2} - 1 \right] \tag{2.19}$$

where E_0 and t are the energy and the time at which positrons enter the buncher, respectively, and τ is the transit time from the buncher to the time focus position [33].

In positron beam experiments, the required time window is typically in the $\sim 10\,\mathrm{ns}$ range, corresponding to repetition rates in the range of tens of MHz.

In particular, the pulsing system of PLEPS is operated with a frequency of 50 MHz, corresponding to a time window of 20 ns.

Sawtooth buncher. Due to the technical difficulties in generating a parabolic electric signal with such repetition rate, equation 2.19 is approximated by taking into account that $t \ll \tau$ and therefore the modulating potential can be written as:

$$\delta U(t) \approx \frac{2E_0}{e} \frac{t}{\tau} \,. \tag{2.20}$$

Equation 2.20 shows that the optimal modulating signal has the form of a sawtooth wave. Such a signal can be easily produced, but only with a maximum amplitude of the order of tens of volts [34].

A sawtooth signal is used for the prebuncher of PLEPS, which is described in section 3.2.2, since in this case an energy modulation $< 10\,\mathrm{V}$ is required in order not to broaden too much the energy distribution of the beam which is fed into the chopper.

Sine − wave buncher. To achieve a time resolution in the range of $\sim 100\,\mathrm{ps}$ a high amplitude is needed. Usually a sine − wave buncher with a resonator is used. The modulating potential of equation 2.20 is further approximated using only the linear part of the sinus function at the zero-crossing.

As can be seen in figure 2.2 only about 10% of the total time window fulfills the linearity condition and in this case equation 2.20 can be written as:

$$\delta U(t) = U_0 \sin(\omega t) \approx U_0 \omega t = \frac{2E_0}{e} \frac{t}{\tau} \,. \tag{2.21}$$

From this equation the required amplitude can be obtained:

$$U_0 = \frac{2E_0}{e\omega\tau} = \frac{1}{e\omega L} \sqrt{\frac{8E_0^3}{m}} \,. \tag{2.22}$$

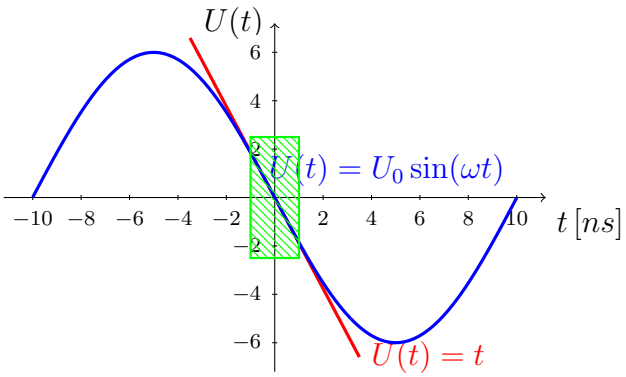

Figure 2.2: Comparison of sine and sawtooth wave.

In the case of PLEPS a double – gap sine – wave buncher is used for the final pulse compression. This means that the modulating potential is applied to the central electrode of the buncher and an energy modulation is accomplished at both gaps. In particular, a double modulation is achieved if the length and the potential of the central electrode are chosen such, that the time of flight from the first to the second gap is equal to half a period of the high frequency signal. In this case, as can be seen in figure 2.3, a positron that would arrive late (early) at the target, experiences a negative (positive) potential difference at both gaps and therefore is accelerated (decelerated) twice. The velocity of the reference particle can be written as:

$$v = \frac{l}{\tau} = \frac{2l}{T} = \sqrt{\frac{2eU}{m}} \tag{2.23}$$

where τ is the transit time between the two gaps with distance l and T is the period of the high frequency sine signal. From equation 2.23 the electric potential of the central electrode U can be easily determined:

$$U = \frac{m}{2e}\left(\frac{2l}{T}\right)^2 . \tag{2.24}$$

Chopping

Beam chopping is a completely different approach in which the continuous beam is periodically blanked out, giving pulses with no background in between. The suppression is achieved by applying a perpendicular time dependent field to deflect the beam so that only a part of it can pass through a slit positioned at the exit of the chopper.

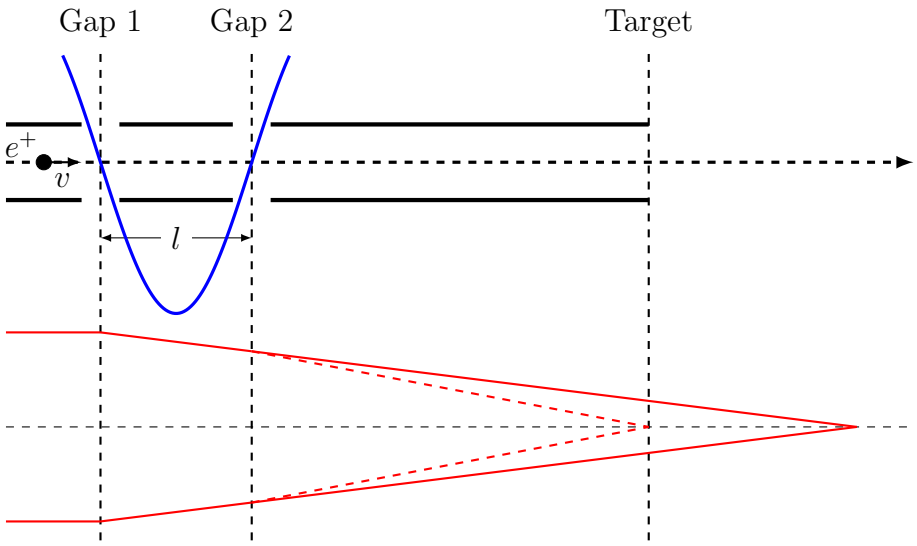

Figure 2.3: Working principles of a sine wave double gap buncher. The continuous red line shows the effect of the first gap, which gives a time focus in a position far behind the target. At the second gap the pulse undergoes a further energy modulation, resulting in a shortening of the focal length, *e. g.* a time focus at the location of the target is achieved.

Deflection chopper with no *B* field. The working principle of a chopper when no magnetic field is present is shown schematically in figure 2.4(a).

Basically, the positron that experience an electric field when passing through the two plates (D1 and D2) are deflected and annihilate on the slit S. A constant electric potential V_{D1} is applied to the plate D1. The time dependent electric field is produced by applying a high frequency electric signal on the plate D2 superimposed on a constant potential V_{D2} lower than V_{D1}. When the sum of the amplitude of the high frequency signal and the potential of the plate is equal to the dc level of the second plate, no electric field is experienced by the positrons. These positrons are thus not deflected and can pass through the slit S.

Due to the width of the slit, also positrons that are slightly affected by the electric field (blue case in figure 2.4(a)) are not suppressed and a finite acceptance window is defined. By adjusting the amplitude of the high frequency signal, the potential of the plate and the width of the slit the acceptance window ΔT of the chopper can be optimized. This is schematically illustrated in figure 2.5. In particular, from this picture it is clear that by choosing a higher amplitude of the sine wave (light blue case), the width of the pulse can be reduced ($\Delta T < \Delta T'$).

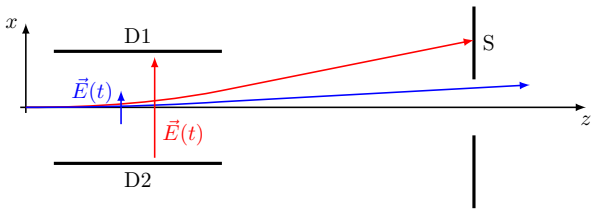

(a) No magnetic field. The plane parallel to the direction of motion (xz - plane) is illustrated.

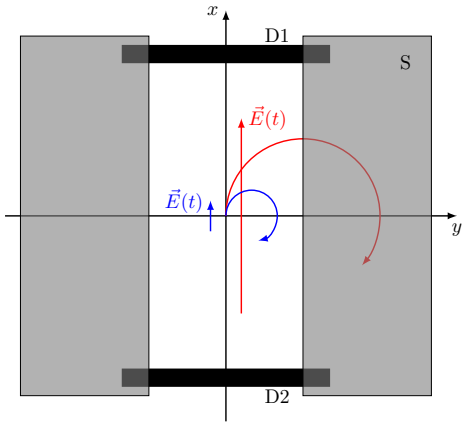

(b) With longitudinal magnetic field. The plane perpendicular to the direction of motion (xy - plane) is shown.

Figure 2.4: Working principle of the chopper with and without magnetic field, upper and lower picture, respectively. The positrons move in the z direction passing first through the deflecting plates D1 and D2 and then through the slit S. Two trajectories, *i. e.* when a small and a big electric field is experienced by the positrons, are shown in blue and red, respectively.

Deflection chopper in presence of a longitudinal B field. When a longitudinal magnetic field is present, the trajectories of the positrons passing through the chopper are drastically different from the previous case. Due to the electric field experienced during the transit through the plates, the positrons gain a velocity perpendicular to the direction of motion. Differently from figure 2.4(b), the presence of the magnetic field causes a gyration motion in the xy - plane. The radius of the orbit described by the positrons can be

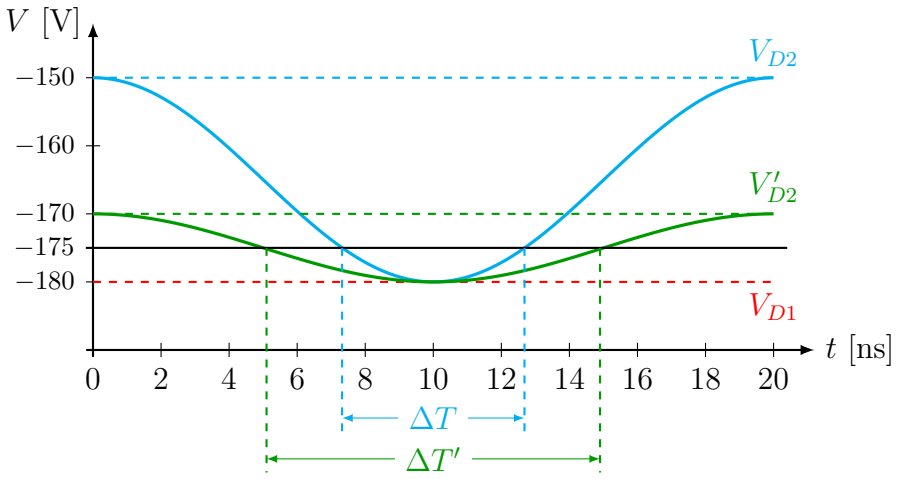

Figure 2.5: Acceptance window of the chopper.

approximated by (from equation 2.10):

$$r_g = \frac{mv_\perp}{qB} \approx \frac{l}{v_\parallel} \cdot \frac{E}{B} = l\sqrt{\frac{m}{2E_\parallel}} \cdot \frac{E}{B}\,. \tag{2.25}$$

Here l is the length of the deflection plates, $v_\perp$ and $v_\parallel$ are the transversal and longitudinal component of the velocity, respectively, and $E_\parallel$ is the component of the energy parallel to the direction of motion. E and B are the electric and magnetic fields experienced by the positrons during the transit through the deflection plates.

This equation shows that the width of the resulting pulse depends not only on the width of the slit, on the amplitude of the sine wave and on the potential applied to the deflection plate, but also on magnetic field B.

Since the positrons are magnetically guided from the source to the target of PLEPS, in this case a chopper as described in this section is required. A detailed description of the chopper of PLEPS can be found in [3].

2.3 Positrons in matter

In the next paragraphs we summarize the "fate" of the positrons after the implantation into a solid, *i. e.* the slowing down and diffusion processes. A comprehensive description can be found in [13, 14].

When positrons are implanted into a sample, they lose their kinetic energy through different processes depending on their energy and on the type of material, and they reach the thermal equilibrium in a time short compared to the positron lifetime [35].

In metals, at high energies the dominant process is the ionization of the atoms of the crystal and the energy transfer is high meaning that the time spent in this energy range is very short. When the energy decreases below about 100 eV excitation of free electrons start to dominate and also plasmon excitation and electron–hole pairs creation are possible. When the positrons approach thermal energy, they undergo mainly phonon scattering and they are completely thermalized in a time which is much shorter than the typical positron lifetime. Nieminen and Oliva [36] have estimated that positron implanted with an energy of 1 keV in Al are completely thermalized in 6.8 ps and 64 ps at 300 K and 15 K, respectively. This fact has been confirmed by Kubica and Stewart [37] by means of Angular Correlation of the Annihilation Radiation measurements performed on various materials in a temperature range down to liquid helium. Their experiments have shown that before annihilation positrons are very close to thermal energy even at the lowest temperature.

In semiconductors and insulators, the electron–hole excitation process is inhibited, when the kinetic energy of the positrons is smaller than the band gap. However, in the case of semiconductors the phonon emission process is already very efficient at energies of about 1 eV which results in thermalization times equivalent to those in metals [22].

Differently from metals and semiconductors, in insulators phonon scattering is not effective enough to complete the thermalization process in such a short time, especially at low implantation energies, a fraction of the implanted positrons can reach the surface and be re-emitted into the vacuum with an energy greater than the thermal energy. These positrons are called *epithermal* and they have been observed not only in insulators, but also in metals and semiconductors as described by Knight and Coleman in copper [38] and silver [39] at very low positron implantation energies.

After the thermalization process, the positrons start diffusing into the solid and, due to their positive charge, they sense missing ions in the lattice as a potential well. Considering the De Broglie wavelength of thermalized positrons of 62 Å, they may be trapped very efficiently into defects. Eventually, the positrons will annihilate with an electron of the material either from the delocalized bulk state or from a localized state at a trapping site.

2.3.1 Diffusion

The diffusion of a positron in the crystal can be described in the one dimensional case and for low energy positron beam experiments by the following

equation [40]:

$$\frac{\mathrm{d}n(z,t)}{\mathrm{dt}} = D_+\nabla^2 n(z,t) - \left[\lambda_B + \sum_i \kappa_i(z)\right] n(z,t) - \nabla\cdot[\vec{v}(z)n(z,t)] \quad (2.26)$$

where $n(z,t)$ is the positron density at time t at a distance z below the surface, D_+ is the positron diffusion constant, λ_B the annihilation rate in the bulk state and $\vec{v}$ the drift velocity due to an external electric field. κ_i is the trapping rate into the i-th defect and can be written as the product of the concentration c of the i-th defect and its specific trapping rate μ_i. Equation 2.26 can be solved using the boundary condition at the surface

$$D_+\nabla n(z,t)|_{z=0} = \nu n(0,t)\,, \quad (2.27)$$

where ν is the trapping rate at the surface, and with the initial condition

$$n(z,0) = P(z,E) \quad (2.28)$$

being $P(z,E)$ the positron implantation profile for positron implantation energy E.

If the diffusion constant D_+ is known, the diffusion length L_+ can be calculated by:

$$L_+ = \sqrt{D_+\tau_B}\,, \quad (2.29)$$

but, in the presence of defects the bulk lifetime in equation 2.29 is substituted with the "reduced bulk lifetime" τ_R:

$$L_+^{defects} = \sqrt{D_+\tau_R} = \sqrt{\frac{D_+}{\lambda_B + \sum_i \kappa_i(z)}}\,. \quad (2.30)$$

The diffusion length of positrons in defect free materials is on the order of 100 nm (as an example: (141 ± 4) nm in well-annealed Al [41]), but can be as short as 10 nm in amorphous materials or in presence of defects (13 nm in isothermally fatigued aluminum [41]).

For monoenergetic positron beams the implantation profile can be described by a Makhovian function [13]:

$$P(z,E) = -\frac{d}{dz}\left[e^{-(z/z_0)^m}\right] = \frac{mz^{m-1}}{z_0^m}e^{-(z/z_0)^m} \quad (2.31)$$

where

$$z_0 = \frac{\overline{z}}{\Gamma\left[\frac{1}{m}+1\right]} \quad , \qquad \Gamma[x] = \int_0^\infty t^{x-1}e^{-t}dt$$

From Monte Carlo simulations and various experiments, Valkealathi and Nieminen [42] have estimated the value of the parameter m and they have found a nearly constant value of ≈ 1.9 for different metals.

However, the approximation with $m = 2$ is often used, therefore the Gamma function assumes the constant value of $\Gamma[3/2] = \sqrt{\pi/2}$ and the implantation profile reduces to the derivative of a Gaussian (see Eq. 2.32).

$$P(z, E) = \frac{\pi z}{2\overline{z}^2} e^{-\frac{\pi}{2}(z/\overline{z})^2} . \tag{2.32}$$

Doppler Broadening Spectroscopy measurements on multi-layered ZnS – Al_2O_3 structures by Vehanen *et al.* [43] have shown that the mean implantation depth $\overline{z}$ can be well described by

$$\overline{z} \approx \frac{40}{\rho} E^{1.6} . \tag{2.33}$$

Here, $\overline{z}$ is in nm, if ρ and E are expressed in g/cm^3 and keV, respectively. In the case of amorphous polymers a better fit for the mean implantation depth was obtained by Algers *et al.* [44] with the parameters:

$$\overline{z} \approx \frac{28.1}{\rho} E^{1.71} . \tag{2.34}$$

In figure 2.6 (left) the positron implantation profiles from equation 2.32 for a silicon target $\left(\rho = 2.32\,\mathrm{g/cm^3}\right)$ at different positron implantation energies are shown. On the right hand side of the figure the mean implantation depth is plotted as a function of the positron implantation energy for Si and for $\rho = 1.0\,\mathrm{g/cm^3}$ (typical density of polymer samples) calculated with equations 2.33 and 2.34, respectively.

2.4 Positronium

Positronium is the bound state of a positron and an electron. The existence of this quasi stable atom was suggested by Mohorovicic [19] and after some years was proved by Deutsch [20] by measuring the lifetime of the positron in various gases. Later on, also its formation in small grained powders [45] and on the surface of metals [46] was proved and nowadays, it is widely used for the determination of the size of the free volumes in polymers.

It can be formed in two possible states depending on the total spin of the system:

s=0 singlet state called para–positronium (p–Ps) with a lifetime in vacuum of 125 ps and annihilation via $2n$ gamma quanta (2γ decay rate is $\approx 10^6$ times bigger than for the 4γ process)

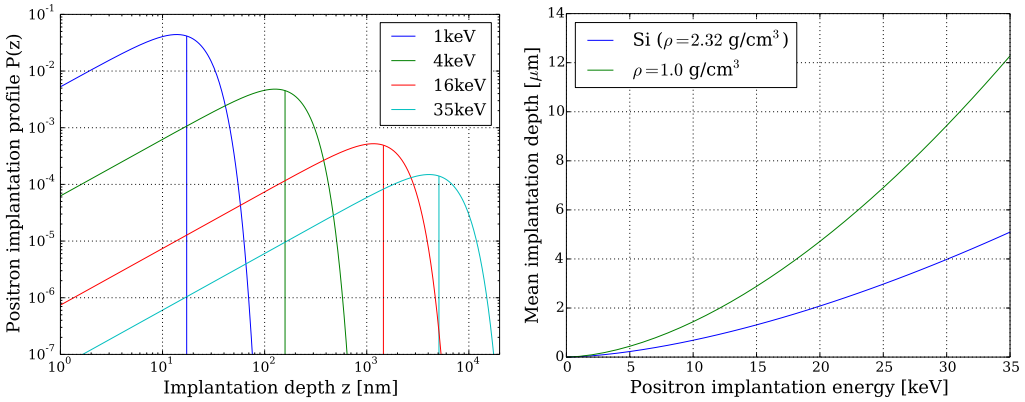

Figure 2.6: Left: positron implantation profiles of silicon ($\rho = 2.32\,\mathrm{g/cm^3}$) at different positron implantation energies. The vertical lines mark the mean implantation depth at the corresponding implantation energy. Right: mean implantation depth $\overline{z}$ as a function of the implantation energy from equations 2.33 and 2.34 for Si and for $\rho = 1.0\,\mathrm{g/cm^3}$ (typical density of polymer samples), respectively.

s=1 triplet state called orthopositronium (o–Ps), that lives much longer (142 ns in vacuum) and decays via an odd number of gammas (3γ process is $\approx 10^6$ times more probable than the 5γ decay)

The formation probability in vacuum is given by the spin statistics, namely o–Ps and p–Ps can be formed with a 3 to 1 ratio.

When positronium is formed in a solid, the quenching of orthopositronium due to the annihilation of the positron with an electron of the solid instead of the one it is bounded to can occur. The result of this phenomenon, called pickoff, is a shortening of the orthopositronium lifetime. Tao [47] and Eldrup *et al.* [48] developed a simple quantum mechanical model that relates the o–Ps pickoff lifetime to the average void radius. This model assumes the void as a spherical, infinite potential well with radius R and that the positronium wave function can overlap with a layer of electrons of the material of thickness ΔR, as shown in figure 2.7.

By solving the Schrödinger equation with these boundary conditions, the annihilation probability can be written as:

$$\lambda_{pickoff} = \tau_{pickoff}^{-1} = \lambda_b \cdot \left[1 - \frac{R}{R+\Delta R} + \frac{1}{2\pi} \cdot \sin\left(\frac{2\pi R}{R+\Delta R}\right)\right] \tag{2.35}$$

where λ_b is the spin averaged annihilation rate of positronium:

$$\lambda_b = \frac{1}{4}\lambda_{pPs} + \frac{3}{4}\lambda_{oPs} \approx \frac{1}{4}\lambda_{pPs} \approx 2ns^{-1} \tag{2.36}$$

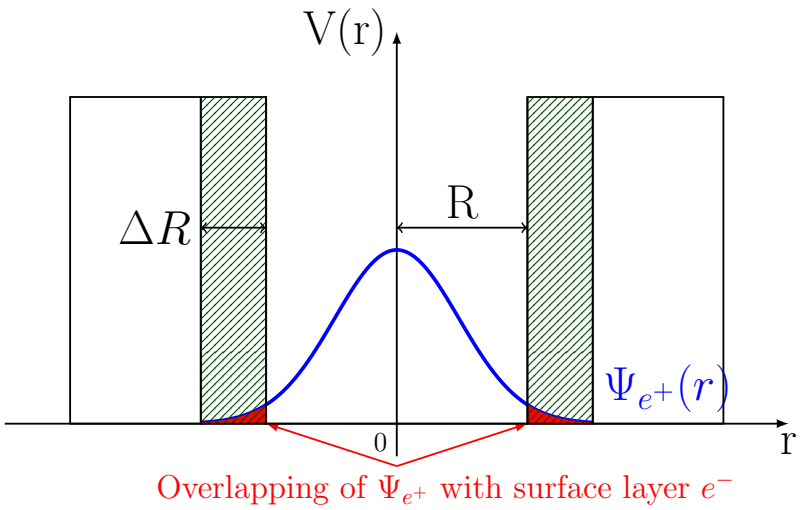

Figure 2.7: Tao-Eldrup model: the blue line represents the Ps wavefunction in the infinite potential well of radius R. The overlap with the electron layer of thickness ΔR is also shown.

This relation has been tested in various plastic crystals and agrees very well with the experimental measurements by using a value of 0.17 nm for the empirical parameter ΔR [48]. The parameter ΔR depends on the geometry of the pores and on the investigated material as reported by Goworek [49], Gidley *et al.* [50]. This model is limited to spherical voids with diameter smaller than ≈ 2.5 nm. Therefore, different theoretical models have been proposed to extend it to larger and differently shaped pores [51, 50] and also to take into account the influence of the temperature [50].

2.5 Positron techniques

In this section I will describe the two positron annihilation techniques relevant for this work, *e. g.* Doppler Broadening Spectroscopy (DBS) and Positron Annihilation Lifetime Spectroscopy (PALS).

2.5.1 Doppler Broadening Spectroscopy

In figure 2.8 the influence of the electron momentum on the annihilation radiation is illustrated. In particular, if the electron - positron pair has a total momentum $\vec{p}$, a Doppler shift of the two emitted gamma quanta is

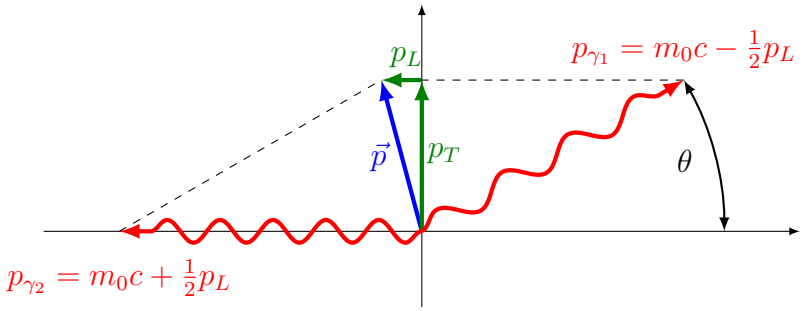

Figure 2.8: Illustration of the conservation of the momentum in the laboratory system. The total momentum of the positron - electron pair leads to a Doppler shift and to a deviation from the collinearity of the annihilation radiation.

observed in the laboratory system. The corresponding momenta are:

$$p_{\gamma 1,2} = m_0c \pm \frac{1}{2}pL \tag{2.37}$$

and the energy of the two emitted gamma quanta can be written as:

$$E = m_0c^2 \pm cp_L/2\,. \tag{2.38}$$

The annihilation gamma quanta are detected with high purity Ge detector with resolution of about 1 keV at 511 keV.

Usually the DBS measurements are characterized by the shape (S) and the wing (W) parameters that are graphically shown in figure 2.9. The S parameter is the number of counts in the central area (A) divided by the total counts in the peak (C). It is related to the low momentum electrons, i. e. the valence electrons, and therefore is associated to the presence of defects. The W parameter is the ratio between the two energy window defined by the area B in figure 2.9 and the total counts in the peak (area C). In this energy range the annihilations with core electrons, which are a fingerprint of the different elements, are taken into account and hence can give information on the chemical environment at the annihilation site.

Normally, a setup for DBS measurements consists of a monoenergetic, continuous positron beam allowing to measure the S and W parameters as a function of the positron implantation energy and, thus, to depth-profile the investigated samples. Since positrons can annihilate from either the bulk (S_B, W_B) or from some trapped states (S_i, W_i), the measured $S = S(E)$ and $W = W(E)$ parameters for each implantation energy are the superpositions of the characteristic values in the different states:

$$\begin{aligned} S(E) &= f_B S_B + \textstyle\sum_i f_i S_i \\ W(E) &= f_B W_B + \textstyle\sum_i f_i W_i \end{aligned} \tag{2.39}$$

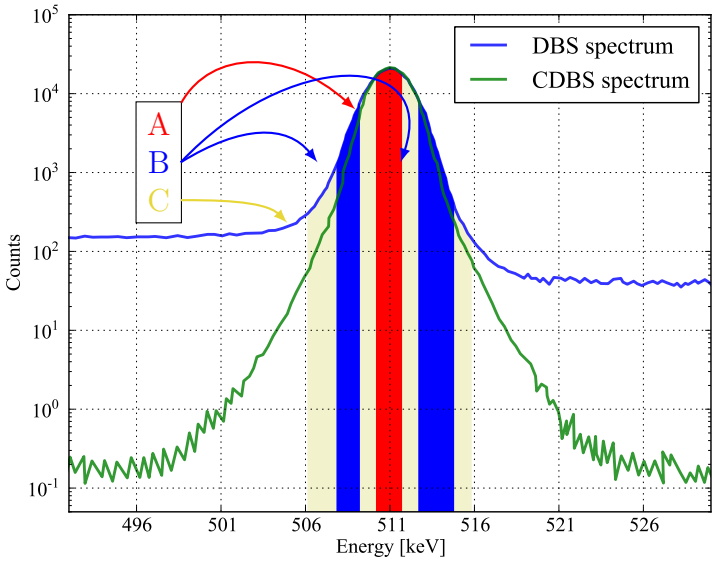

Figure 2.9: Typical 511 keV annihilation line measured in the normal mode (blue line) and in coincidence with two Ge detectors (green line) (adapted from [52]). The regions of interest for the S and W parameter are highlighted in red and blue, respectively.

with the condition that $f_B + \sum_i f_i = 1$. Here f_B and f_i are the fractions of positron annihilating in the bulk and in the i-th trapping site, respectively. In the case of DBS measurements the diffusion equation 2.26 can be treated in the steady state regime:

$$D_+ \nabla^2 n(z,t) - \left[\lambda_B + \sum_i \kappa_i(z) \right] n(z,t) - \nabla \cdot [\vec{v}(z) n(z,t)] = 0 \qquad (2.40)$$

and can be used to fit the measured $S(E)$ and $W(E)$ parameters using programs like VEPFIT [53].

Often the Doppler broadening of the annihilation radiation is measured with two Ge detectors in coincidence. This results in a dramatic reduction of the background (about 1000 times lower in the green spectrum of figure 2.9) and in an improvement of the energy resolution by a factor $\sqrt{2}$. As a consequence it is possible to get information to higher electron momenta ($\Delta E \approx (10-20)$ keV), *i. e.* the electron momentum of the core electrons, and thus to enhance the elemental selectivity of this technique [52].

2.5.2 Positron Annihilation Lifetime Spectroscopy

Positron Annihilation Lifetime Spectroscopy (PALS) measures the time spent by the positron in the material from the implantation to the annihilation with an electron. The positron lifetime depends on the overlap between the positron and the electron wave functions at the location of the annihilation and can be calculated with the following formula:

$$\tau^{-1} = \lambda = \pi r_0^2 c \int d\mathbf{r}\ \rho_+(\mathbf{r})\rho_-(\mathbf{r})\gamma(\rho_+, \rho_-)\,, \tag{2.41}$$

where r_0 is the classical radius of the electron, c is the speed of light, $\gamma(\rho_+, \rho_-)$ is the enhancement factor and ρ_+ and ρ_- are the positron and electron densities, respectively. Knowing the local electron density, it is possible to calculate the positron bulk lifetime using equation 2.41 in any material. The enhancement factor, which takes into account the distortion on the electron wave function induced by the presence of the positron in the crystal, is approximated within the Local Density Approximation (LDA) or the Generalized Gradient Approximation (GGA) schemes [54]. In table 2.4 a comparison between the experimental measurements and the calculated positron lifetimes with different approximations for the enhancement factor $\gamma(\rho_+, \rho_-)$ for some elements is shown. Moreover, since defects act as a potential well and every defect has a characteristic local electron density, equation 2.41 allows to determine the positron lifetime for different defect configurations.

Material	Calculated [ps]		Experiment [ps]
	LDA	GGA	
Al	168[a]	160[a]	167[c]
Si	218[a]	207[a]	224[d]
Mg	233[a]	226[a]	218(2)[e]
$SrTiO_3$	—	152[b]	145(2)[f]

[a] from [54] [b] from [11] [c] from [41]
[d] from [55] [e] from [56] [f] this work (see 4.1)

Table 2.4: Calculated positron bulk lifetime within the local electron density (LDA) and generalized gradient approximation (GGA) for the enhancement factor and experimental values measured with PLEPS.

As an example, the plot in figure 2.10 shows the calculated positron lifetime in magnesium as a function of the number of vacancies in the cluster from [56].

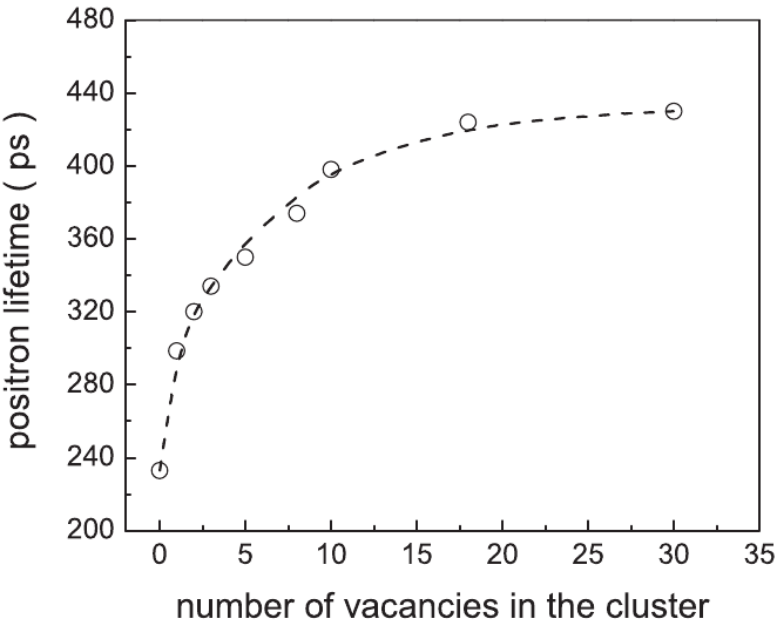

Figure 2.10: Calculated positron lifetime in Mg as a function of the number of vacancies in the cluster (from [56]).

By measuring the time between the implantation of the positron in the target and the detection of the annihilation gamma quantum and accumulating several millions of events, the positron lifetime spectrum can be obtained. It is the combination of all the annihilation channels present in the sample and can be described by a sum of exponential decays convoluted with the instrument function $R(t)$:

$$Z(t) = -\frac{\mathrm{d}n(t)}{\mathrm{dt}} = R(t) \otimes \left[\sum_{j=1}^{N+1} \frac{I_j}{\tau_j} e^{-t/\tau_j} \right] + \text{Background} \tag{2.42}$$

where τ_j and I_j are the lifetime and intensity of the j-th state, respectively.

Moreover, for PALS with a monoenergetic positron beam of variable energy E, the observable $Z = Z(E,t)$ depends also on the implantation energy and not only the inhomogeneity of the defect distribution but also the positron diffusion have to be taken into account. Differently from DBS experiments, one must solve the time dependent diffusion trapping equations [57]:

$$\begin{aligned}\frac{\mathrm{d}n_B(z,t)}{\mathrm{dt}} &= D_+\nabla^2 n_B(z,t) - \left[\lambda_B + \sum_i \kappa_i(z)\right] n(z,t) \\ &\quad -\nabla\cdot[\vec{v}(z)n_B(z,t)] + P_B(z,t) \\ \frac{\mathrm{d}n_i(z,t)}{\mathrm{dt}} &= -\lambda_i n_i + \kappa_i n_B + P_i(z,t)\,.\end{aligned} \tag{2.43}$$

Here $n_B(z,t)$ and $n_i(z,t)$ are the positron densities in the bulk and in the i-th trapping site (with trapping rate $\kappa_i(z)$), respectively. $P_B(z,t)$ and $P_i(z,t)$ are the population of positrons that after the thermalization time t are in the bulk (with annihilation rate λ_B) and in the i-th trapping site (with annihilation rate λ_i), respectively. Kögel [57] demonstrated that an approximate solution of 2.43 with suitable boundary conditions can be successfully applied not only in single-crystalline Si but also in fine-grained aluminum alloys.

Chapter 3

Pulsed Low Energy Positron System (PLEPS)

PLEPS is a pulsed positron beam of variable energy, which allows positron annihilation lifetime spectroscopy measurements as a function of the implantation depth. Its development began in the mid 80's at the Universität der Bundeswehr München with the dissertation of Schödlbauer [1].

In 2007 (described in section 3.2 and in references [58, 59]) PLEPS was coupled to the new high intensity positron source NEPOMUC (NEutron-induced POsitron source MUniCh [21, 24]) at the research reactor FRM-II with some minor changes.

In this chapter the properties of the NEPOMUC source and of the re-moderator stage are briefly described in section 3.1, while PLEPS and its performances at NEPOMUC and a list of some of the investigated materials are presented in sections 3.2 and 3.3, respectively

3.1 The NEPOMUC source

The high intensity, high brilliance positron source NEPOMUC (NEutron-induced POsitron source MUniCh) was installed at FRM-II in 2004. With a primary beam of $(9 \cdot 10^8)\, e^+/s$, NEPOMUC was the most intense positron source worldwide.

In 2011 the source was upgraded and an even higher intensity of the primary beam was achieved ($(1.5 \cdot 10^9)\, e^+/s$ [24]).

The source consists of two stages (see figure 3.1): an outer cadmium shield and a platinum converter/moderator. The outer stage is a neutron to gamma converter made out of ^{113}Cd, which has a very high cross section of 20600 barn for thermal neutrons. The most probable nuclear reaction is

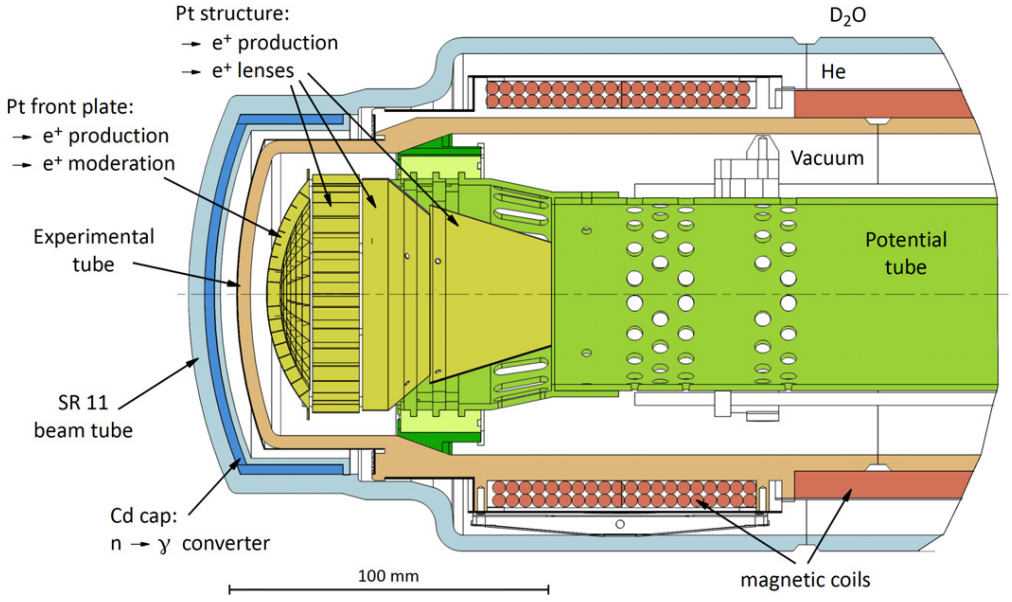

Figure 3.1: Cross section of the NEPOMUC source (from [24]).

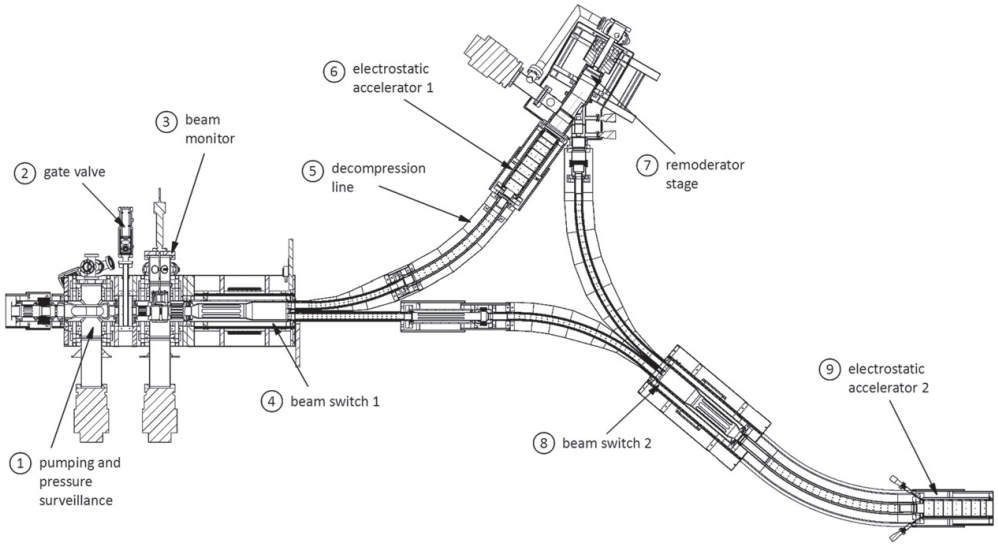

Figure 3.2: View of the new remoderator stage (7) and of the setup for the analysis (3) of the NEPOMUC beam (from [24]).

	Laboratory source	NEPOMUC	
		primary beam	remoderated beam
$I\,[\mathrm{e}^+/\mathrm{s}]$	$2 \cdot 10^5$	$9 \cdot 10^8$	$4.5 \cdot 10^7$
d^{FWHM} [mm]	3	7	< 2
$E_\perp^{FWHM}$ [eV]	0.1	50	1
$B\ \left[\left(\frac{1}{\mathrm{mm}}\right)^2 \frac{\mathrm{e}^+}{\mathrm{eV\,s}}\right]$	$2.2 \cdot 10^5$	$3.7 \cdot 10^5$	$> 1.1 \cdot 10^7$

Table 3.1: Characteristics of a typical laboratory source and the primary and remoderated NEPOMUC beam (data from [61, 24]). The intensity I, diameter d, transversal energy spread $E_\perp$ and brightness B (calculated with equation 3.1) are shown.

$^{113}\mathrm{Cd}(\mathrm{n},\gamma)^{114}\mathrm{Cd}$. The ^{114}Cd nucleus is initially in an highly excited state. The excitation energy is successively released in a γ–cascade and generates positrons via pair-production in the inner platinum structure The emitted positrons have a broad energy distribution with a maximum at an energy of about 800 keV. These positrons are then moderated by a series of platinum foils [60] (see fig. 3.1). A primary beam is formed and extracted by applying a positive high voltage to the Cd/Pt source and is guided to the exit of the concrete shield of the reactor tank in a magnetic field of 5 mT.

The quality of a positron beam can be described by the *brightness* B, defined as [24]:

$$B = \frac{I}{d^2 \Theta^2 E_\parallel} = \frac{I}{d^2 \Delta E_\perp}\,. \tag{3.1}$$

Here, I is the intensity, d the diameter, Θ the angular divergence, $E_\parallel$ the longitudinal energy and $\Delta E_\perp$ the transversal energy spread of the beam. Table 3.1 compares the characteristics of the old laboratory source with the NEPOMUC beam. As can be seen, the NEPOMUC primary beam has a slightly higher brightness with respect to the previous laboratory source. However, this result is mainly due to the extremely high intensity of the beam. With a beam diameter of 7 mm and an energy spread of 50 eV, the NEPOMUC primary beam is not suitable for the operation with PLEPS. For this reason, an additional remoderation stage is needed to further enhance the brightness of the beam.

After the extraction from the concrete shielding of the reactor, the primary beam can be either sent directly to the experiments or to the remoderator stage (see figure 3.2). To remoderate the positrons a tungsten (100)

single crystal is used in reflection geometry. The remoderator setup has an efficiency of 5 % and the extracted positron beam has a diameter of less than 2 mm and a transversal energy spread of ≈ 1 eV [62].

The remoderated beam is then guided with an energy of 20 eV in a solenoidal magnetic field of about 4 mT to the different instruments:

PLEPS (Pulsed Low Energy Positron System): pulsed beam for positron lifetime spectroscopy (Universität der Bundeswehr München)

SPM (Scanning Positron Microscope) : pulsed beam with $\sim 100\,\mu$m spatial resolution for positron lifetime spectroscopy as a function of the beam position on the target (Universität der Bundeswehr München)

CDBS Coincidence Doppler Broadening Spectrometer (TU Munich)

PAES Positron-induced Auger Electron Spectrometer (TU Munich)

Open port for other experiments, *e. g.* positronium Time Of Flight spectrometer (Universitá degli Studi di Trento)

3.2 PLEPS at NEPOMUC

PLEPS is schematically shown in figure 3.3. It can be conceptually divided

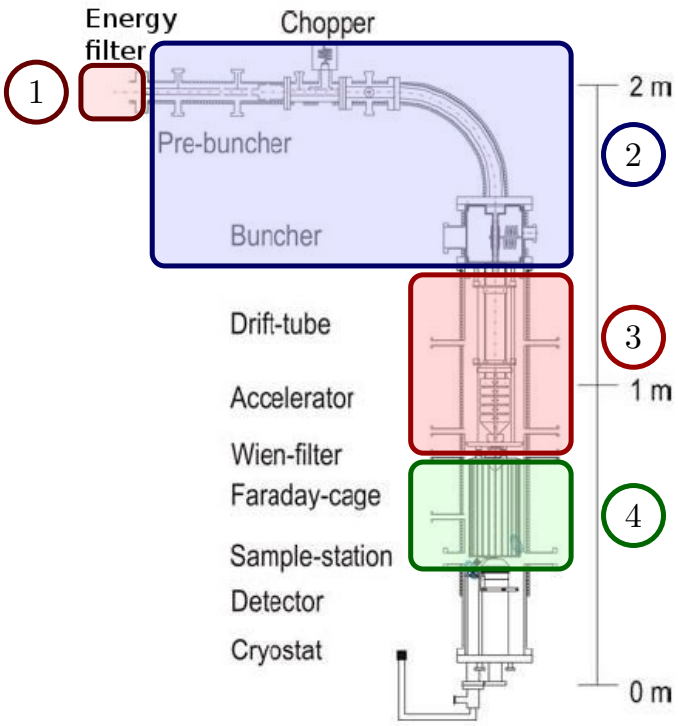

Figure 3.3: Schematic view of the last version of PLEPS in operation at the research reactor FRM-II. The four main parts described in the following sections are highlighted with different colors.

into four main parts: the entrance section, the pulsing system, the acceleration section and the target chamber:

1. The entrance section is a high pass energy filter described in section 3.2.1.
2. The pulsing system consists of the following three elements, described in section 3.2.2:
   - a sawtooth prebuncher which produces a pulse that contains about 50% of the beam intensity in 2 ns
   - a chopper that suppresses the background between two adjacent pulses
   - a double gap buncher that further compresses the pulses down to a FWHM of about 200 ps at the location of the sample

3. In the acceleration section the positron implantation energy can be adjusted from 0.1 keV to 22 keV and is described in section 3.2.3.
4. Finally, the target chamber with a Faraday cage, which is separated from the acceleration section by a vacuum tight plate with a 5 mm hole for the beam. Since sections three and four are evacuated by different pumps this plate acts as a differential pumping stage (see section 3.2.3)

3.2.1 The entrance section

The first stage that the remoderated positrons encounter is a high pass energy filter. It consists of a simple electrode, which cuts off the low energetic positrons by applying a positive potential. The incoming beam was characterized by means of a multi-channel plate detector coupled to a CCD camera at the exit of the energy filter (see figure 3.4). The profile along the green and blue axis are plotted in figure 3.5. The beam has an elliptical shape with a FWHM of about $(1.73 \times 1.38)\,\mathrm{mm}^2$ and a FWTM of about $(3.87 \times 3.09)\,\mathrm{mm}^2$.

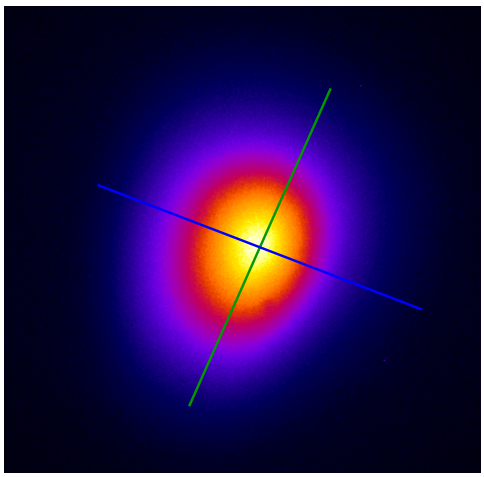

Figure 3.4: Picture of the beam injected into PLEPS registered by a multi-channel plate detector coupled to a CCD camera.

The longitudinal energy distribution can be obtained by applying a positive voltage to the electrode of the energy filter and measuring the count rate at the target location as a function of the applied voltage. Figure 3.6 shows the longitudinal energy distribution with the typical width of less than 1 eV. The measured data points were fitted with a sum of two complementary error functions $\mathrm{erfc}(z) = \frac{2}{\pi}\int_0^z e^{-z^2}\mathrm{d}z$ (black line). The red line gives the normalized energy distribution of the positrons as obtained by the derivative of the fitted transmission curve (FWHM=0.8 eV, FWTM=2.5eV).

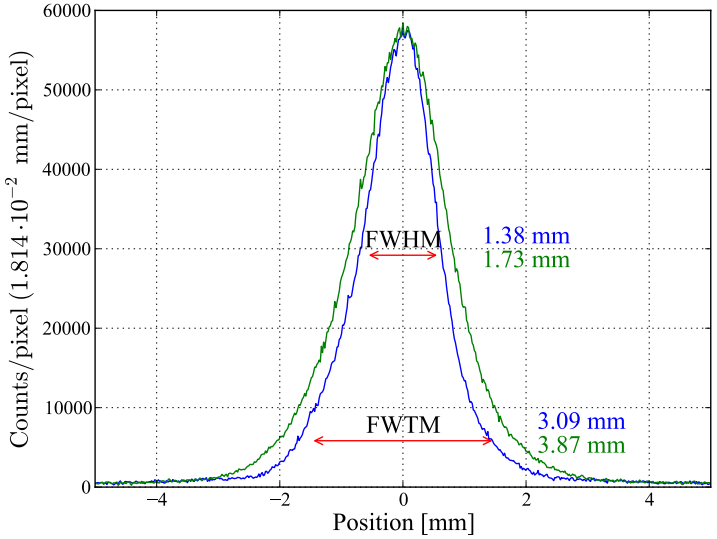

Figure 3.5: Beam profiles along the green and blue axis marked on figure 3.4. The Full Width at Half Maximum (FWHM) and the Full Width at Tenth of Maximum (FWTM) are also shown.

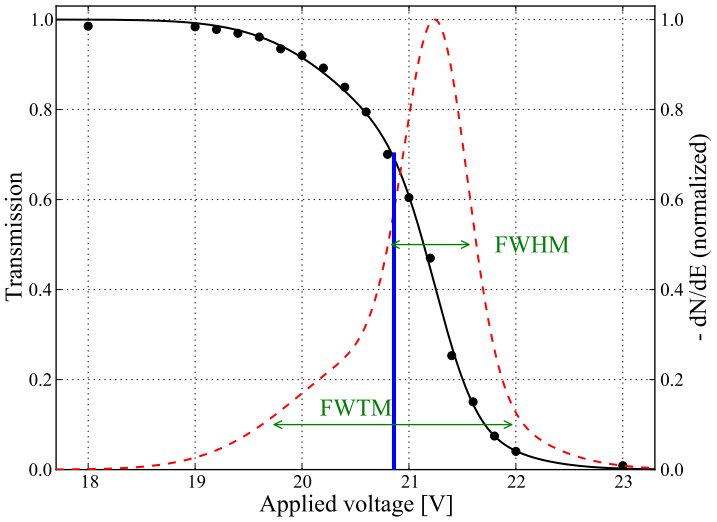

Figure 3.6: Transmission curve as a function of the applied voltage (left) and its normalized derivative (right) of the remoderated positron beam. The cut off of the energy filter is typically set at a transmission of 0.7 (blue line). The FWHM and FWTM are evidenced by the green arrows.

3.2.2 The pulsing system

The pulsing section consists of a prebuncher, a chopper and a buncher. They are operated at a frequency of 50 MHz resulting in a sharp pulse at the target location in a time window of 20 ns.

Prebuncher

To compensate the loss in count rate in the chopper, the positrons pass through the prebuncher, which is operated with a 50 MHz sawtooth electric signal. It compresses roughly 50 % of the positron beam intensity in a pulse with about 2 ns FWHM (see left plot of figure 3.7).

The longitudinal energy distribution of the prebuncher was measured in transmission by applying a positive voltage to the exit electrode of the buncher with the chopper and buncher switched off. The measured transmission curve is illustrated in figure 3.7 (bottom) together with the fitted curve (black solid line, sum of two complementary error functions) and with the corresponding energy distribution (dashed red line).

The energy distribution shows two distinct peaks with similar intensity and comparable width (FWHM $\sim$ 3 eV), but centered at about 18.7 eV and 22.7 eV, respectively. This results in a FWHM of the total energy distribution of 7 eV and a FWTM of 9 eV. The origin of this bimodal distribution is not entirely clear and needs further investigations.

A detailed description of the prebuncher can be found in [34].

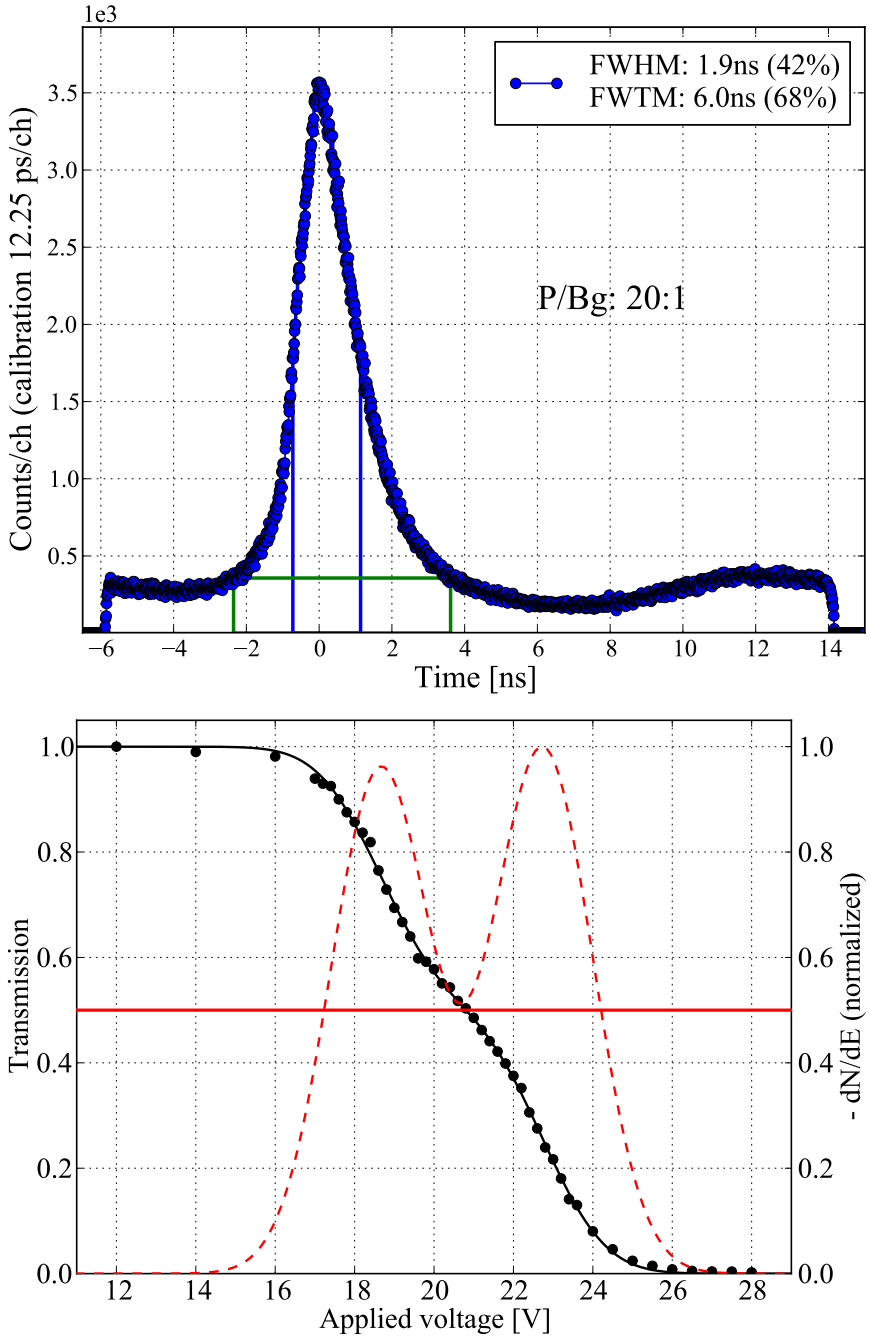

Figure 3.7: Measured spectrum of the prebunched beam at 4 keV positron implantation energy on a p-SiC sample (upper plot). Transmission curve of the prebunched beam measured as a function of the applied voltage (bottom).

Chopper

The prebunched beam successively is accelerated to 200 eV kinetic energy and passes through the chopper in order to suppress the background between two adjacent pulses. It consists basically of two pairs of deflecting plates that are coupled to an external resonator and a slit in between [63]. Due to the electric potential applied to the first plate (sine wave with a frequency of 50 MHz), the positrons start to gyrate with a gyration frequency of 200 MHz, corresponding to a gyration period of 5 ns. The slit is positioned exactly half a gyration length, *i. e.* 21 mm at 200 eV kinetic energy, away from the center of the plates to have the maximal deflection at the location of the chopper slit. Only the positrons that pass through the first plates in a time interval of about 2 ns do not annihilate on the slit. On the second pair of plates the same electric potential with a phase shift of π is applied in order to compensate the effect of the first deflecting plates and to reduce the increase in the energy spread of the beam.

The effect of the chopper on the continuous beam is shown in figure 3.8. In particular, figure 3.8(a) shows a typical spectrum of the chopped beam. The energy distribution measured as described in the previous section is illustrated in plot 3.8(b).

By adding also the prebuncher, the spectrum and the energy distribution shown in figure 3.9 are obtained.

From figure 3.9(a) one can see that the full width at tenth maximum is 2 ns and includes about 95 % of the total counts in the spectrum. Moreover, comparing this spectrum with the one of the prebuncher only (fig. 3.7) shows that the background is strongly suppressed.

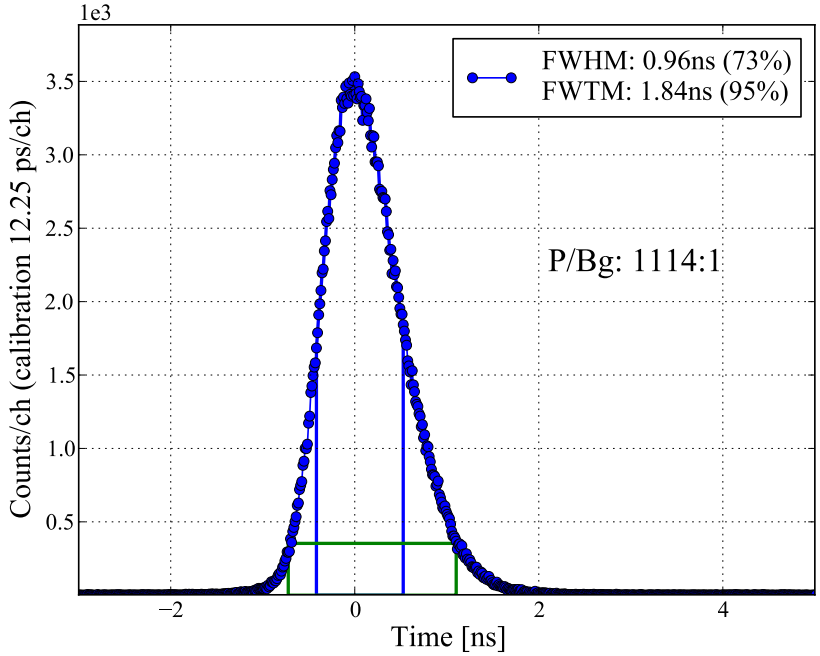

(a) Measured spectrum of the chopped beam.

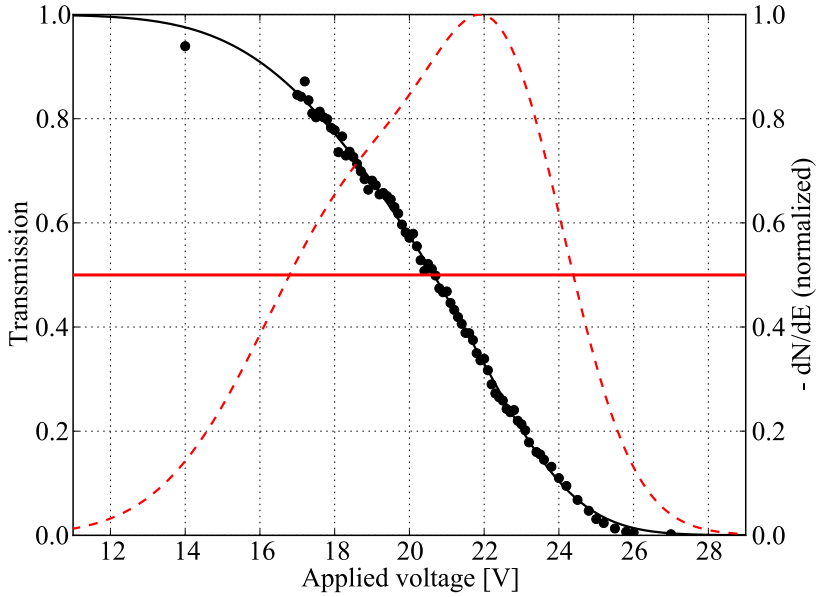

(b) Transmission curve and energy distribution of the chopped beam measured as a function of the applied voltage.

Figure 3.8: Effect of the chopper on the continuous beam at 4 keV positron implantation energy (p-SiC target).

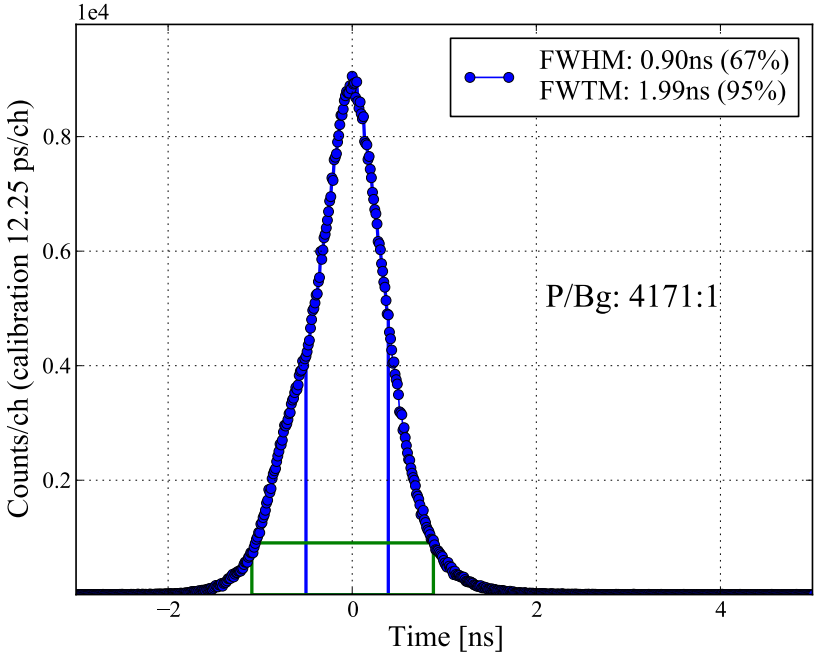

(a) Measured spectrum of the prebunched and chopped beam.

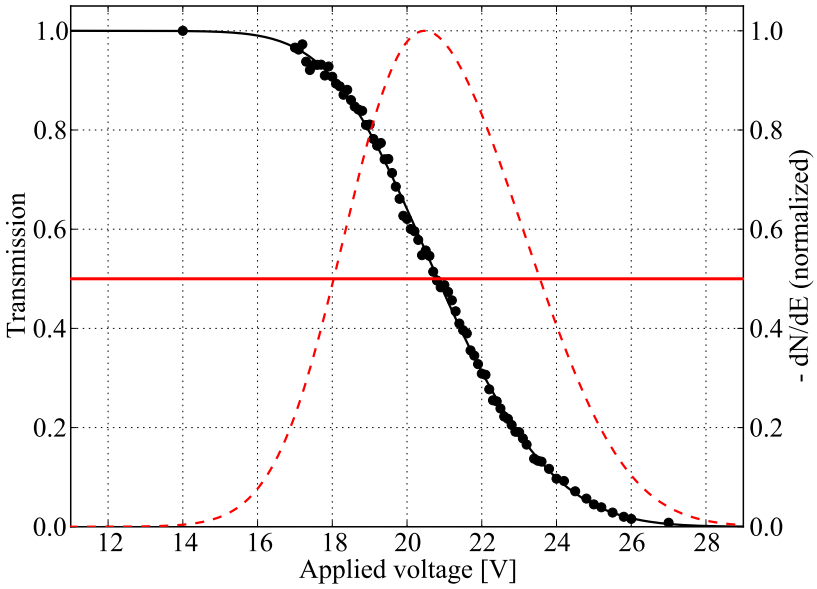

(b) The transmission curve and energy distribution of the prebunched and chopped beam measured as a function of the applied voltage.

Figure 3.9: Effect of the chopper on the prebunched beam at 4 keV positron implantation energy (p-SiC target).

Buncher

The chopped beam is then deflected by 90 degrees and guided to a double gap buncher, which consists of a series of three electrodes. The middle electrode is coupled to a resonator, driven by a sine wave electric potential with a frequency of 50 MHz [63].

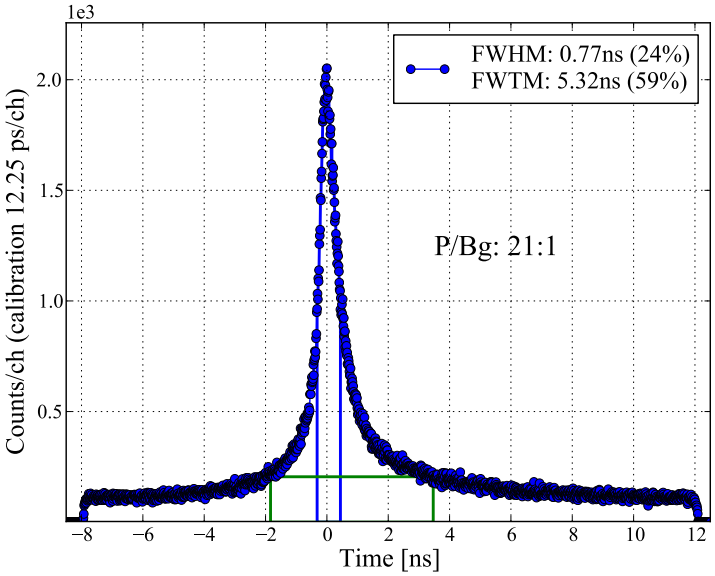

Figure 3.10: Measured spectrum of the buncher on the continuous beam (pre-buncher and chopper switched off) at 4 keV positron implantation energy. The target is a p-type SiC sample.

Figure 3.10 and 3.11 show a measured spectrum of the buncher alone and of the whole pulsing system, respectively. The buncher compresses the pulse further to about (200-300) ps FWHM at each positron implantation energy.

Assuming that the pulsing system and the detector contribute independently to the total time resolution, the full width at half maximum of the total system can be written as

$$FWHM^2_{total} = FWHM^2_{pulsing} + FWHM^2_{detector}\,. \tag{3.2}$$

The total time resolution $FWHM_{total}$ can be found by measuring a sample with known lifetime (in our case a p-type SiC with bulk lifetime of 145 ps) and extracting the resolution function at each implantation energy. A typical value for the total time resolution is about 260 ps obtained with a photomultiplier XP2020/URQ coupled to a BaF_2 scintillator of about 80 cm^3. The resolution of the detector $FWHM_{detector}$ is measured independently with a

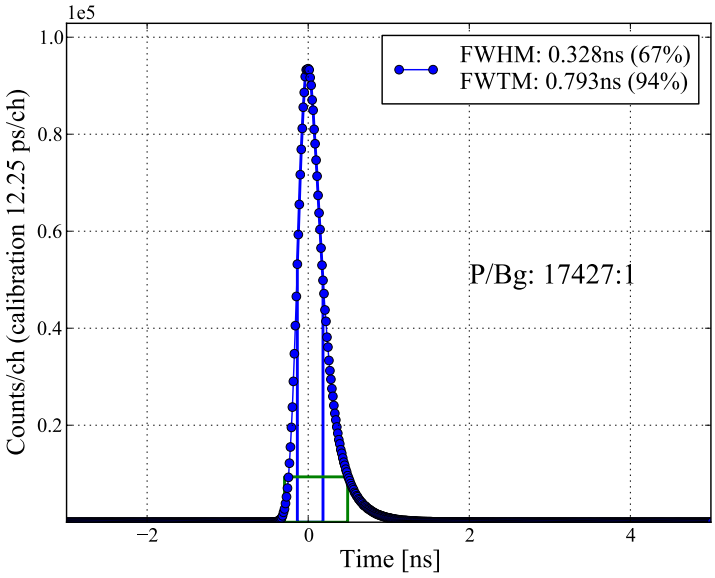

Figure 3.11: Effect of the whole pulsing system (prebuncher, chopper and buncher) on the continuous beam at 4 keV positron implantation energy. The target is a p-type SiC sample.

^{60}Co radioactive source and is found to be ∼180 ps at 511 keV gamma energy. Inserting these values in equation 3.2 a time resolution of the pulsing system of about 190 ps is obtained.

3.2.3 The acceleration section and the target chamber

At the exit of the buncher is the acceleration section, which consists of a drift tube and an accelerator. The drift tube, in combination with the Faraday cage located in the target chamber, is necessary in order to keep the transit time of the pulse from the buncher exit to the target constant for every implantation energy. As a consequence the time resolution would ideally be independent from the implantation energy. Before entering the target chamber, positrons pass through a Wien filter necessary to suppress satellite structures caused by positrons that, after being backscattered, are able to reach the accelerator and eventually to be re-implanted in the target.

Finally, positrons pass through the field free Faraday cage and are implanted into the sample, where they annihilate. A schematic view of the target chamber is shown in 3.12. The annihilation gamma quanta are usually detected with a photomultiplier XP2020/URQ coupled to a BaF_2 scintillator (truncated pyramid of about 80 cm^3 volume) and placed about 2 cm under the sample position. The small distance from the target makes the standard

position unique for its high efficiency. On the other hand not all the gamma quanta coming from annihilations from other parts of the target chamber can be shielded and they cause a structured background in the positron lifetime spectra (see discussion in chapter 6). As shown in figure 3.12, two side ports are also available for DBS simultaneously to PALS, Age Momentum Correlation (AMOC) measurements or PALS in coincidence. The latter option could be interesting for the suppression of the structured background. However, the drawback of the coincidence method is the dramatic loss in count rate due to the distance of the two ports (about 20 cm from the target, giving a count rate 400 times lower than with the detector in the standard position).

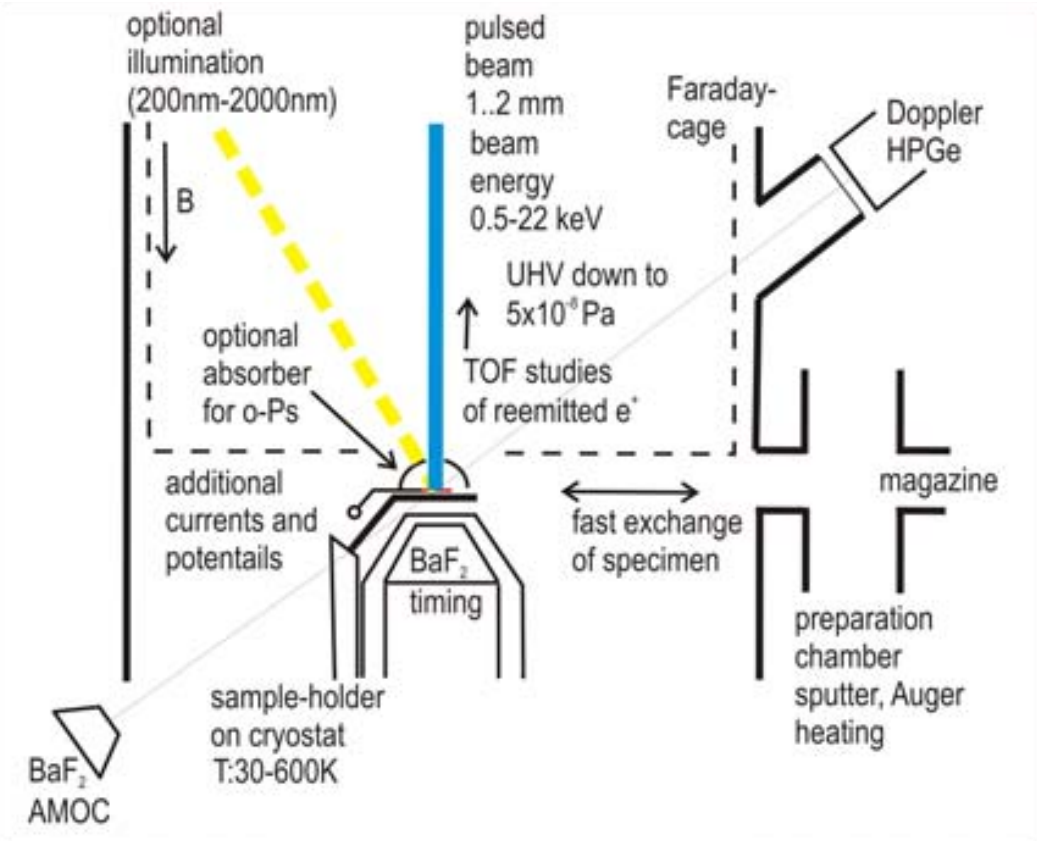

Figure 3.12: Schematic view of the target chamber (from [58]).

3.3 Performance of PLEPS

Table 3.2 summarizes the performance of PLEPS at the high intensity positron source NEPOMUC in the period from 2008-2010 before the upgrade of the source.

PLEPS @ NEPOMUC	
Implantation energies	$(0.1 - 22)\,\mathrm{keV}$
Time window	$20\,\mathrm{ns}$
Count rate	$\sim (5 - 10) \cdot 10^3\,\mathrm{s}^{-1}$
Time resolution	$(260 - 300)\,\mathrm{ps}$
Peak/Bg	$(5 - 30) \cdot 10^3$
Beam spot	$(2 - 3)\,\mathrm{mm}$
Acquisition times	
Single spectrum ($\sim 3.5 \cdot 10^6$ counts)	$\sim (5 - 10)\,\mathrm{min}$
Depth profile (20 spectra $\sim 3.5 \cdot 10^6$ counts)	$\sim (2 - 4)\,\mathrm{h}$

Table 3.2: Performance of PLEPS at the high intensity positron source NEPOMUC from 2008 until 2010.

After its installation and commissioning at NEPOMUC in 2008, PLEPS was operated as a user facility. Since 2008 about 200 depth profiles were measured in about 100 days of operation for a wide range of materials and for different applications. The following list contains a selection of typical measurements of PLEPS at NEPOMUC in those years.

defect identification in thin layered structures : $SrTiO_3$[64, 11, 65]; hetero-epitactic (LEPEVPE) GaN [66]; MgTi [67]; Mg[56] and Nb-doped Mg films[68]; CdTe [69];

defects structures in semiconductors: InN [70]; InN and GaN [71];

radiation induced defects in reactor materials: ODS and reactor steel [72]; SiC; W;

open volumes in polymers and membranes: Teflon [73]; aging effects in PIM [74]; Polyimide-Based Solvent Resistant Nanofiltration Membranes [75]; Ordered nanoporous membranes [76].

o-Ps emitters: nano-channels in Si [77]; Aerogel, Vycor, Germanate Xerogel, for anti–hydrogen production (AeGIS project) [78].

Chapter 4

Applications of PLEPS to selected problems in material science

In this chapter I review two investigations of positron lifetime spectroscopy with PLEPS before the upgrade:

a) Defect characterization in strontium titanate thin layers and crystals (section 4.1). The thin layers were investigated in collaboration with D. J. Keeble (University of Dundee, United Kingdom) and the results have been published in [11]. The measurements on strontium titanate crystals resulted from a collaboration with A. Gentils (Université Paris-Sud, France).
b) Determination of the average void size in permanently densified silica glasses (section 4.2) in collaboration with R. S. Brusa and M. Zanatta of the Universitá degli Studi di Trento, Italy, and published in [12].

4.1 Strontium titanate

In the last decades there has been a growing interest on strontium titanate ($SrTiO_3$, abbreviated as STO) because of its electronic properties for the production of oxide electronic devices [79, 80]. It is an electrical insulator (wide band gap of 3.3 eV), but shows a good conductivity when doped (for example with Nb) or by changing its stoichiometry [81, 82]. It is also one of the few titanates that exhibits a perfect (cubic) perovskite structure at room temperature. Therefore STO substrates are ideally suited to grow a wide variety of thin oxide films. It undergoes phase transition to tetragonal at 108 K, orthorombic at 65 K and rhombohedral at 35 K [83].

Vacancy like defects can influence or even control the transport- as well as the physical-properties in this material. Many investigations can be found in literature on the effect of oxygen vacancies, but little is known about the cation vacancies, the Sr vacancy, V_{Sr}, and the titanium vacancy, V_{Ti}. In particular, Ohnishi *et al.* [10] showed that varying the laser fluence in the pulsed laser deposition procedure can influence the stoichiometry of the film and also its electrical conductivity.

	Calculated	Experimental
Bulk	151 [84]	149–155 [84]
V_O^{2+}	166(170) [84]	—
V_{Ti}^{4-}	195(184) [84]	181 [11]
V_{Ti-O}	225 [84]	—
V_{Sr}^{2-}	279(279) [84]	$\sim$ 280 [11]
V_{Sr-O}	283 [84]	—

Table 4.1: Calculated and measured positron lifetimes (ps) for perfect lattice and different defects in $SrTiO_3$ from [84] and this work [11]. In parenthesis the values for the simulation with the relaxed structure are shown.

A wide variety of defects can be found in STO. The most important defects and the corresponding positron lifetimes are summarized in table 4.1. The positron – lifetime calculations have been performed using the MIKA doppler package [85] and the Arponen–Pajanen electron-positron enhancement factor with a 6x6x6 super-cell. Also the lattice relaxation was taken into account (values in parenthesis). The perovskite structure used in the positron – lifetime calculations is shown in figure 4.1 (from Mackie *et al.* [84]). The twelve fold coordinated A – site and the six fold coordinated B – site are occupied by Sr (blue spheres in the figure) Ti (green spheres) ions, respectively. Figure 4.2 shows the structure of the cation vacancies V_{Sr} and V_{Ti}. As can be inferred from figure 4.2, V_{Sr} presents a wider open volume than V_{Ti}, leading to a positron lifetime about 100 ps longer for V_{Sr}. Also, the positron lifetime in the oxygen – vacancy complexes, $V_{\mathrm{Sr-O}}$ and $V_{\mathrm{Ti-O}}$, differ strongly between A and B site. In particular, the positron lifetime in $V_{\mathrm{Sr-O}}$ is only a few ps longer than in V_{Sr} vacancy, whereas the lifetime in $V_{\mathrm{Ti-O}}$ is about 40 ps longer than in V_{Ti}. Therefore, the identification of defects in this material becomes an extremely challenging task, requiring a good time resolution as

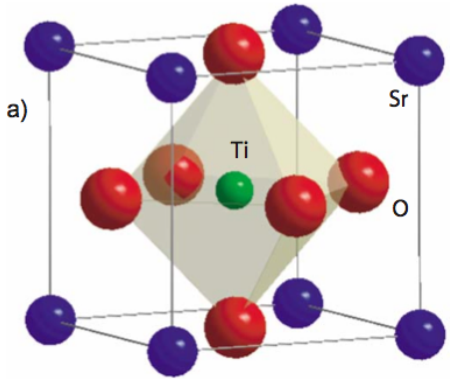

Figure 4.1: $SrTiO_3$ structure at room temperature from [84]. It is the typical perovskite oxide structure (ABO_3) with Sr and Ti in the A – and B – site, respectively.

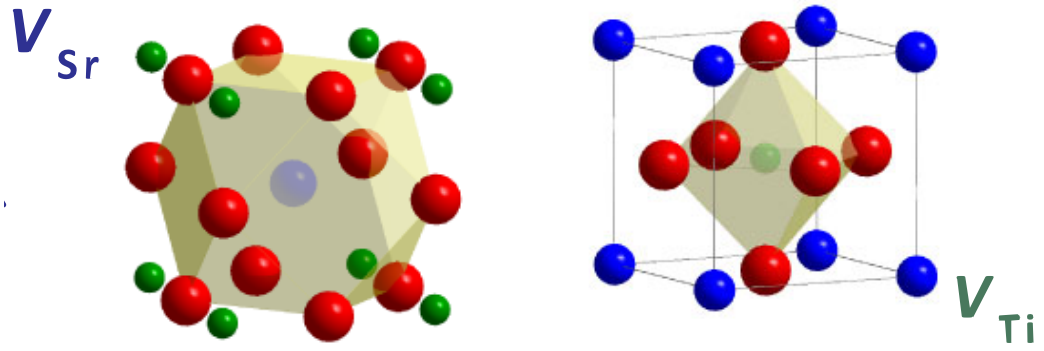

Figure 4.2: Structure of the strontium vacancy V_{Sr} (left) and the titanium vacancy V_{Ti} (right) in STO (from [11]).

well as a good peak-to-background ratio.

In the following we will discuss two investigations in STO: characterization of the defects created in the production of STO thin films deposited by Pulsed Laser Deposition (PLD) on a STO single crystal (section 4.1.1) and the defect evolution in a STO bulk sample after the same annealing treatment used for the PLD deposition of thin films (section 4.1.2).

4.1.1 Defect characterization in STO films

Pulsed Laser Deposition is a widely used technique to produce high quality oxide films. Ohnishi *et al.* [86] showed that the stoichiometry of the strontium titanate film can be varied by changing the laser fluence and that a variation in the stoichiometry causes an expansion of the lattice which is

directly correlated with the presence of cation defects [10].

Sample preparation

The samples for this investigation were deposited by Pulsed Laser Deposition on a $SrTiO_3$ (001) substrate using a KrF excimer laser and the fluence was varied in the range (1.00–2.50) J/cm^2. During the deposition the substrate was kept at 720 °C in 0.25 mbar oxygen and then cooled down at the same pressure. The thickness of the films was $\sim$200 nm and their structure were investigated with atomic force microscopy showing smooth step–terrace structure in the fluence range (1.67–2.50) J/cm^2 (layer–by–layer growth) and island growth for the lower fluences.

PALS measurements

The PALS measurements were performed in the energy range (1–18) keV corresponding to a mean implantation depth from about 8 nm to 800 nm with an average time resolution of (300 $\pm$ 20) ps. To ensure good statistics about $5 \cdot 10^6$ counts per spectrum were accumulated. In figure 4.3 the positron annihilation lifetime spectra of three selected samples at an implantation energy of 4 keV is shown.

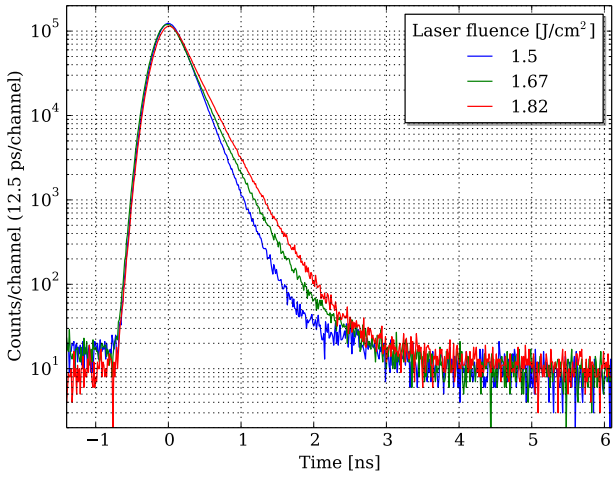

Figure 4.3: PALS spectra at 4 keV positron implantation energy for STO films deposited at different laser fluences.

All lifetime spectra could be decomposed into three components with a good variance. The intensity of the longest lifetime component was $< 1\,\%$ in all cases and therefore will be neglected in the following discussion. The mean

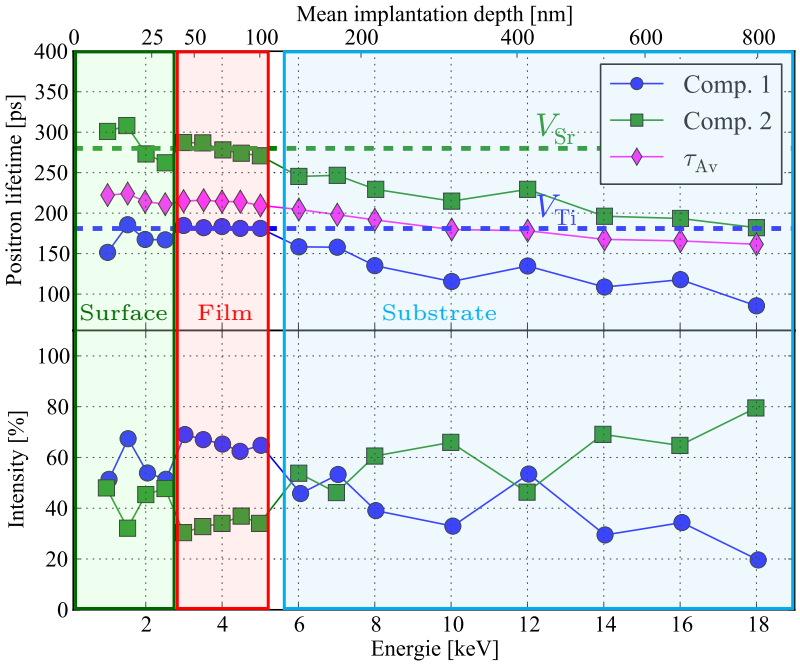

Figure 4.4: Positron lifetime and intensity of the two decomposed components and mean positron lifetime as a function of the positron implantation energy. The lines serve as guide for the eye. The dashed lines are the calculated positron lifetimes for V_{Sr} and V_{Ti} (see table 4.1).

positron lifetime and both the lifetime components and intensities are shown in figure 4.4. Both lifetime components increase with decreasing implantation energy and show a plateau in the range (3–5) keV, that corresponds to the film thickness, since the positron implantation profile extends to about $2\bar{z}$ and $\bar{z}(E = 5\,\mathrm{keV}) \approx 100\,\mathrm{nm}$. At implantation energies below 3 keV the first lifetime slightly decreases and the second one increases, probably due to larger defects and surface effects. The positrons start to annihilate in the substrate from energies above 5 keV.

For all samples the same trend for the two shorter lifetimes as in the upper panel of figure 4.4 was observed. Moreover, in the energy range corresponding to the film, total trapping into two defects was found. In order to minimize the statistical error, the fitted values in the film region were averaged and are shown in 4.5 as a function of the laser fluence (lifetimes and intensities, upper and lower panel, respectively). The two lifetimes of $\sim$ 181 ps and $\sim$ 280 ps are in excellent agreement with previous measurements [84] and with theoretical calculations (see table 4.1) and can be attributed to the V_{Ti} and V_{Sr}, respectively. The increase of the intensity of the V_{Sr} component in

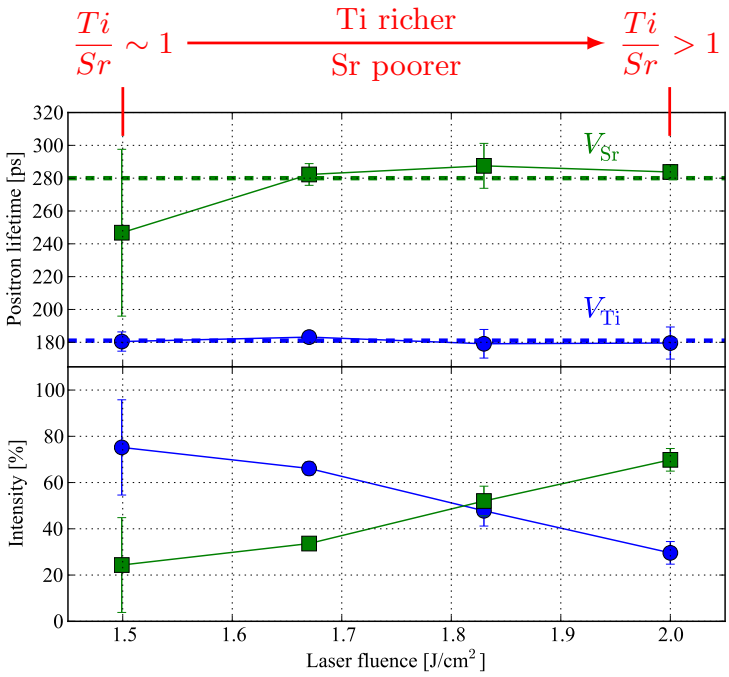

Figure 4.5: Average lifetimes (upper panel) and intensities (lower panel) over the energy range (3–5) keV as a function of the laser fluence. The dashed lines are the calculated positron lifetimes for V_{Sr} and V_{Ti} (see table 4.1).

the lower part of figure 4.5 with increasing laser fluence is consistent with the increase in the Ti/Sr ratio with fluence.

Since for all samples saturation trapping in the film was observed, it was not possible to calculate the concentration of the two defects with the standard trapping model. However, the ratio of the specific trapping rates could be estimated. In fact, when total trapping into two types of defect occurs, the ratio of their intensities is (a discussion of the trapping model can be found in appendix A):

$$\frac{I_1}{I_2} = \frac{\kappa_{D_1}}{\kappa_{D_2}} = \frac{\mu_{D_1}}{\mu_{D_2}} \cdot \frac{C_{D_1}}{C_{D_2}} \,. \tag{4.1}$$

No lattice expansion was observed in XRD measurements for the sample deposited with a laser fluence of 1.50 J/cm^2. Therefore, a Ti/Sr ratio and also a corresponding defects ratio of ~ 1 are expected for this sample. Consequently, using the intensities of figure 4.5, $I_1/I_2 = I_{V_{\mathrm{Ti}}}/I_{V_{\mathrm{Sr}}} = \mu_{V_{\mathrm{Ti}}}/\mu_{V_{\mathrm{Sr}}} \approx 3.6$. Considering the local charge of the defects (V_{Ti}^{4-} and V_{Sr}^{2-}), this value of the specific trapping rates ratio is plausible.

4.1.2 Defect evolution in STO crystals

Various methods are used to systematically improve the conductivity in STO crystals, which sensibly depends on the nature and the spatial distribution of lattice defects. In particular, the spatial distribution of defects is notoriously hard to engineer. To study the influence of different treatments on vacancy – like defects and their distribution, Gentils *et al.* [87] performed DBS and conventional positron lifetime measurements in differently prepared STO crystals. Two samples of these were also investigated with PLEPS:

As received STO (100) single crystal from Crystec GmbH.

Annealed in similar conditions as for the PLD procedure ($P_{O_2} = 10^{-5}$mbar and 750 °C) and then cooled down in high oxygen partial pressure ($P_{O_2} = 300$ mbar) to enhance the re-incorporation of oxygen. For the DBS measurements a slightly different sample was measured. In particular, this sample had a 5 nm thick $LaAl_2O_3$ layer on top of it (*IA-LAO*).

DBS and conventional lifetime measurements

A preliminary study using DBS and conventional lifetime measurements were performed by Gentils *et al.* [87]. In this paper, they reported a single lifetime of (154.4 ± 0.3) ps for the *IA-LAO*, while in the *as-received* sample two components were present ($\tau_1 = (109.1 \pm 5.4)\,ps$, $I_1 = 36\,\%$, $\tau_2 = (195.9 \pm 2.9)\,ps$, $I_2 = 64\,\%$). Their interpretation was that in the *IA-LAO* sample positrons annihilate from the defect free bulk state, while in the *as-received* they are mainly trapped in one defect, attributed to V_{Ti}.

The DBS measurements were performed with the slow positron beam at the CEMHTI Site Cyclotron in Orleans. The positron implantation energy was varied from 0.25 to 25 keV and the S and W parameter were measured in the momentum ranges $(0\text{-}2.80)\cdot10^{-3}\,m_0c$ and $(10.61\text{-}26.35)\cdot10^{-3}\,m_0c$, respectively [87]. These two parameters were fitted with VEPFIT [53], which gives information about the positron diffusion length and about the distribution of the defects present in the sample (see table 1. in [87]).

An extremely long diffusion length, characteristic of defect free samples, was observed in the *IA-LAO* sample. This was apparently consistent with their conventional positron lifetime measurements. Based on this interpretation of their measurements, they concluded that, surprisingly, after the deposition of a 5 nm thick LAO layer the native V_{Ti} defects are annealed out.

PLEPS measurements

To identify the defects type and better characterize their distribution, full depth profiles in the two aforementioned samples were measured with PLEPS. The positron implantation energy range was from 1 keV to 18 keV with an overall time resolution of about 270 ps. Very good statistic was achieved by collecting $> 7 \cdot 10^6$ (peak-to-background ratio $\sim 2 \cdot 10^4$)) and $> 4 \cdot 10^6$ (peak-to-background ratio $\sim 1.7 \cdot 10^4$)) for the *as-received* and *annealed* samples, respectively. Due to the higher peak-to-background ratio and to the better time resolution than in the conventional lifetime measurements of Gentils *et al.* [87], it was possible to decompose all the spectra with three lifetime components with good variance ($\chi^2 < 1.1$) at every implantation energy. As an example, in figure 4.6 a measured spectrum of the *as-received* sample at 16 keV positron implantation energy is shown together with the resolution function and with the corresponding lifetime components obtained from the fit. The residuals of the fit are also shown in the lower panel.

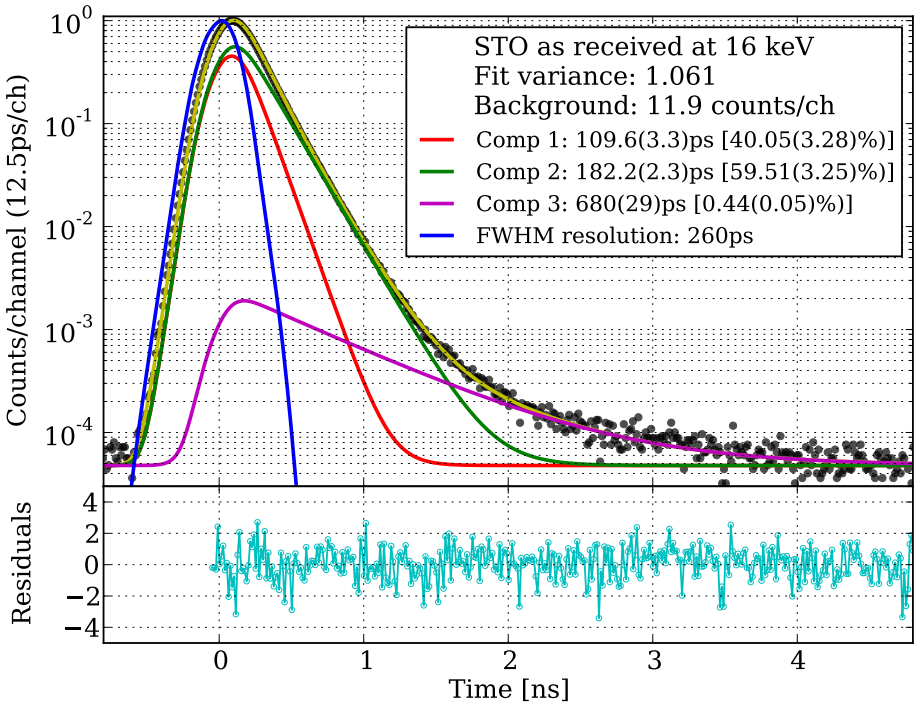

Figure 4.6: Positron lifetime spectrum of the as received sample measured at 16 keV positron implantation energy. The single components obtained from the fit and the instrument function (black line in the upper panel) are also plotted. The lower panel shows the residuals of the fit.

Since the intensity of the longest component is less than 1%, it can be neglected for the rest of the discussion. Only the two main components with the corresponding intensities are shown in figure 4.7 for the two investigated samples.

As-received sample: For the *as-received* sample, both lifetimes and intensities are constant in the bulk. To reduce the statistical error due to scatter in the measured data, the average values of both lifetimes and intensities in the range (11-18) keV are considered in the following discussion. In this region positrons are mainly trapped in a defect with a lifetime of (183.7 ± 1.4) ps, which agrees with the experimental value of the lifetime in V_{Ti} found in the PLD deposited thin films described in section 4.1.1. Differently from the investigation in section 4.1.1, a reduced bulk lifetime of (110.3 ± 0.9) ps with an intensity of $(41.5 \pm 1.0)\%$ is observed in the *as-received* sample. Given the short diffusion length (about 10 nm), the Standard Trapping Model (STM, see appendix A) with one type of defect can be applied and by using A.12 the bulk lifetime can be calculated (empty symbols in the upper left plot of figure 4.7). The average value of (144.4 ± 1.2) ps agrees well with the theoretical value (see table 4.1) and also with the experimental value of 141 ps reported by [88].

Using the STM it was also possible to calculate the trapping rate of the titanium vacancies $\kappa_{V_{\mathrm{Ti}}}$ with equation A.14 and, assuming a specific trapping rate $\mu_{V_{\mathrm{Ti}}}$ of $2 \cdot 10^{15}\,\mathrm{s}^{-1}$, also estimate their concentration. With the calculated value of τ_{Bulk}, the measured average and the defect lifetimes, the concentration can be written as:

$$c = \frac{\kappa}{\mu} = \frac{(\tau_{Av} - \tau_{Bulk})}{(\tau_2 - \tau_{Av})} \cdot \frac{1}{\mu \cdot \tau_{Bulk}} \tag{4.2}$$

giving a value of (1.26 ± 0.16) ppm.

Annealed sample: The results of the *annealed* sample have also shown a reduced bulk lifetime between 100 ps and 120 ps at every implantation energy with an almost constant intensity of about 45%. In the bulk, the second lifetime shows a slightly higher value than the as-received sample, increases to a constant value of about 227 ps in the energy range (4-8) keV before increasing rapidly towards the surface. Using Eq. A.12, the bulk lifetime was calculated in order to test the validity of the STM. Also in this case a very good agreement was found from the bulk to 4 keV. The average value of the calculated bulk lifetime in the energy range from 4 keV to 18 keV is in this case (146.1 ± 1.7) ps.

In the plateau region (from 4 keV to 8 keV) the average lifetime of the second component is (227 ± 2) ps which agrees with the calculated value for

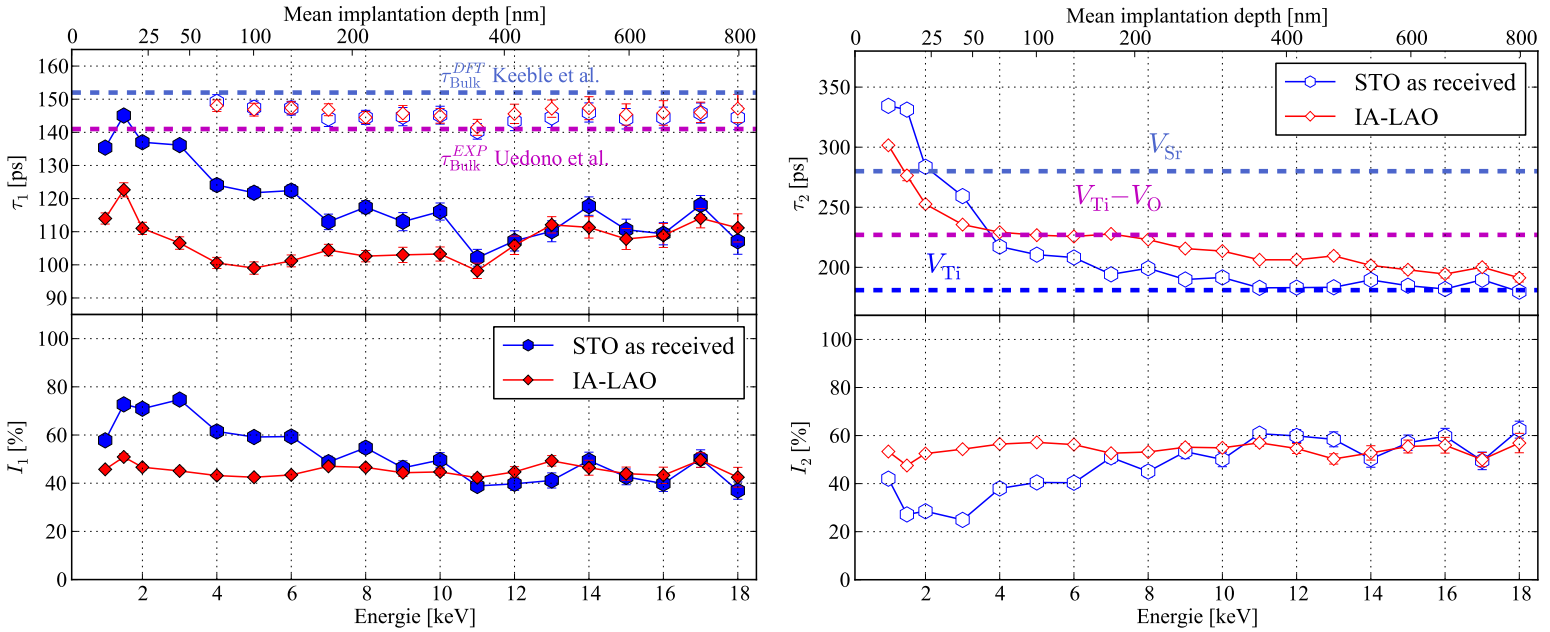

Figure 4.7: Positron lifetimes (upper panel) and intensities (lower panel) as a function of the positron implantation energy for the sample two investigated samples (component one on the left side, component two on the right). In the upper left plot: the open symbols represent the bulk lifetime calculated using the standard trapping model (Eq. A.12), the two dashed lines are the STO bulk lifetimes from DFT calculations (from Keeble *et al.* [11]) and experimentally measured by Uedono *et al.* [88]. The lines serve as guide to the eye.

the lifetime in titanium–oxygen divacancy $V_{\mathrm{Ti-O}}$. Assuming a specific trapping rate for this defect complex of about $(0.5 - 1.0) \cdot 10^{15}\mathrm{s}^{-1}$, corresponding to neutral and singly negatively charged defect, respectively, a concentration between $\approx (3 - 6)\,\mathrm{ppm}$ was estimated in the energy range from 4 keV to 8 keV.

For energies above 8 keV the τ_2 continues to decrease. It remains however always longer than the corresponding lifetime in the as received sample. This can be explained with a simple model assuming:

- the native V_{Ti} defects are still present in bulk
- a defective layer with a lifetime of ∼227 ps extending from the surface down to about 8 keV positron implantation energy
- short diffusion length (about 10 nm) as compared to the thickness of the defective layer ($\sim (300 - 400)\,\mathrm{nm}$).

A fraction of the positrons implanted at energies above 8 keV are stopped in the defective layer and probe this region with a positron lifetime of the second component of ∼227 ps. In particular, the fraction of positrons implanted in a layer with thickness z_{Layer} is given by

$$f_{Layer}(E) = \frac{\int_0^{z_{Layer}} P(z,E)\,dz}{\int_0^{\infty} P(z,E)\,dz} \tag{4.3}$$

where $P(z,E)$ is the positron implantation profile described in section 2.3.1 (see equation 2.31). Due to the shape of the implantation profile, even at the highest positron implantation energy available with PLEPS (18 keV), about 20 % of the positrons are thermalized in a layer with a thickness of 400 nm as illustrated in figure 4.8.

Consequently, since the second lifetime component in the defective layer and in the substrate are too close and can not be separated, the measured lifetime in the bulk is the weighted average of them:

$$\tau_2(E) = f_{Layer}(E) \cdot \tau_2^{Layer} + (1 - f_{Layer}(E)) \cdot \tau_2^{Substrate} \tag{4.4}$$

with $\tau_2^{Layer} = 227\,\mathrm{ps}$ and $\tau_2^{Substrate} = 184\,\mathrm{ps}$. The measured data points were fitted using equation 4.4 with z_{Layer} as a free parameter. The best fit was obtained with a thickness of 400 nm and, as evidenced by the dashed green curve in figure 4.9, the model fits the measured data very well. The two continuous green curves are obtained with layers of thickness $(400 \pm 20)\,\mathrm{nm}$.

The same reasoning applied to the trapping rate allows to express the total trapping rate $\kappa_{Total}(E)$ as a function of κ_{Layer}, $\kappa_{Substrate}$ and the fraction

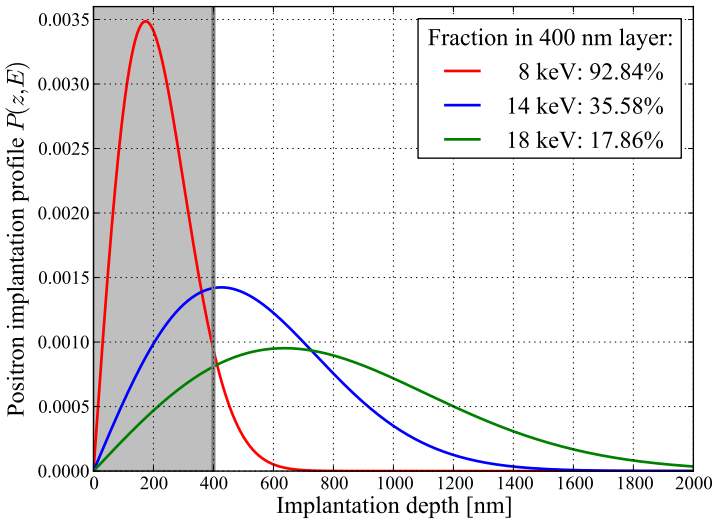

Figure 4.8: Positron implantation profile in STO

of positrons implanted in the layer f_{Layer}:

$$\kappa_{Total}(E) = f_{Layer} \cdot \kappa_{Layer} + (1 - f_{Layer}) \cdot \kappa_{Substrate} \tag{4.5}$$

In the STM the total trapping rate is:

$$\kappa_{Total} = \lambda_1 - \lambda_{Bulk} \,. \tag{4.6}$$

Combining these two equations the concentration in the substrate can be estimated with:

$$c_{Substate} = \frac{\kappa_{Substrate}}{\mu} = \frac{\lambda_1 - \lambda_{Bulk} - f_{Layer}(E) \cdot \kappa_{Layer}}{\mu \cdot (1 - f_{Layer}(E)) \cdot \kappa_{Substrate}} \,. \tag{4.7}$$

An average concentration of about (0.8 ± 0.3) ppm from 11 keV to 18 keV positron implantation energy was found. This value is very similar within the experimental errors to the concentration of V_{Ti} in the as-received sample. A possible interpretation is that the V_{Ti} native defects are not affected by the annealing procedure, which seems to introduce titanium – oxygen divacancies from the surface down to some hundreds of nm.

These results are apparently in disagreement with the conclusions reported in the paper of Gentils *et al.* [87]. However, as can be seen in figure 4.9, the second lifetime component found with the PLEPS measurement and the S parameter show exactly the same energy dependence. To resolve this issue the DBS measurement had to be reanalyzed in the light of the PLEPS results.

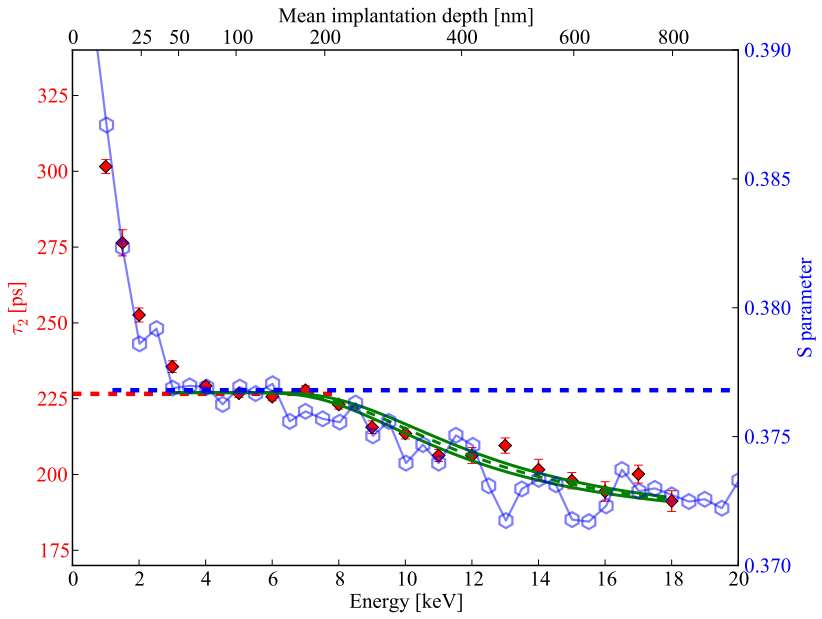

Figure 4.9: Comparison of the defect lifetime component (left axis) and the S parameter (right) as a function of the implantation energy. The dashed green line is the positron lifetime calculated with equation 4.4 and a layer thickness of 400 nm (the two continuous green lines are the same as the dashed curve but with thickness (400 ± 20) nm).

Reevaluation of the DBS measurements

The measured S parameter and the best fit obtained with VEPFIT are illustrated in figure 4.10. The results are summarized in table 4.2.

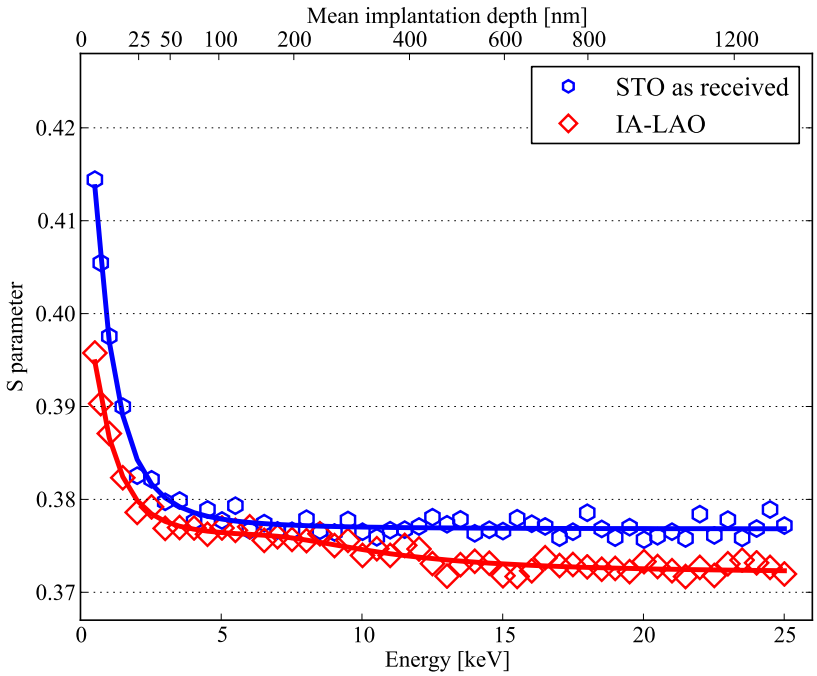

Figure 4.10: S parameter as a function of the positron implantation energy for the as received and IA-LAO samples. The measured data are shown with points, the lines are the best fits obtained with VEPFIT.

The *as-received* sample has a constant S parameter from the bulk to about 4 keV where a steep increase starts towards the surface. This trend can be interpreted as a homogeneous defect distribution with a short diffusion length

Sample	Layer 1			Layer 2		χ^2_{Red}(S)
	S_1	L^1_+ [nm]	B_1 [nm]	S_2	L^2_+ [nm]	
As-received	0.37682(15)	8.4(3)				0.76
IA-LAO	0.37591(27)	8.6(6)	340(40)	0.372070(24)	8(X)	0.52

Table 4.2: Results of VEPFIT analysis. The S parameter, the diffusion length L^i_+ and the upper boundary B_i of each layer is reported for the two samples. The fixed parameters are marked with a X. The last column shows the reduced chi-square of the fit.

as pointed out by the VEPFIT analysis. Furthermore, the comparison of the PALS measurements with the results obtained by DBS is consistent. In fact, τ_2 presents the same steep increase as the S parameter with decreasing positron implantation energy, which can only be interpreted by a short positron diffusion length. The S parameter of the *IA-LAO* sample has a lower value than the *as-received* in the bulk region, shows a plateau with a slightly higher value between 4 keV and 8 keV and then increases again towards the surface. In the article of Gentils *et al.* [87] a very long diffusion length of (200.2 ± 15.3) nm is reported. This result is probably affected by the assumption of this sample as "defect free" and by fitting the S parameter in the range (2.5-25.0) keV, thereby completely neglecting the back diffusion of the positrons to the surface. Considering the whole energy range, it was possible to fit the measured data only by fixing the diffusion length of the substrate obtaining a first layer of thickness (340±40) nm with a diffusion length comparable to the one obtained in the bulk. These results are consistent with the PLEPS lifetime measurements. In fact, both methods demonstrated the existence of a defective layer of about 400 nm thickness on top of a substrate that contains ∼1 ppm of the native titanium vacancies. Furthermore, the apparent discrepancy between the conventional lifetime and the PLEPS measurements can be explained by considering the mean implantation depth that is obtained with a ^{22}Na radioactive source. In fact, the characteristic implantation depth for STO using equation 2.1 is about 50 μm, meaning that the positrons are implanted mainly in the bulk of the sample and only a negligible fraction senses the region affected by the annealing treatment. Another reason for the disagreement of the two techniques is also the much better overall quality of the lifetime spectra measured with PLEPS (peak-to-background ratio of $\sim (1.7 - 2.0) \cdot 10^4$) and the poor statistics of the conventional lifetime measurements, since only approximately two million counts were collected for each spectrum.

4.1.3 Conclusions

Defect characterization in PLD deposited STO films

In the PLD deposited STO thin films investigation total trapping into two kind of defects was observed with PLEPS. The two lifetimes of 181 ps and ∼280 ps were attributed to the titanium vacancy and strontium vacancy, respectively. Moreover, the measurements as a function of the laser fluence allowed to determine the ratio of the specific trapping rates characteristic of these two defects ($\mu_{V_{\mathrm{Ti}}}/\mu_{V_{\mathrm{Sr}}} \approx 3.6$).

Defect evolution in STO crystal

The investigation in STO crystals subjected to different treatments to improve their conductivity evidenced the power of the positron lifetime technique in combination with a pulsed beam. In particular, the measurements performed with PLEPS and the DBS data showed:

- V_{Ti} are present in the as received sample with a concentration of (1.26 ± 0.16) ppm.
- after the annealing treatment in low oxygen partial pressure the native defects are not removed and a layer of titanium-oxygen divacancies (with positron lifetime of 227 ± 2) ps) appear from the surface to about 400 nm with a concentration between $\approx (3 - 6)$ ppm depending on the specific trapping rate assumed for the $V_{\mathrm{Ti-O}}$ defect.
- the calculated bulk lifetimes in STO of (144.4 ± 1.2) ps and (146.1 ± 1.7) ps for the as-received and annealed samples, respectively, are in excellent agreement with the experimental value of Uedono *et al.* [88].

4.2 Permanently densified silica glass

Although glasses have been intensively studied during the last decades, there are still some open questions about their structures. Crystals can be described by a repetition of some building blocks, usually composed by only few atoms, which are called the unit cell. Differently from crystalline materials, in glasses the periodicity is broken and they are therefore known as disordered materials.

However, even glasses show some degree of order. For example, vitreous silica can be described as an open network of SiO_4 tetrahedra (highlighted by the green circle in figure 4.11) similar to those of the crystalline form.

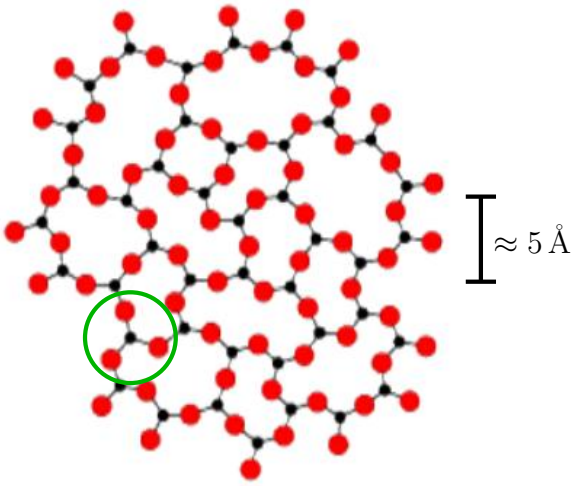

Figure 4.11: Structure of vitreous silica from [89]. The black and red dots show Si and O atoms, respectively.

Three ranges with very different properties can be identified [89, 90]:

- Short Range Order (SRO): between 2 Å and 5 Å, namely the atom and the nearest neighbors. This structure level has been thoroughly investigated and can be described by the number of nearest neighbor atoms and by the distributions of the bond-length and -angle.
- Medium Range Order (MRO): from 5 Å to 20 Å. It depends on how the tetrahedra are connected to each other and on the interstitial voids between them. The existence of a MRO is evidenced by the presence of a First Sharp Diffraction Peak (FSDP) in the static structure factor $S(Q)$.

- Long Range Structure (LRS): for distances $>20\,\text{Å}$, where inhomogeneities in the structure are observed.

Different models have been proposed to describe the structure of SiO_2 and its evolution as a function of the density when subjected to densification. In this work, permanently densified silica glasses were investigated by X-ray diffraction and positron annihilation lifetime spectroscopy.

Sample preparation

The samples are normal silica glasses (commercial grade Spectrosil, cylinders of $\varnothing 4 \times 4\,\text{mm}$) subjected to a densification process using a multianvil apparatus. The pressure was increased with a rate of 1 GPa/hour up to the desired value. The sample was heated at the maximum pressure at 770 K (heating rate 50 K/min) for 10 min and then the pressure was decreased with a rate of 0.3 GPa/hour. The density of the compressed samples was measured with the Archimedes method (ethanol as immersion fluid) and was found to be stable over few years. The obtained values are shown in table 4.3.

4.2.1 X-ray diffraction measurements

These measurements were performed with a two axis diffractometer using the Ag K_{ff} radiation ($\lambda = 0.5608\,\text{Å}$) in combination with a graphite crystal monochromator. The results obtained with this technique are shown in figure 4.12 and are briefly discussed in the next paragraphs.

Figure 4.12 (a) shows the static structure factor $S(Q)$ of the investigated samples. The differences in the four curves for high Q is very small, indicating no change in the SRO. This fact is also emphasized by the calculation of the number density function $N(r)$, which gives the number of atoms at a distance r (see figure 4.12 (b)). No difference is observe in the four samples up to a distance of about r_{OO}, meaning that the SiO_4 tethaedra are barely affected by the densification process.

On the other hand, a change in the MRO is evidenced by the shift in the position Q_1 of the FSDP. This feature is clearly visible by studying the low-Q portion of the static structure factor (see figure 4.12 (c)). With increasing density, Q_1 shifts to higher Q and reaches a value $\sim$20 % higher than normal glass for the 8 GPa sample. In this graph also the diffraction patterns of crystalline SiO_2 in the $\alpha-$quartz and $\alpha-$cristobalite phases are plotted. It is interesting to note that the position of the FSDP of the samples subjected to a pressure 4 GPa and 8 GPa is in good agreement with the one of $\alpha-$cristobalite and $\alpha-$quartz, respectively.

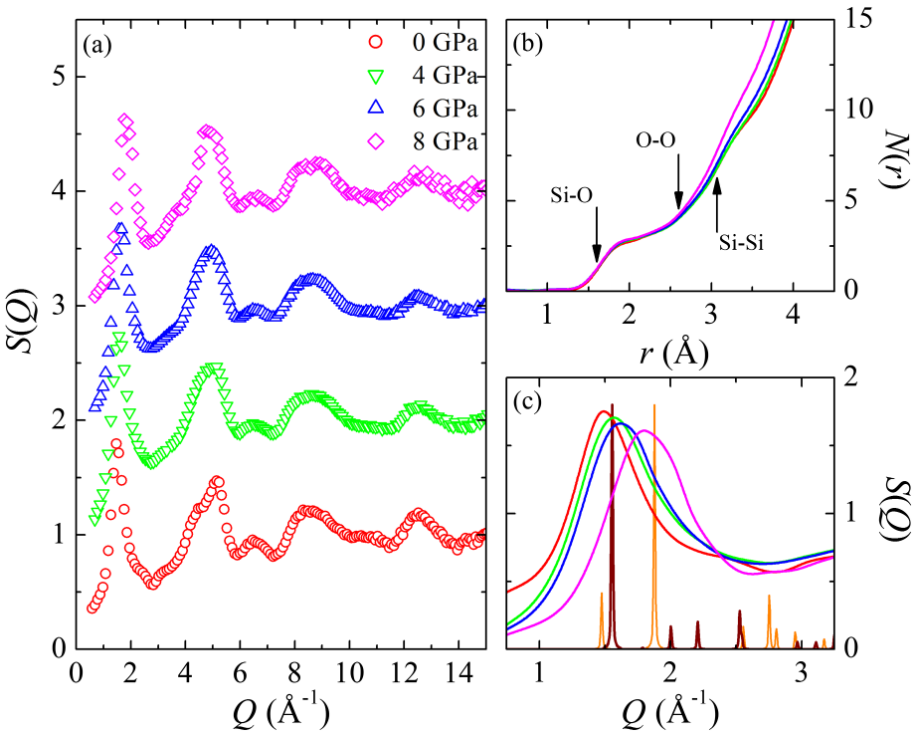

Figure 4.12: Results of the X-ray diffraction measurements for normal SiO_2 and for the samples subjected to a pressure of 4, 6 and 8 GPa (the colors in all three plots is as described in the legend of figure (a)): (a) static structure factor $S(Q)$. (b) Number distribution function $N(r)$. The bond lengths are marked by the arrows: $r_{SiO} = 1.60$ Å,$r_{OO} = 2.50$ Å and $r_{SiSi} = 3.07$ Å. (c) The low-Q portion of the structure factor from (a) enlarged and compared to crystalline SiO_2 in the α – quartz (orange line) and α – cristobalite (brown line) phases (from [12]).

To find a correlation between the shift of the FSDP and the evolution of the inter-tetrahedral voids, a measurement of the average void size was necessary. Therefore, PALS measurements with PLEPS have been performed.

4.2.2 PLEPS measurements

PLEPS measurements were performed at 16 keV and 18 keV positron implantation energy corresponding to average implantation depths between 1.2 μm and 1.8 μm. The instrument function had a FWHM of about 260 ps for both positron implantation energies.

Figure 4.13, shows the comparison of the positron annihilation lifetime spectra measured at 16 keV positron implantation energy for the four investigated samples. From this comparison a dramatic decrease in the long lifetime

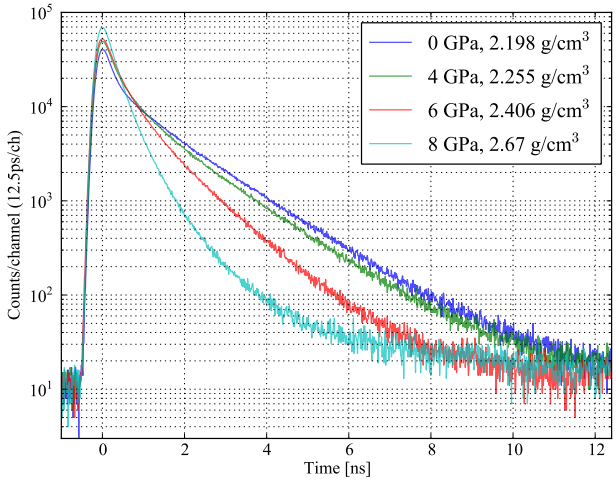

Figure 4.13: Positron lifetime spectra of the v-SiO_2 samples at 16 keV positron implantation energy.

component with increasing density can be inferred.

The positron annihilation lifetime spectra were analyzed by means of both POSWIN [91] and LT [92] and the results of the two programs were in perfect agreement. An example of the decomposition obtained by the POSWIN analysis is shown in figure 4.14(a) for the sample subjected to 6 GPa measured at 16 keV positron implantation energy. Figure 4.14(b) shows the positron lifetime spectra of the sample subjected to a pressure of 6 GPa at 16 keV and 18 keV positron implantation energy. Since no difference between these two spectra was observed, the lifetime components and the corresponding intensities found with the fitting procedure were averaged.

Table 4.3 summarizes the fit results for all samples. The virgin sample was fitted with three components and showed the typical lifetimes of SiO_2 glass: a short component ($\tau_1 = 145$ ps) that can be attributed to p-Ps and annihilation of free positrons, an intermediate component ($\tau_2 = 730$ ps) coming from annihilation in small voids and a longer one ($\tau_3 = 1623$ ps) due to o-Ps pick–off in the intrinsic voids of the amorphous structure. With increasing density, the first component becomes longer (from 145 ps to 195 ps at 6 GPa and 169 ps at 8 GPa) and the corresponding intensity increases from 25.5 % to 39.7 %. The intermediate lifetime decreases from 730 ps to 570 ps at 6 GPa and then again to 359 ps at 8 GPa with an intensity increase from 18.7 % to 45.3 % at the maximal density. The third component decreases from the original value in glasses to 781 ps at 8 GPa. Also its intensity is much lower after the compression (from 55.8 % to 13.9 %). A good fit of the spectra of the sample subjected at 8 GPa could be obtained only by adding a fourth

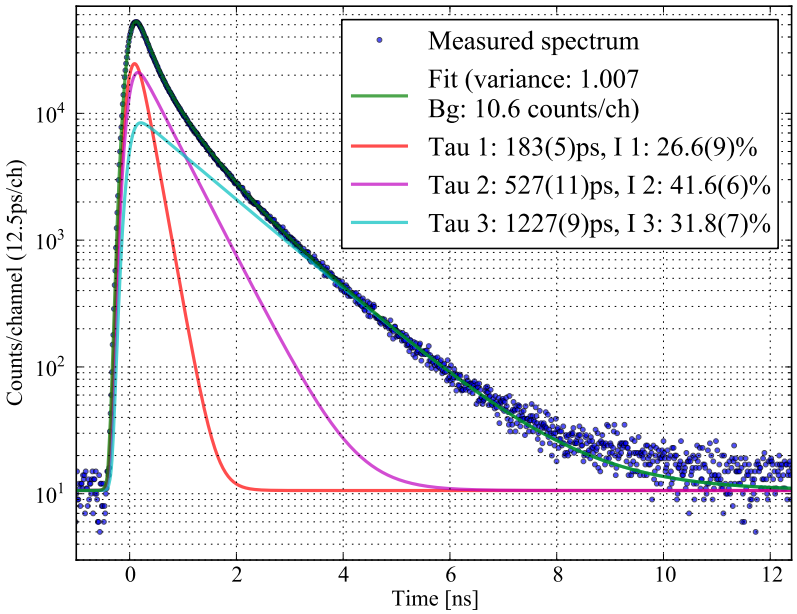

(a) Positron lifetime spectrum and positron lifetimes obtained from the fit for the sample subjected to a pressure of 6 GPa at a positron implantation energy of 16 keV.

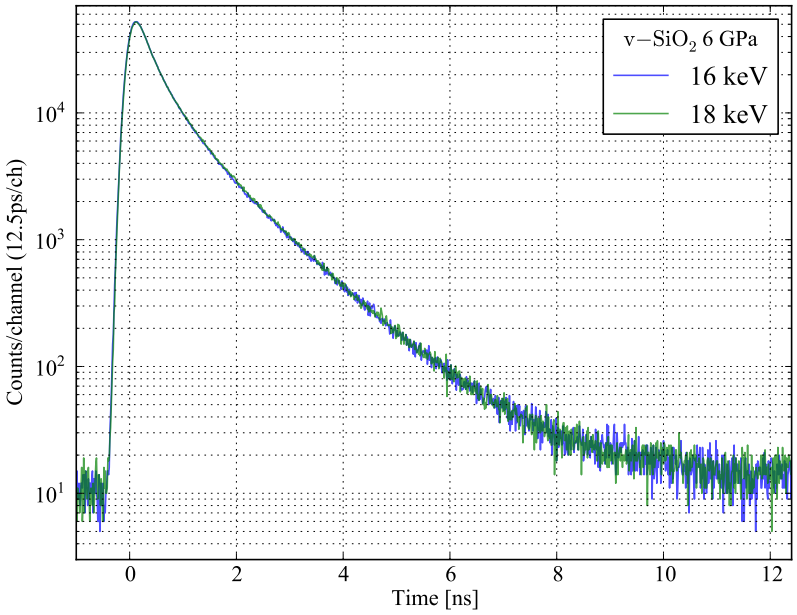

(b) Comparison of the positron lifetime spectra of the 6 GPa sample measured at 16 keV and 18 keV positron implantation energy.

Figure 4.14: Positron lifetime spectra of the v-SiO_2 sample subjected to 6 GPa.

component of (3590 ± 80) ps with an intensity of 1.1 %.

Since this study is focused on the evolution of the void size as a function of the density, only the lifetime component that can be ascribed to the annihilation of ortho-positronium will be discussed in detail. In particular, τ_3 (and τ_4 for the 8 GPa sample) obtained by the fitting procedure is related to the void size by the Tao – Eldrup model described in detail in section 2.4. The long τ_4 component for the 8 GPa sample could be attributed to small cracks that appeared at this pressure. Since the intensity of this lifetime component is very small (∼1 %) it is neglected in the rest of the discussion.

The pick – off lifetime can be expressed as (from equation 2.35):

$$\tau_{pickoff} \approx \frac{1}{2} \cdot \left[1 - \frac{R}{R + \Delta R} + \frac{1}{2\pi} \cdot \sin\left(\frac{2\pi R}{R + \Delta R} \right) \right]^{-1} . \qquad (4.8)$$

The parameter ΔR was set to 0.168 nm. Figure 4.15 shows the evolution of the void volume, assumed as spherical ($V = \frac{4}{3}\pi R^3$), as a function of the density. The void volume shows a linear trend and an increase of the density of ∼22 % gives rise to a shrinking of the void to ∼12 % of the initial value (from about 66 Å^3 to 9 Å^3).

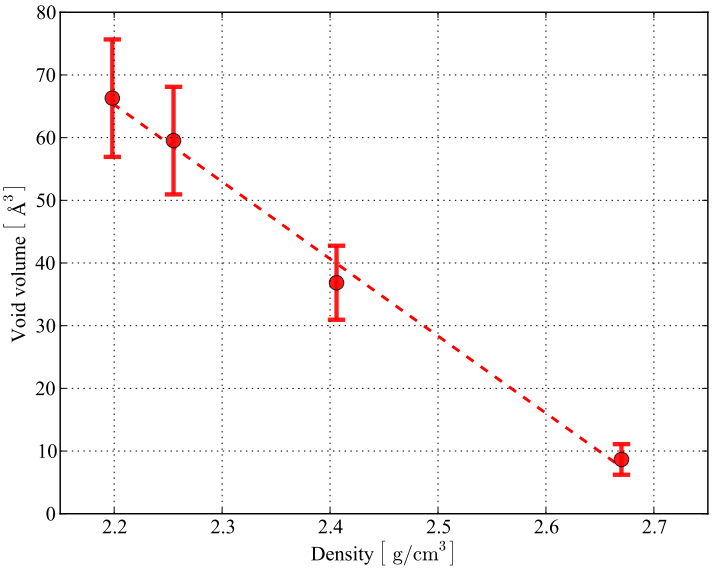

Figure 4.15: Void volume as a function of the sample density. A spherical void was assumed ($V = \frac{4}{3}\pi R^3$) and the void radius R was calculated with equation 4.8.

Sample	Density	τ_1	τ_2	τ_3	τ_4	I_1	I_2	I_3	I_4
	$[g/cm^3]$	[ps]	[ps]	[ps]	[ps]	%	%	%	%
0 GPa	2.198(5)	145(3)	730(30)	1623(6)	—	25.5(5)	18.7(5)	55.8(6)	—
4 GPa	2.255(5)	165(3)	571(10)	1540(20)	—	26.4(3)	28.9(1.5)	47.7(1.7)	—
6 GPa	2.406(5)	195(12)	570(50)	1250(20)	—	29.3(3)	40.9(0.7)	29.8(2.0)	—
8 GPa	2.67(1)	169(6)	359(5)	781(14)	3590(80)	39.7(4.0)	45.3(4.0)	13.9(0.2)	1.1(0.1)

Table 4.3: Results of the fitting procedure for the v-SiO_2 samples. The average values of the lifetime components τ_i and the corresponding intensities I_i of the measurements at 16 and 18 keV are shown.

4.2.3 Conclusions

In normal silica glasses an average void size $R = (2.5 \pm 0.2)$ Å was measured. A shrinking of the voids to ∼12 % of the non – densified sample was observed with an increase in the density of about 22 %.

The results obtained with the two techniques suggest that the v-SiO_2 structure can be described by an incompressible and a compressible part. The incompressible part is formed by SiO_4 tetrahedra that are not affected by the densification process up to 8 GPa. The compressible part can be ascribed to the inter-tetrahedral voids and its reduction can be explained by the rotation of the tetrahedra, which fill the voids.

One of the model proposed to describe the glass structure is the void – cluster model [93]. In this framework the voids are surrounded by SiO_4 tetrahedra at a distance D and separated by the Si – Si distance. Furthermore, the origin of the FSDP is the chemical ordering of the clusters around the voids and its position Q_1 can be written as:

$$Q_1 = \frac{3\pi}{2d}\left(\frac{3}{2} - \frac{D}{2d}\right), \tag{4.9}$$

where $d = r_{\mathrm{SiSi}} = 3.07$ Å and D is the distance between the center of the void and the tetrahedra and can be estimated using the PALS results. The distance D can be decomposed into two terms: *i*) R, the average void radius found with the Tao – Eldrup model and *ii*) r_{eff}, a screening factor which takes into account the portion of the void that is not accessible to the positrons due to the Coulomb potential of the ions [12]. This parameter can be estimated comparing the void radius measured in the normal glass with the geometrical Si – void center distance calculated in β – cristobalite. The value for r_{eff} found with this procedure is ∼0.59 Å and it is then possible to calculate D as a function of the density (shown in the lower inset of figure 4.16). The calculated position of the FSDP using equation 4.9 and the estimated D values are reported in figure 4.16 in red open circles. In this figure also the Q_1 measured by XRD (blue open diamonds) and by neutron diffraction from [94] (black open squares) are plotted. From this figure it is evident that the agreement between the measured and calculated values is perfect and, therefore, the description of the structure of permanently densified v-SiO_2 within the void – cluster model seems to be correct.

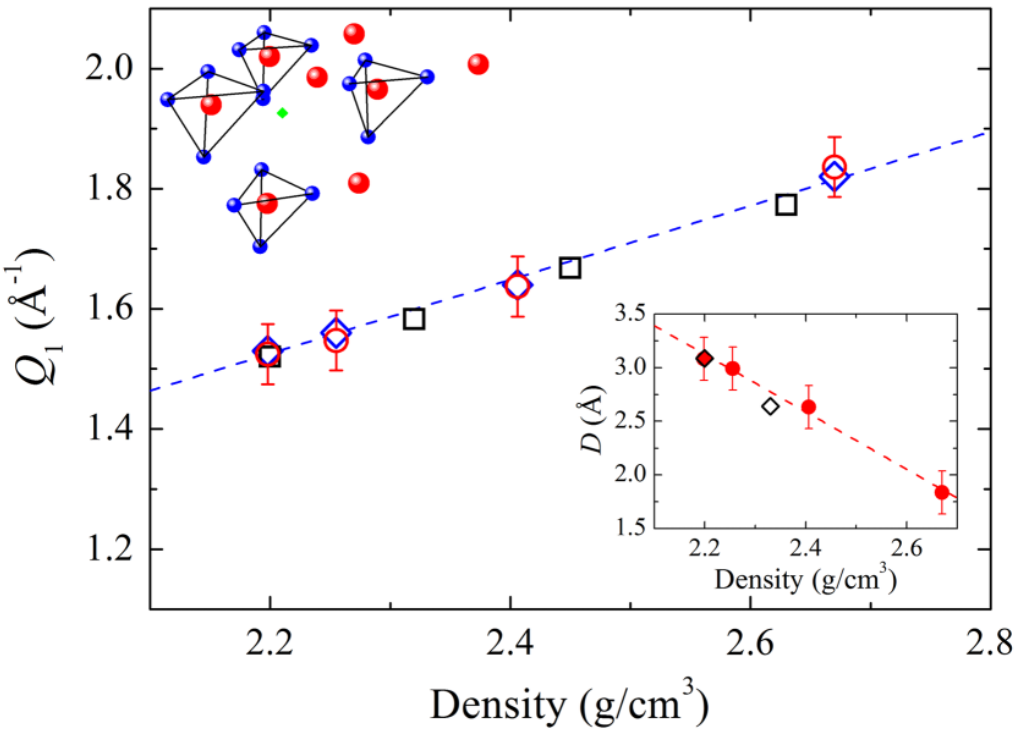

Figure 4.16: Position of the FSDP (Q_1) measured with XRD (blue open diamonds) and neutron diffraction from [94] (black open squares) compared with the calculations using the void – cluster model (equation 4.9, red open circles). The upper left inset shows the structure of β – cristobalite. Si and O atoms are shown in red and blue, respectively. The green dot represents the center of the void. In the lower right inset the Si – void center distance D is plotted as a function of the density for permanently densified v-SiO_2 (red circles). The black diamonds are the calculated geometrical distances D for α and β – cristobalite. From [12].

Chapter 5

Limits of PLEPS

The measurements performed in the years from 2008 until 2010 evidenced some limits of PLEPS, especially when dealing with:

Different types of defects: in many complex systems the lifetimes of different defects are very similar, see for example table 5.1 in which the lifetimes of the defects in $6H$-SiC and $SrTiO_3$ are summarized. In such cases, if the resolution of the system is not good enough to resolve two close lifetimes, only an average lifetime may be obtained from the fit.

$6H$-SiC			$SrTiO_3$		
Bulk	144	$\delta = \frac{\tau_i}{\tau_{i-1}}$	Bulk	152	$\delta = \frac{\tau_i}{\tau_{i-1}}$
V_{C}	153	1.06	V_{O}	161	1.06
$V_{\mathrm{C-C}}$	161	1.05	V_{Ti}	181	1.12
V_{Si}	192-194	1.20	$V_{\mathrm{Ti-O}}$	225	1.24
$V_{\mathrm{Si-Si}}$	196	1.01	V_{Sr}	281	1.25
$V_{\mathrm{Si-C}}$	214	1.09	$V_{\mathrm{Sr-O}}$	283	1.01

Table 5.1: Positron lifetimes in 6H-SiC (from [95]) and $SrTiO_3$ (monovacancies from [11] and this study, vacancy complexes from [64]).

Multi-layered systems: due to the width of the implantation profile, when investigating thin layers or multi-layered systems, it is not always possible to tune the implantation energy in such way that all the positrons annihilate in the same material. Thus, positrons annihilating in the layer and in the substrate contribute to the lifetime spectrum. If the corresponding lifetimes are similar, it may not be possible to resolve them and as in

the previous case an average lifetime results from the fit. Moreover, positron diffusion and internal electric fields can complicate the interpretation of the lifetime data even further [57, 41].

Long lifetimes: due to the 20 ns time window in the case of lifetimes longer than approximately 3 ns an increase of the background is observed.

In order to increase the number of components that can be resolved in a given sample, not only the time resolution has to be improved, but also the peak-to-background ratio. In fact, as shown by Istratov and Vyvenko [96], the number of components that can be resolved and the resolution δ of two close lifetime components τ_i and τ_{i-1} $\left(\delta = \frac{\tau_i}{\tau_{i-1}}\right)$ of the fitting procedure are directly correlated with the peak-to-background ratio. Furthermore, according to Istratov and Vyvenko [96], the resolution δ depends also on the domain of the system, which is defined as the ratio between the longest and the shortest lifetimes, τ_{MAX} and τ_{MIN}, respectively, present in the lifetime spectrum. The resolution for selected peak-to-background ratios and domains are shown in table 5.2 (from [96]).

Considering that the peak-to-background ratio of the measurements done with the previous version of PLEPS, operated with a ^{22}Na source, was about $2 \cdot 10^3$, a resolution factor of 1.27 could be obtained with a $\tau_{MAX}/\tau_{MIN} = 2$, which is the typical domain for metals and semiconductors. With the NEPOMUC source the peak-to-background ratio is a factor 10 higher, giving a δ of 1.20 considering the same domain. This means that even with PLEPS at NEPOMUC it is not possible to resolve all the defect lifetimes in SiC and STO (see column three and six of table 5.1, respectively).

Fortunately, in many cases certain defects can be ruled out (*e. g.*: positive charge state of some defects in semiconductors and insulators, information on the nature of the defects obtained with other techniques, use of reference

	τ_{MAX}/τ_{MIN}	
peak-to-background	2	5
10^2	1.44	1.74
10^3	1.27	1.45
10^4	1.20	1.32

Table 5.2: Resolution δ of the exponential fitting according to Istratov and Vyvenko [96].

samples with known defects) and, consequently, the type of defect can be identified. On the other hand, if larger defects are present (for example, in irradiated materials) or in semiconductors like STO (see table 5.1), the domain τ_{MAX}/τ_{MIN} can be >2, leading to δ typically in the range 1.20–1.32 even for PLEPS operated at NEPOMUC with its excellent peak-to-background ratio of $\approx 10^4$. One example of this kind of issue is described in section 4.1.2, which concerns measurements on STO crystals subjected to different treatments.

Therefore, in order to be able to resolve more lifetimes, an improvement of the peak-to-background ratio is needed. There are two ways to improve the peak-to-background ratio: *a*) increase the count rate and *b*) reduce the background. The maximum count rate is ultimately limited by the intensity of the remoderated reactor beam. Also the further reduction of the background is mainly limited by constructive constrains which can not be easily modified.

As the peak-to-background ratio increases, satellite structures not visible at lower peak-to-background-ratios appear in the lifetime spectra. This problem is illustrated in figure 5.1 (left), which shows positron annihilation lifetime spectra of a gold target at 4 keV, 8 keV, 12 keV and 16 keV positron implantation energy. Due to the high Z, the backscattering coefficient in

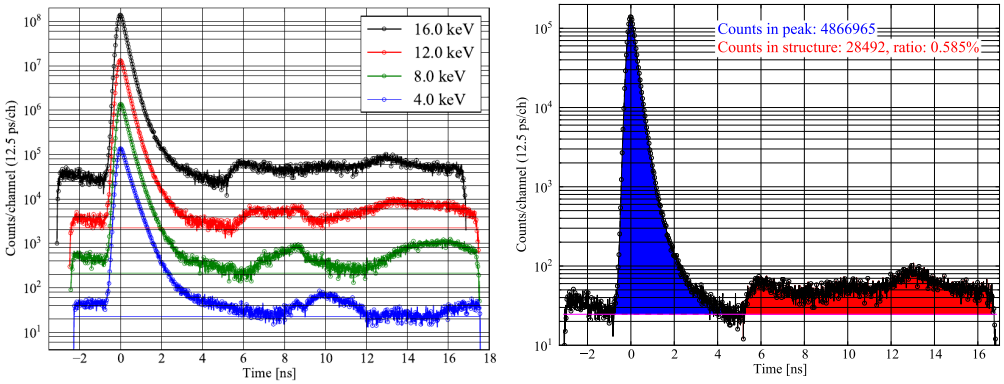

Figure 5.1: Left: Positron lifetime spectra of a gold target at different implantation energies. Right: positron lifetime spectrum at 16 keV implantation energy. The number of counts in the peak (blue) and in the satellite structure (red) are shown.

gold can be as high as 35% at 16 keV positron implantation energy [97, 98]. Nevertheless, already with the setup in the years 2008-2010 the contribution of the satellite structures (highlighted in red) was less than 1% of the number of counts in the lifetime peak (blue), as can be seen in figure 5.1 (right). Even though the amount of such events is very small, in some cases these

structures can render the data analysis difficult. This issue is one of the main topics of this thesis and is described in detail in chapter 6.

The second limitation of the setup in the years 2008-2010 concerned the measurements with long lifetimes, especially when free volumes with different sizes, and consequently more than one long lifetime component, are present. Istratov and Vyvenko [96] have shown that not only the resolution factor δ, but also the length of the time window plays a crucial role in the determination of long lifetimes. This problem is illustrated in the two plots of figure

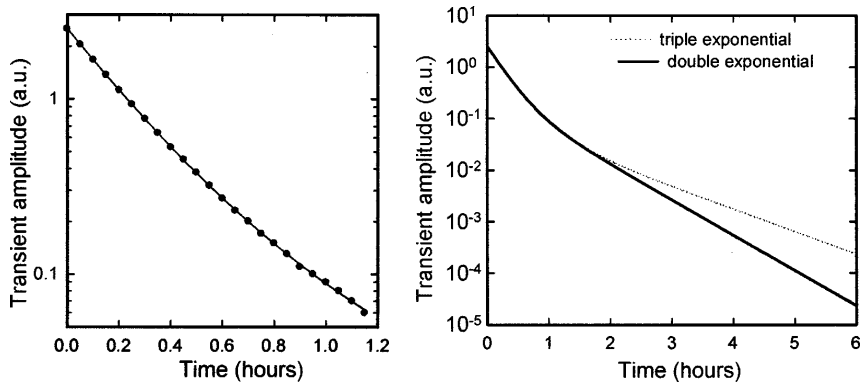

Figure 5.2: Comparison of exponential decay functions from [96]: 24 data points are fitted with a double ($f_2(t) = 2.202\exp(-4.45t) + 0.305\exp(-1.58t)$, dashed line) and a triple exponential function ($f_3(t) = 0.0951\exp(-t) + 0.8607\exp(-3t) + 1.5576\exp(-5t)$, solid line) but the differences are smaller than the line width (left). On the right the same functions are plotted in a longer time range and the two functions can be well separated for $t > 2\,\mathrm{h}$.

5.2. On the left, 24 data points were fitted with a double and a triple exponential function with completely different decay constants and amplitudes, but the difference between them is smaller than the width of the line. On the right hand side, the same functions are plotted in a wider time range and one can clearly see that they become distinguishable only for $t > 2\,\mathrm{h}$. This is a very important problem when dealing with samples where o-Ps is formed, especially if in a time window of 20 ns the longest lifetimes are $> (6 - 8)\,\mathrm{ns}$.

Chapter 6

Simulations of the background in the lifetime spectra of PLEPS

From the first version of PLEPS computer simulations were intensively employed, in particular in the development of the pulsing system and the beam transport. For these tasks computer codes like SIMION [99] are sufficient [1, 2, 55].

As pointed out in the preceding chapter, the background in the lifetime spectra due to positrons backscattered from the sample is now one of the main problems in the evaluation of positron lifetime spectra measured with PLEPS. In order to understand the provenience of these structures and to figure out possible countermeasures, comprehensive computer simulations of the target chamber of PLEPS were needed. These simulations require highly sophisticated software which permits not only the calculation of the trajectories of positron in electromagnetic fields, but also their interaction with matter, such as the Geant4 toolkit [100, 101]. This software, which is briefly described in section 6.1, allows the tracking of particles and electromagnetic radiation through matter also in presence of electric and magnetic fields.

The modeling of the target chamber for the calculation of the electric and magnetic fields was performed with COMSOL Multiphysics © [102] (see section 6.2).

The details of the Geant4 simulations and the comparison between the results of the simulations and the measured spectra are discussed in 6.4. Part of the results have already been published in [103].

6.1 Geant4

Geant4 is a toolkit to simulate the passage of charged particles and electromagnetic radiation through matter which was developed at CERN [100, 101]. It is a free software package written in C++ which provides a series of classes that cover all the aspects needed for the simulations:

- the definition of the geometry of the system
- a database with the properties of pure materials and all the compounds defined by the National Institute of Standards and Technology (NIST)
- the database with the cross sections of the physics processes
- the generation of the primary events and the tracking of particles through materials and electromagnetic fields
- the storage of events and tracks and a graphical user interface for the visualization of the trajectories

Although it was originally developed for high energy, nuclear and accelerator physics, the last versions of Geant4 with the standard low energy electromagnetic model give good results also for positrons with energies down to 1 keV [104].

To check the validity of the Geant4 toolkit in the energy range of interest, the total backscattering probability of gold was simulated with different versions of Geant4 in the range from 1 to 30 keV. The results are shown in figure 6.1 for Geant4 release 9.4 and release 9.5 in comparison with the experimental and calculated data of Mäkinen *et al.* [97]. The agreement of the Geant4 release 9.4 results is very good, especially in the energy range from 15 keV to 30 keV, for both energy cut-off values of 20 and 50 eV. At energies lower than 8 keV, even with an energy cut-off value of 20 eV, the total backscattering probability is about 50% lower than the measured values. In Geant4 release 9.5 the low energy electromagnetic classes which describe the interactions of electrons, positrons and photons were upgraded. From this release on, the standard low energy electromagnetic classes are based on the version 2001 of the PENELOPE (PENetration and Energy LOss of Positrons and Electrons) model [105]. With this model it is possible to simulate the slowing down of positrons in matter taking into account multiple scattering, ionization and bremsstrahlung from 1 GeV down to hundred of eV. For unknown reasons, with this release the total backscattering probability is overestimated by about (5-8)% from 30 to about 6 keV.

However, due to technical issues with release 9.4, it was decided to perform the simulations with Geant4 release 9.5 and the PENELOPE low energy electromagnetic classes. The influence of the discrepancy in the total

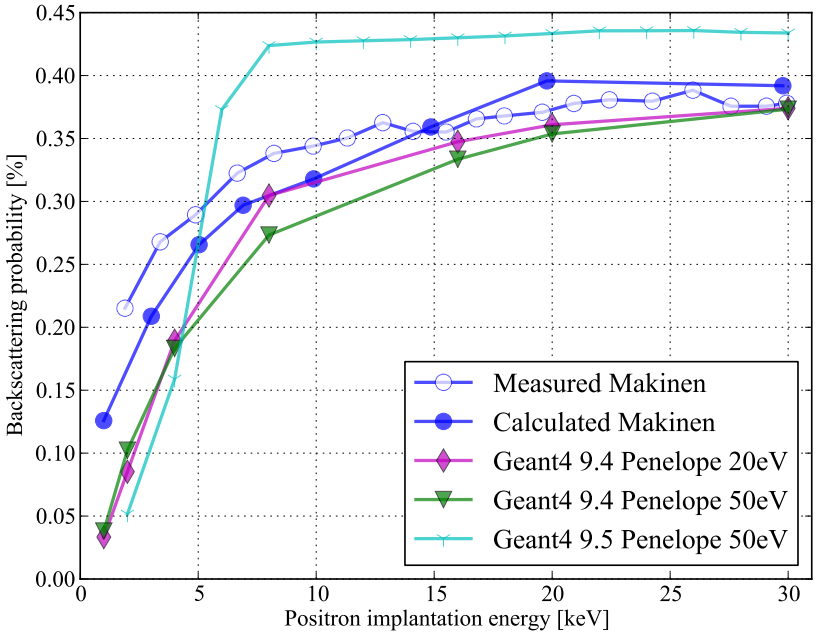

Figure 6.1: Experimentally measured and simulated positron backscattering probability for a gold target as a function of the implantation energy. The data of Mäkinen are from ref. [97].

backscattering probability on the simulated spectra is discussed in section 6.4.

6.2 Electric and magnetic fields calculation with COMSOL Multiphysics ©

As Geant4 allows only the definition of homogeneous electric and magnetic fields, they had to be calculated separately in order to reproduce accurately the real system. For this purpose COMSOL Multiphysics © [102] was used. This program is a solver and simulation software for many physics and engineering problems based on the finite element method (FEM). After modeling the geometry of the system and defining its boundary conditions and the physics, a mesh is created and the field equations are numerically solved.

The target chamber of PLEPS with the Faraday cage (described in section 3.2.3) had to be modeled to study the effect of positrons that are backscattered from the sample, travel through the target chamber and annihilate on its walls. To obtain the magnetic field a two dimensional simulation was sufficient, since the system is rotationally symmetric, and periodic boundary conditions were used. In figure 6.2 the section of the target chamber paral-

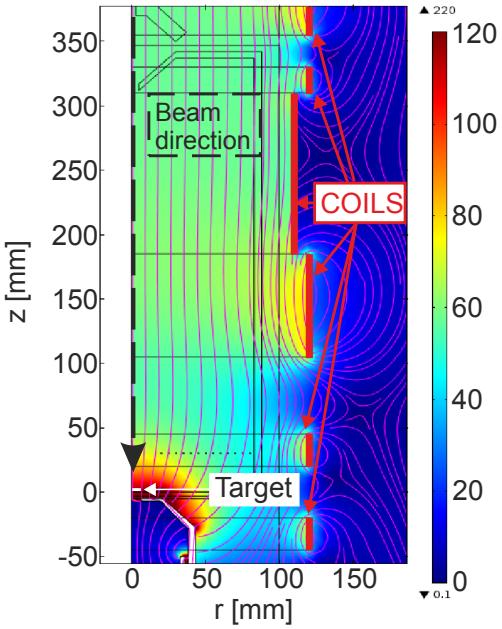

Figure 6.2: Model of the target chamber used in the calculation of the magnetic flux density. The magnetic flux density is plotted as surface and streamline-plots.

lel to the beam direction and the coils that generate the magnetic field are shown. The magnetic flux density is plotted as surface- and streamline-plots as a function of the position. The magnetic field is homogeneous along the

beam path, except for the last 30 mm where the field increases due to the presence of the mu-metal shielding of the detector, and it agrees with the measured values.

For the electric fields the rotational symmetry is broken and, therefore, a three dimensional simulation of the Faraday cage was necessary. The model of the target chamber used in the COMSOL simulations is shown in figure 6.3

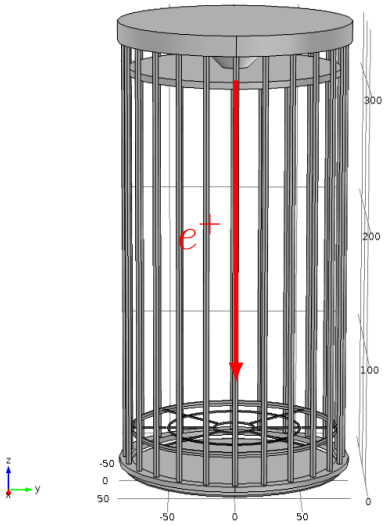

Figure 6.3: Model of the Faraday cage used in the calculation of the electric fields using COMSOL Multiphysics.

The only differences from the real target chamber, shown in figure 6.4, are:

1. The complicated fan-like structure of tungsten blades on the top of the Faraday cage was substituted by a simple plate in the model of both the COMSOL.
2. The thin wire structure (tungsten wire with diameter of $\sim 20 \mu$m) placed about 3 cm above the target to close the Faraday cage was approximated by a simpler structure in the calculation of the electric fields as can be seen by comparing figure 6.3 with figure 6.4.

Figure 6.5 shows the electric potential as contour-plot and the electric field as arrow field in a section of the target chamber parallel to the beam direction.

The electric and magnetic fields were then saved as text files and imported in the Geant4 program.

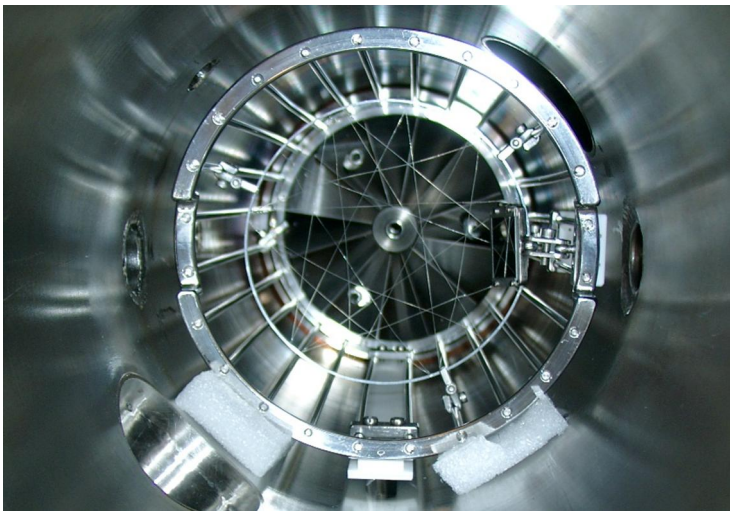

Figure 6.4: The Faraday cage seen from the target position. The fan-like tungsten structure and the thin wired structure at the bottom of the Faraday cage are visible.

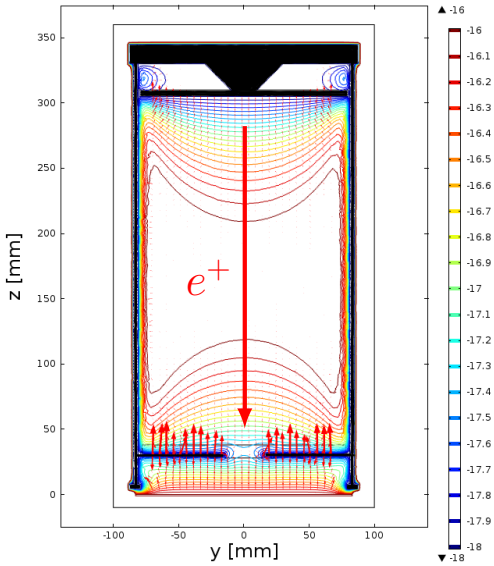

Figure 6.5: Electric potential and field in the target chamber of PLEPS as calculated by COMSOL Multiphysics © for a positron implantation energy of 16 keV. The cross section parallel to the beam direction (z) is shown.

6.3 Simulation details and results

The simulations were performed with Geant4 version 9.5 patch 01 and the PENELOPE (PENetration and Energy LOss of Positrons and Electrons and photons) low-energy electromagnetic model, including ionization, bremsstrahlung and multiple scattering. A cut-off energy threshold of 50 eV was set.

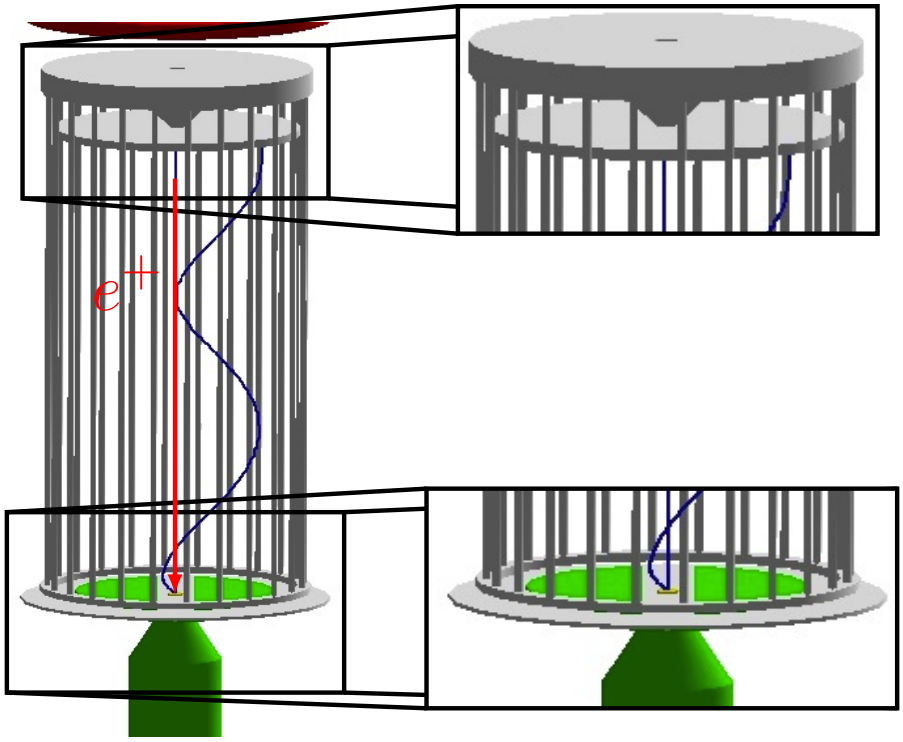

Figure 6.6: Model of the target chamber used in the Geant4 simulations and trajectory of a backscattered positron. On the right hand side the bottom and the top of the target chamber are enlarged.

The structure of the Faraday cage and also the detector with the whole tungsten shielding (in green) were modeled according to the real setup. The only differences concern the top of the target chamber, approximated with a simple plate as in the case of the COMSOL simulations, and the thin wire structure that closes the Faraday cage. As the fraction of the area shadowed by the thin wire structure with respect to the cross section of the Faraday cage is $< 0.6\,\%$, this structure was neglected in the Geant4 simulations.

The direction of the incoming beam is illustrate by the red arrow in figure 6.6. A simulated trajectory of a positron backscattered from the target and

annihilating on the top of the Faraday cage (blue line) is also shown.

For each simulation 10^8 positrons were implanted into the sample to obtain approximately the same number of events in the measured and in the simulated spectra. A gold target was chosen since it represents the "worst case scenario" because of a backscattering coefficient as high as $\sim 35\,\%$ for positron implantation energies $> 10\,\mathrm{keV}$ (see figure 6.1). The annihilation position and the time between the implantation of the positron and the arrival of the gamma quantum in the detector were saved. To register only events that are actually seen by the detector the 511 keV annihilation quanta that deposited less than 300 keV were rejected like in the real experiment. To highlight only the satellite structures due to the backscattered positrons, from both, the simulated and the measured spectra, the constant random background has been subtracted.

In figures 6.7, 6.8 and 6.9 the results of the simulations with a gold target at different positron implantation energies are compared to the experimental measurements. Despite the discrepancy in the total backscattering probability shown in figure 6.1, the overall agreement of the simulated background with the measured spectra is quite good at every implantation energy. In particular, the position of the minima in the simulated background are in perfect agreement with the experimental measurement.

The satellite structures have a strong energy dependence and three energy ranges can be identified depending on the shape of the structures: a high energy range from 10 keV to about 20 keV, an intermediate energy range from 4 keV to 10 keV and the low energy regime between 1 keV and 2 keV.

High energy range. As illustrated in figure 6.7, at high positron implantation energy, for example 12 keV and 16 keV in plot 6.7(a) and 6.7(b), respectively, a first sharp peak between 2 and 4 ns and a continuous structure from about 6 ns till the end of the time window are present.

Intermediate energy range. On the other hand, at energies lower than 10 keV, the situation is clearly different. For instance, in the intermediate energy range from 4 keV to 8 keV, two pronounced satellite structures appear as evidenced by the plots in figure 6.8. As an example, at 8 keV a backscattered peak is centered at about 9 ns. The second structure is centered at 16 ns and re-enters the time window from the opposite side (see Fig. 6.8(a)). The same behavior can be also seen in figure 6.8(b) for 4 keV positron implantation energy.

Low energy range. In the low energy range, only one satellite structure can be identified as can be seen in figure 6.9. The agreement is in this case very good, however this energy range is not discussed in detail, due to the lack of precision of the Geant4 toolkit at low positron implantation energies (as can be seen in figure 6.1) and due to the presence of a long component

that can possibly hide smaller structures.

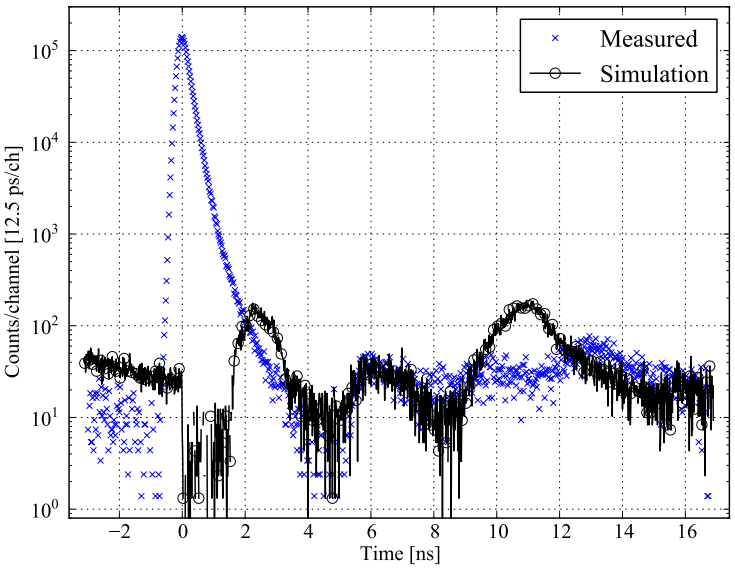

(a) 16 keV positron implantation energy

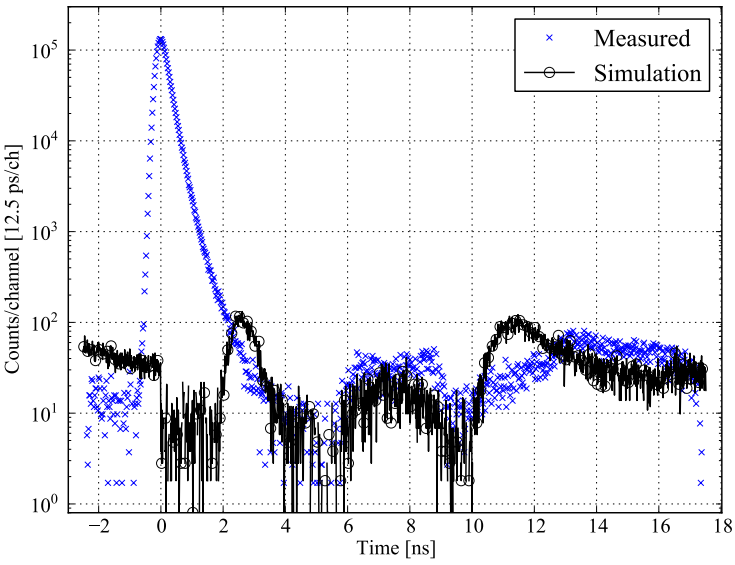

(b) 12 keV positron implantation energy

Figure 6.7: Comparison between the experimental measurement and the simulated background structure on a gold target in the high positron implantation energy range.

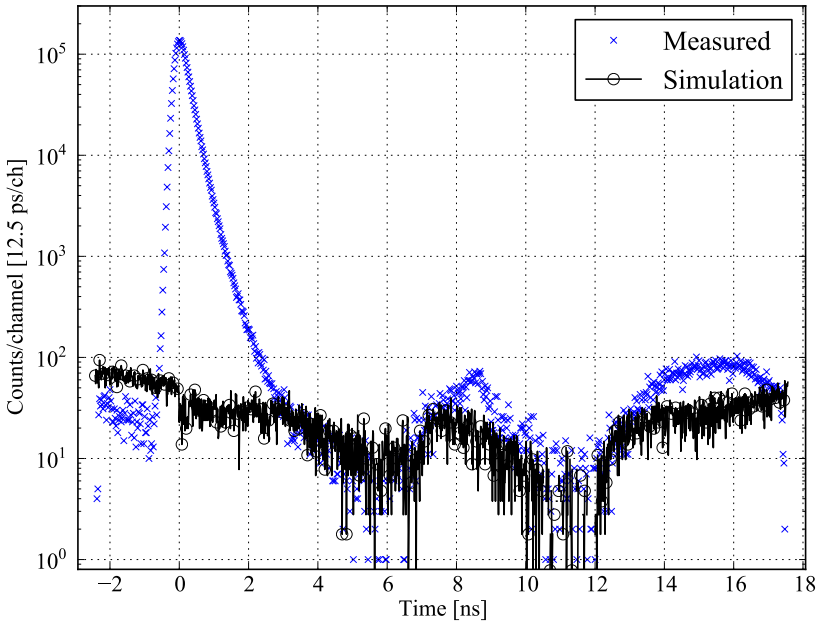

(a) 8 keV positron implantation energy

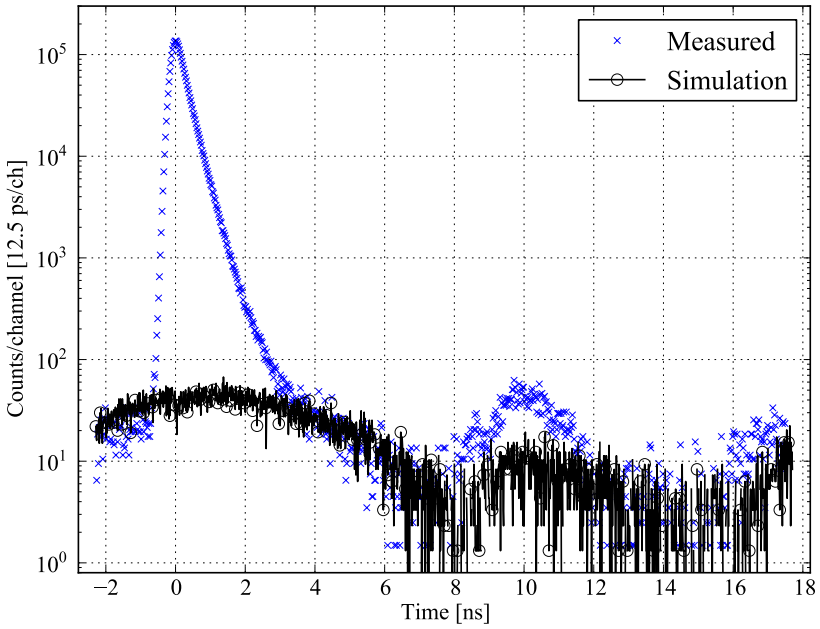

(b) 4 keV positron implantation energy

Figure 6.8: Comparison between the experimental measurement and the simulated background structure on a gold target in the intermediate positron implantation energy range.

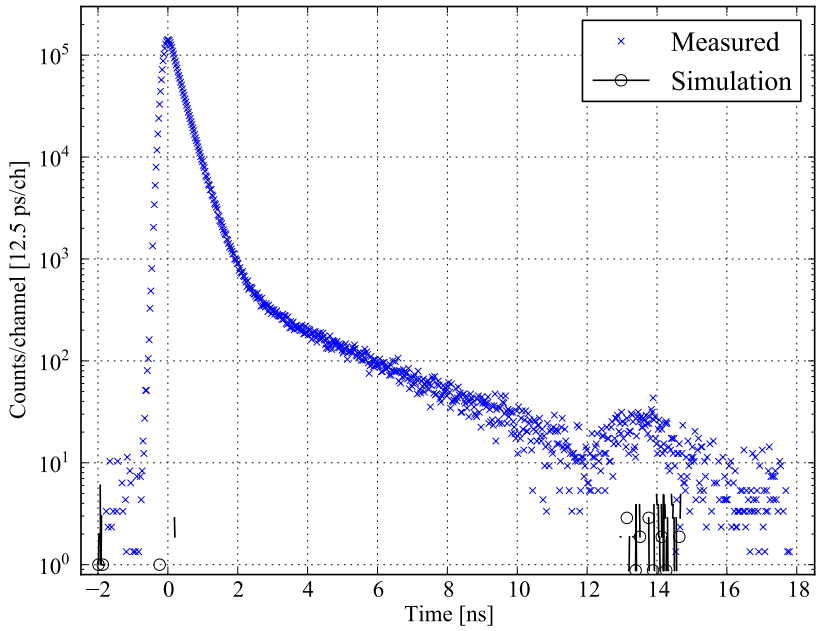

Figure 6.9: Comparison between the experimental measurement and the simulated background structure on a gold target at 1 keV positron implantation energy (low energy range).

Origin of the background structures

To better understand the origin of the single structures, the results of the simulations were analyzed by looking at the provenience of the annihilation gamma quanta. In particular, the target chamber was divided into four parts (target, Faraday cage, top and bottom if the target chamber) and the satellite structures were plotted depending on their provenience according to the colors in figure 6.10.

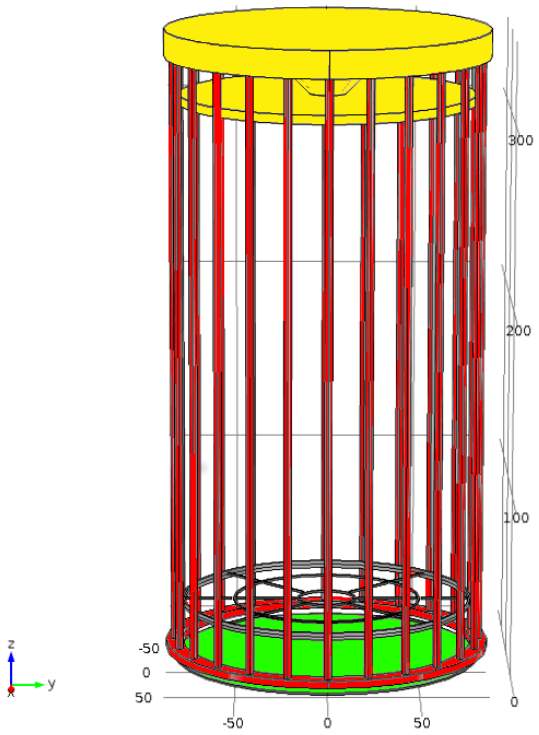

Figure 6.10: Model of the target chamber of PLEPS as in the COMSOL simulation. The colors of the different parts are the same as in the analysis of the results of the simulations: Faraday cage in red, target in black, top and bottom of the target chamber in yellow and green, respectively.

Figure 6.11 shows the results obtained for the simulation at 16 keV positron implantation energy in gold analyzed with the method described above. This plot shows that the satellite structure centered at about 6 ns is mainly due to positrons that, after being backscattered from the target, annihilate on the top of the target chamber (yellow). On the other hand, the structure that extends from 10 ns till the end of the time window and enters from the other side, is caused by positrons ending their trajectories on the bottom of

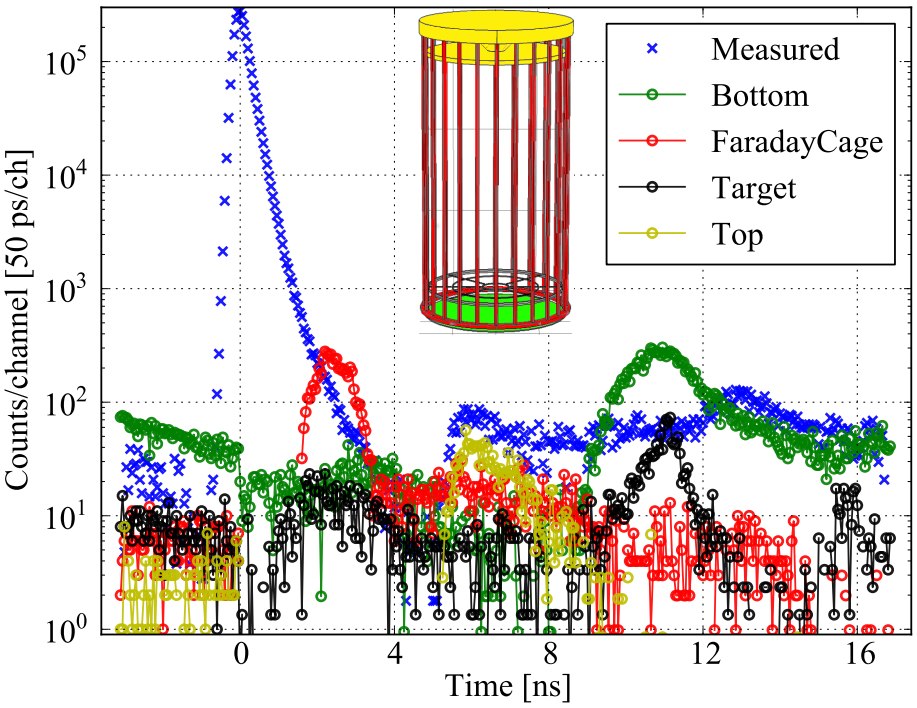

Figure 6.11: Comparison between the experimental measurement and the simulated background structure on a gold target at 16 keV positron implantation energy.

the target chamber; after a first scattering off the target, these positrons can reach either the top or the bars of the Faraday cage and are backscattered again towards the target. Some of these positrons are guided and implanted on the sample (black line in the figure), whereas the majority of them annihilate on the bottom of the target chamber (green). The simulations show also a structure centered at 2.5 ns coming from annihilations on the bars of the Faraday cage (red) for both 12 keV and 16 keV positron implantation energy. The measured spectrum shows a much smaller satellite structure in this position. However, since after about 3 ns the longer lifetime is not yet totally decayed, this structure is probably hidden under the lifetime peak. The rather poor agreement of this part of the simulated spectrum could possibly be attributed to deficiencies of the multiple scattering model used by Geant4 in the considered energy range.

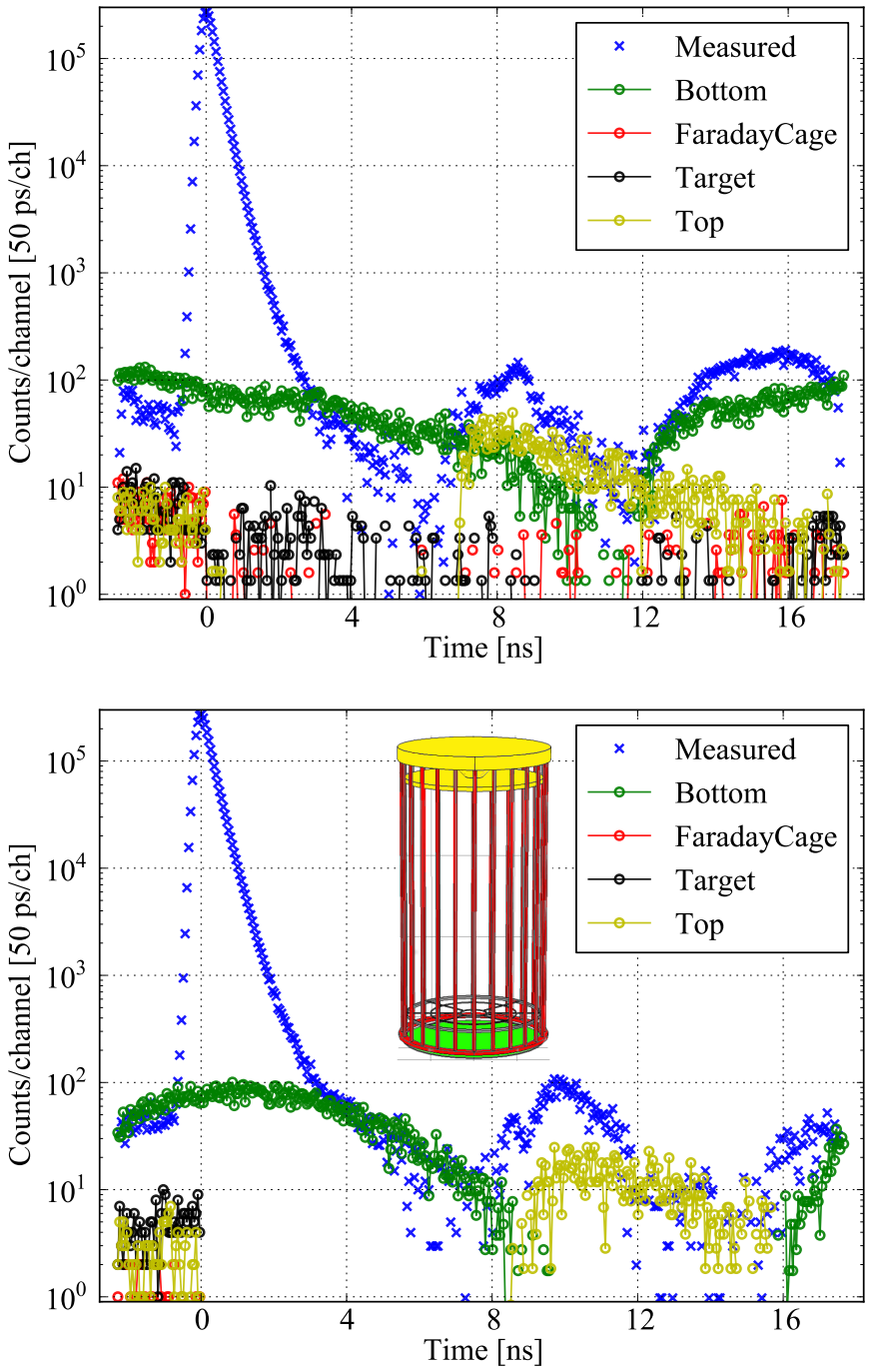

Figure 6.12: Comparison between the experimental measurement and the simulated background structure on a gold target at 8 keV and 4 keV positron implantation energy (upper and lower plot, respectively).

The results obtained in the intermediate energy range are illustrated in figure 6.12 for 8 keV and for 4 keV positron implantation energy. In this energy range the first peak (red) at 2.5 ns disappears, since the backscattered positrons do not have enough energy to reach the bars of the Faraday cage close to the target. As in the high energy case, the structures centered at (8 – 10) ns and at about (15 – 18) ns are due to annihilations coming from the top and the bottom of the target chamber, respectively. The second structure (centered at 15 ns for 8 keV and about 18 ns for 4 keV) is folded over, re-enters the time window and is therefore partially hidden under the lifetime peak. This effect is especially evident at 4 keV and is highlighted by the green curve in plot 6.12 (lower plot), which is positioned almost exactly under the lifetime peak.

Countermeasures

The results of the simulations have evidenced the following countermeasures to suppress the satellite peaks or at least to reduce the problems induced by their presence in the lifetime spectrum with the present setup of PLEPS:

1. **time window extension:** to move part of the satellite structures in less important region of the lifetime spectrum
2. **using a low Z material on top of target chamber:** to reduce the amount of positrons that are backscattered from the top of the target chamber and re-accelerated towards the sample region
3. **measurement in coincidence:** to register only the events coming from annihilations in the target

These three countermeasures are discussed in detail in the next sections.

6.3.1 Time window extension

The first countermeasure studied is the extension of the time window, which will be discussed also in section 7.2. This improvement not only plays a crucial role in the data analysis of samples containing long lifetime components, but it also improves the overall quality of all measurements, by moving part of the satellite structure in less important region of the lifetime spectrum. Figures 6.13 and 6.14 illustrate the comparison between the experimental measurement and the result of the simulation on a gold target at 16 keV and 4 keV, respectively. The upper panel of each plot shows the measurement done with the standard 20 ns time window, while in the lower panel the additional chopper plate was used and the time window was extended to 40 ns.

High energy range. At high positron implantation energy (see upper plot in figure 6.13) the satellite structures caused by annihilations on the Faraday cage and on the top of the target chamber (red and yellow curves, respectively) are almost unchanged. The extension of the time window affects strongly the shape and the position of the contributions coming from the bottom of the target chamber (green for the bottom and black for the target). In particular, the black curve shows a maximum at about (2–3) ns in the upper panel, while with the 40 ns time window this structure is spread between 22 ns and 26 ns. The same effect is visible for the annihilations on the bottom of the target chamber (green curve), since the structure starting at about 11 ns decays slowly and after 35 ns shows an almost flat background. The overall effect is a decrease of the counts in the satellite structures present in the range $(-2 < t < 2)$ ns by a factor $\sim$4.

Intermediate energy range. In the intermediate energy range (figure 6.14, lower plot for the 4 keV positron implantation energy) the contribution of the top of the target chamber is also not affected by the time window extension. As in the high energy range, the structures due to positrons annihilating at the bottom of the target chamber and in the target are confined between 16 ns and 30 ns. At the end of the time window these structures are completely decayed. Contrary to the 20 ns time window, where the structure caused by annihilation at the bottom of the target chamber is hidden under the lifetime peak, in the region from -5 ns to 0 ns the background is almost flat and between 0 ns and 7 ns it shows no structures at all.

Direct comparison 20 ns and 40 ns time window A direct comparison of the measured spectra in gold with the 20 ns and 40 ns time window is shown in figures 6.15(a) and 6.15(b) for the 16 keV and 4 keV positron implantation energies, respectively. From these plots it is evident how the extension of the time window can improve the quality of the lifetime spectra. In fact for both energy ranges the satellite structures are completely decayed

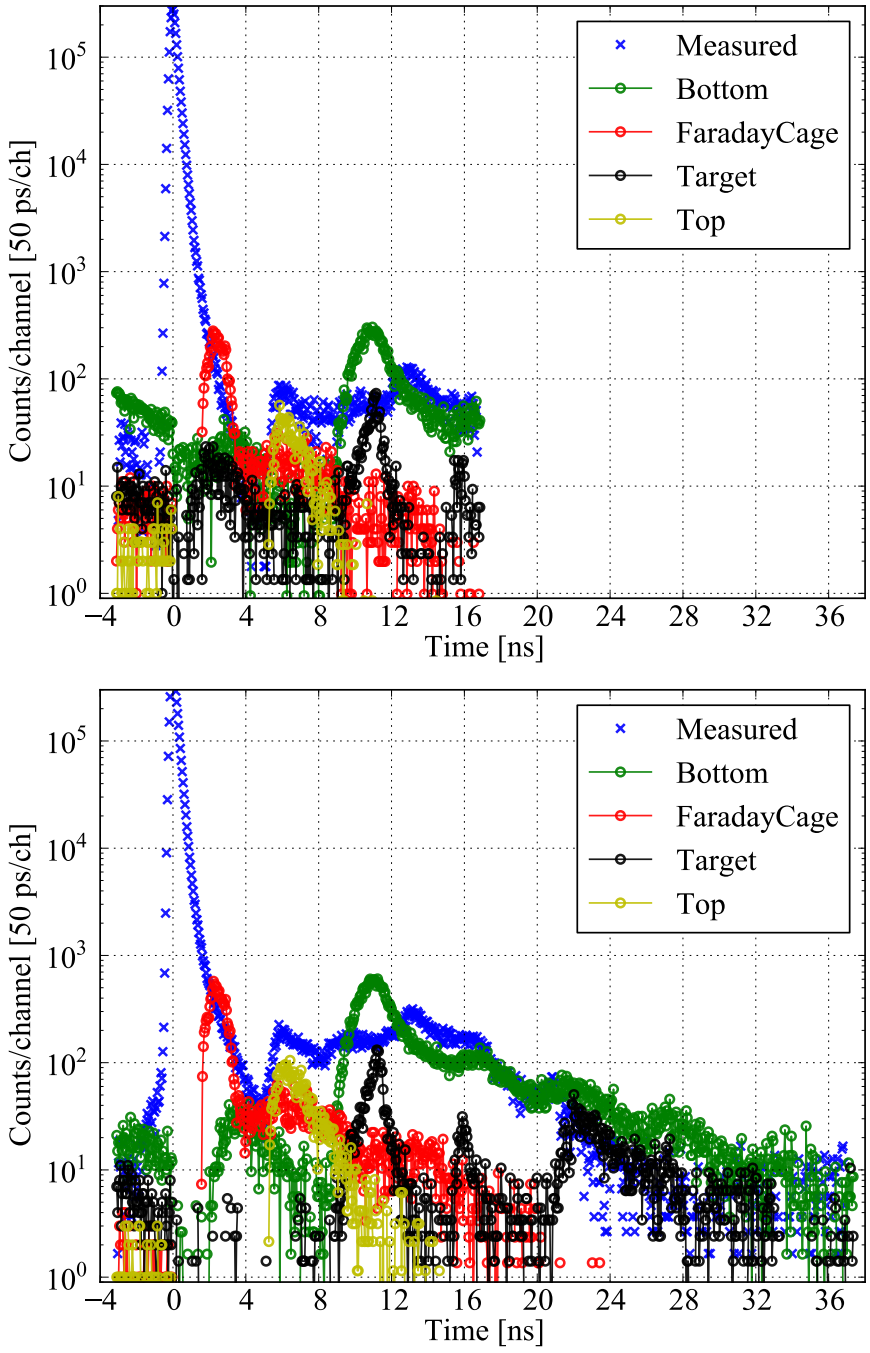

Figure 6.13: Comparison between the experimental measurement and the simulated background structure on a gold target at 16 keV positron implantation energy with a 20 ns (upper plot) and 40 ns (lower plot).

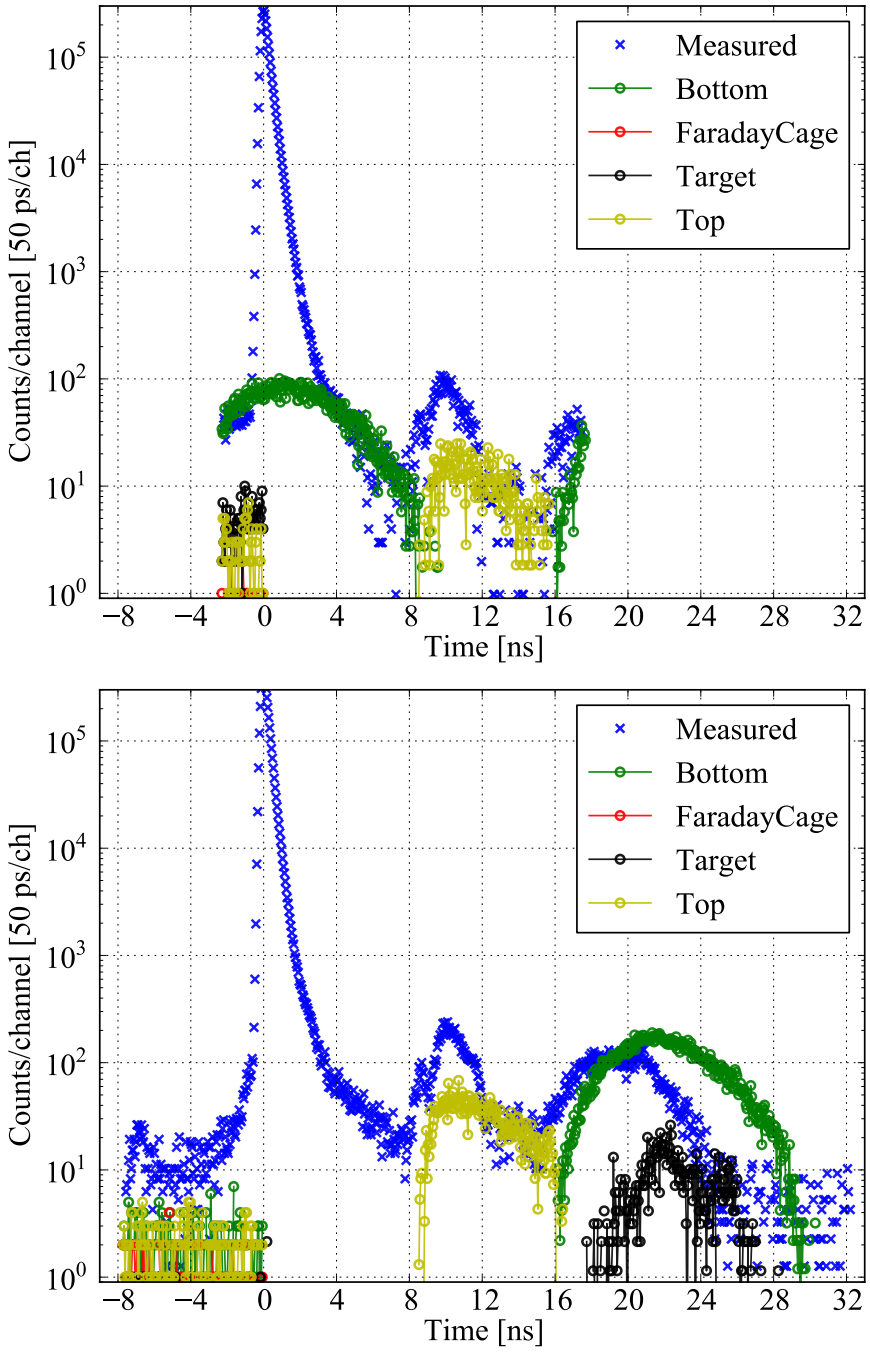

Figure 6.14: Comparison between the experimental measurement and the simulated background structure on a gold target at 4 keV positron implantation energy with a 20 ns (upper plot) and 40 ns (lower plot).

after 28 ns leaving the lifetime peak region with a flat background. Moreover, the constant background is a factor ∼4 lower with the 40 ns time window, which leads to a peak-to-background ratio 7.5 and 8.3 times higher for the 16 keV and 4 keV positron implantation energy, respectively.

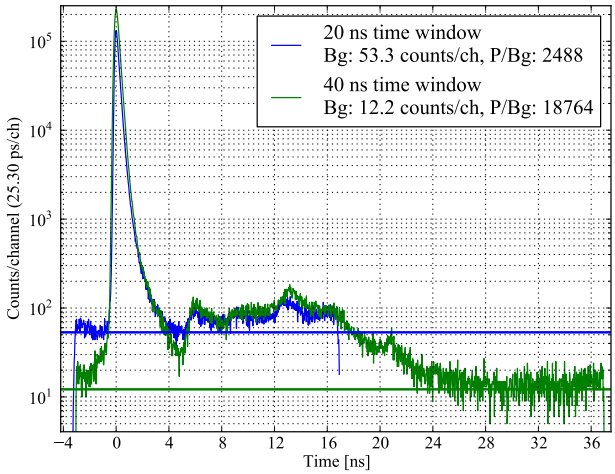

(a) 16 keV positron implantation energy

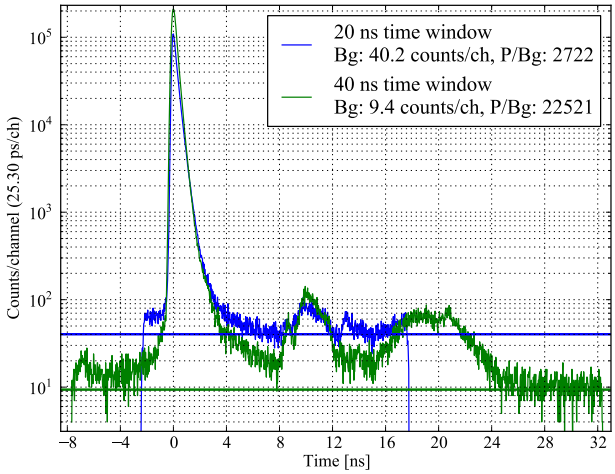

(b) 4 keV positron implantation energy

Figure 6.15: Positron lifetime spectra in gold measured with the 20 ns (blue) and 40 ns (green) time window.

6.3.2 Material at the top of the target chamber

Since most of the disturbances in the lifetime spectra come from positrons that are backscattered from the top of the target chamber and afterwards are guided toward the target position, also the influence of the material of the top of the target chamber was studied. In particular, in the current setup this part of the chamber consists of a structure of tungsten blades that should absorb the backscattered positron and, at the same time, serve as shielding for the detector from the annihilations in this region (see figure 6.4). Covering this part of the target chamber with a low Z material, *i. e.* with a lower backscattering coefficient, should decrease the number of positrons that contribute to these structures. In figure 6.16 the comparison between the measured spectrum and the results of the simulations performed with the top of the target chamber in tungsten and in kapton are shown for 16 and 4 keV positron implantation energy.

High energy range. At 16 keV (figure 6.16(a)), the satellite structures in the range from 9 ns to about 24 ns are clearly suppressed when the top of the target chamber is covered with kapton. The rest of the spectrum shows no big changes in respect to the one with tungsten.

Intermediate energy range. In the intermediate energy range, the broad structure between 16 and 28 ns is a factor 3 lower with kapton compared to the high Z material.

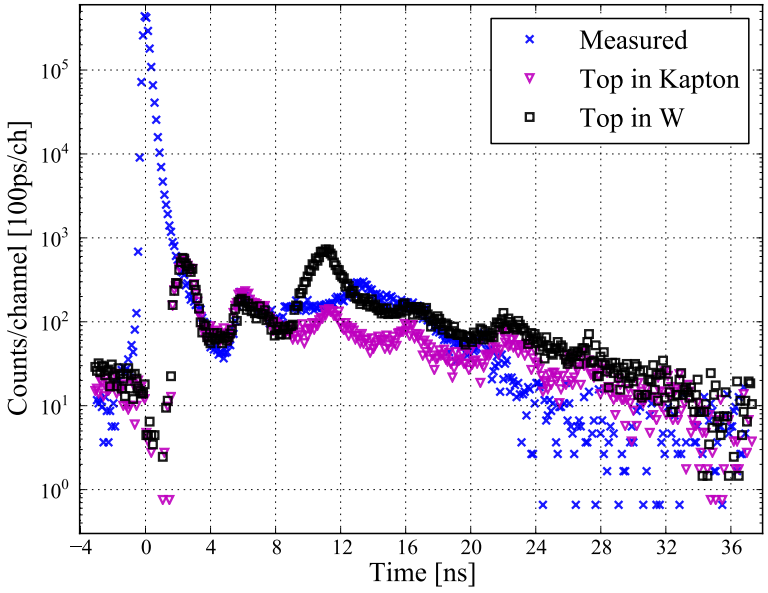

(a) 16 keV positron implantation energy

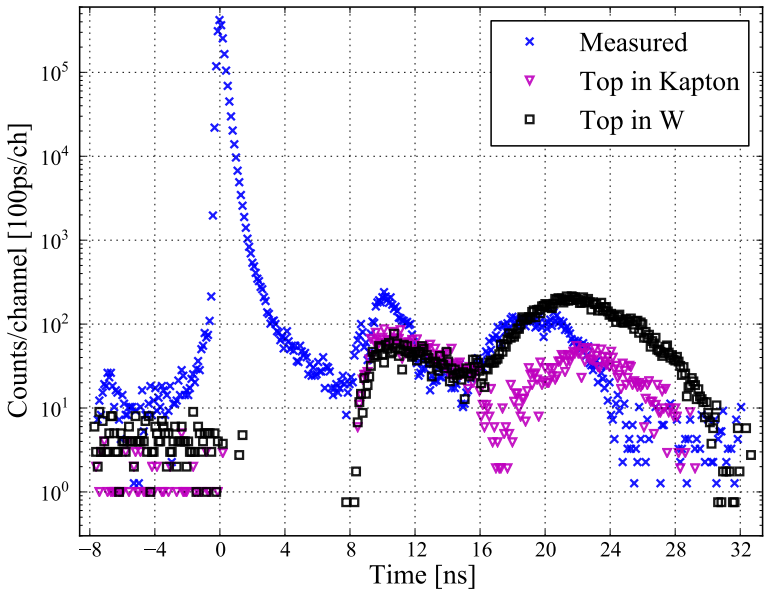

(b) 4 keV positron implantation energy

Figure 6.16: Comparison of the measured lifetime spectrum with the results of the simulations with tungsten and kapton on the top of the target chamber for 16 keV (upper plot) and 4 keV (lower plot) positron implantation energy with a 40 ns time window.

6.3.3 Measurements in coincidence

Another possibility to improve the peak-to-background ratio and to suppress the satellite structures is to use the two side ports in the target chamber to measure with two detectors in coincidence. A schematic cross section of the target chamber with the two side ports is shown in figure 6.17. The

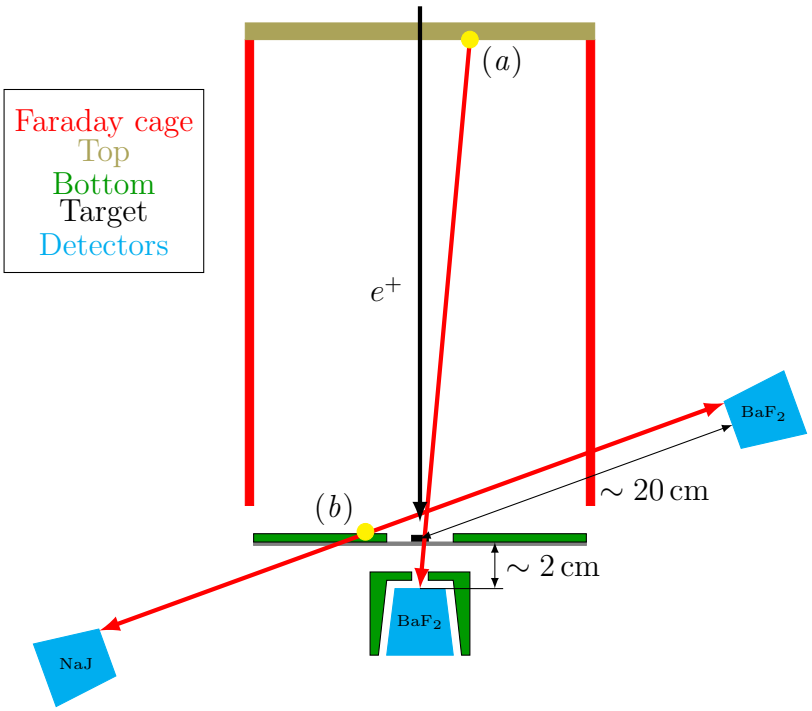

Figure 6.17: Schematic view of the target chamber, in which the different parts are colored according to the previous plots (Faraday cage in red, top in yellow, bottom in green and target in black). The detectors on the side ports and in the standard position are shown in light blue. The green parts are the tungsten shielding.

different parts of the target chamber are colored according to the previous plots, namely: red for the Faraday cage, black for the target, yellow and green for the top and bottom of the target chamber, respectively. The detectors are illustrated in light blue.

This test was performed using two photomultipliers: one coupled to a BaF_2 scintillator crystal (truncated pyramid of about 80 cm^3 volume, same scintillator used for the detector in the standard position) to have a good time resolution and the second one coupled to a NaI scintillator crystal (cylinder (5x5) cm), which has a detection efficiency about 3 times higher than the BaF_2 detector. The purpose of the NaI detector is to deliver a signal when the second annihilation gamma quantum is revealed and only in this case

the time signal measured by the BaF_2 detector is registered. Due to the low count rate (about 20 counts/s) only 250000 counts were accumulated in the coincidence measurements.

In figures 6.18, the comparison between the measurements with the detector in the standard position and the measurement with two detectors in coincidence are shown for 16 keV and 4 keV positron implantation energy (upper and lower plot, respectively).

The annihilation radiation registered with the detector in the lower port for constructive measures has to pass ∼1 cm of matter. Therefore, at 16 keV it was tested, whether placing the BaF_2 detector on either of the ports could influence the quality of the lifetime spectra. The difference was negligible and, consequently, the measurement at 4 keV was done with the BaF_2 detector on the upper port (configuration shown in figure 6.17). As can be seen by the two plots in figure 6.18, this method suppresses only part of the satellite structures. In particular, for both energies the spectra are almost background free in the range from 4 ns to 12-13 ns, but the satellite structure that starts at 12-13 ns and re-enters from the left side of the time window is still present.

The reason is, that with the coincidence measurement all the annihilations on the top of the target chamber can be filtered out, but the contribution from positrons that are backscattered again and are re-accelerated towards the region of the sample is not suppressed. These two cases are shown in figure 6.17: the gamma quanta coming from annihilations from position (a) are registered by the detector in the normal position, but are rejected in the coincidence measurement. Thus, the contribution from the top of the target chamber is suppressed in the coincidence measurement. This is not the case if the positrons are backscattered also from the top of the chamber and annihilate on the bottom of it. In fact, if the positrons annihilate close to the sample as in case (b), not only the detector in the standard position, but also the two detectors in coincidence can register these events, giving the satellite structure that starts at about 12 ns and re-enters from the left side of the time window.

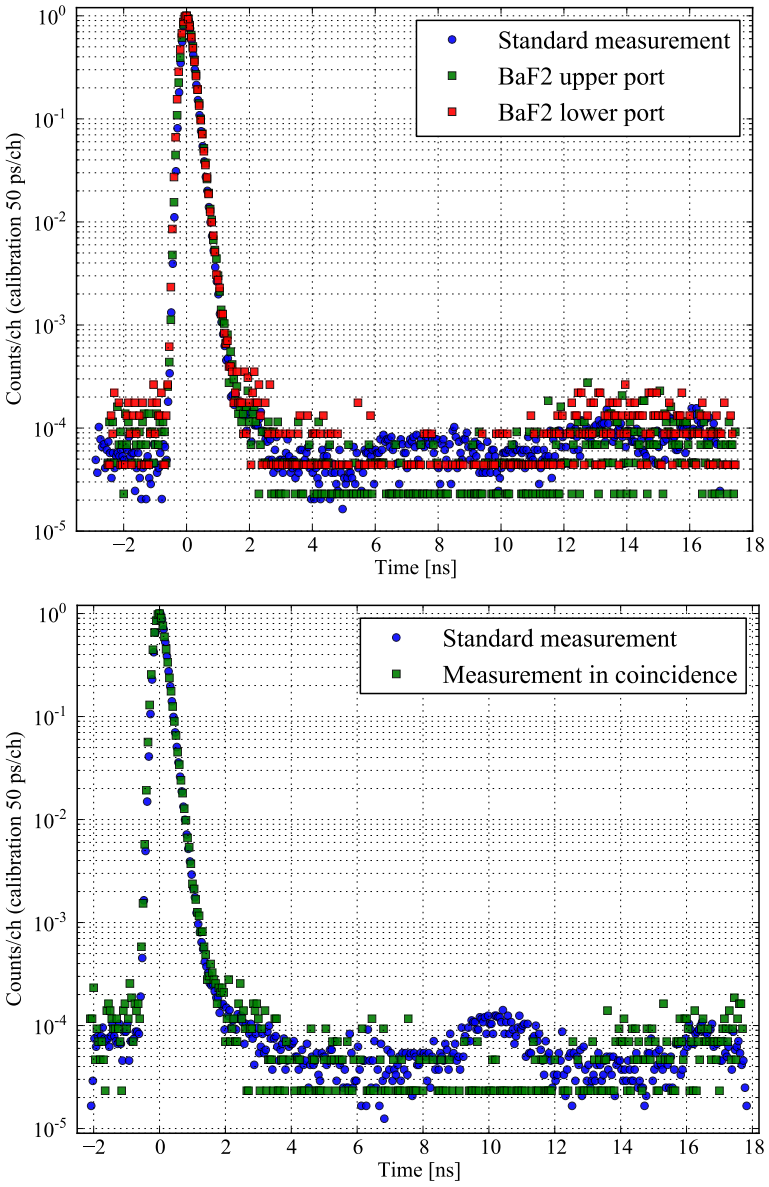

Figure 6.18: Comparison of the measured lifetime spectrum with the detector in the standard position and in coincidence for 16 keV (upper plot) and 4 keV (lower plot) positron implantation energy. All spectra were rebinned to highlight the background structures.

6.4 Conclusions and outlook

The simulations of the target chamber using the Geant4 toolkit allowed to identify the origin of the satellite structures present in the background of the positron lifetime spectra, that are caused by the backscattered positrons.

Although the total backscattering probability is about (5-8)% higher than the measured values found in literature, the overall agreement of the results of the simulations is very good at every positron implantation energy. In particular, the positions of the minima in the simulated background structure agree perfectly with the measured positron lifetime spectra. Thus, it was possible to understand the effect of the studied countermeasures:

- **time window extension**: part of the disturbing background structures are moved in less important regions of the lifetime spectrum and, since after 35 ns almost all structures are already decayed, the background in the lifetime peak region is free of structures. Moreover, the peak-to-background ratio is increased by at least a factor of 2. Since no loss in count rate was observed in the first test with a 25 MHz prebuncher and because of the advantages for precise measurements of long lifetimes, as shown in section 7.2, this is the best of the three studied solutions. The price to pay is a slightly worse time resolution (from ~ 250 ps to ~ 280 ps) due to a broader prebunched beam (about 4 ns instead of 2 ns as with the 50 MHz sawtooth generator).
- **different material on the top of target chamber**: if this part is replaced with a low Z material, the contribution of the annihilations from the bottom of the target chamber is lowered, since less positrons are backscattered from the top and re-accelerated towards the sample.
- **measurement in coincidence**: the satellite structures caused by annihilations on the top of the target chamber are completely suppressed. The drawback is a dramatic loss in counting rate (about a factor 400 less than in the standard configuration) and without major changes in the target station only if the intensity of the remoderated NEPOMUC beam were considerably increased, it could be used as a standard method.

Furthermore, the results of the simulations open a way for further progress in the analysis of positron lifetime spectra by the explicit subtraction of either the background of the spectra of tests specimen or even simulated background distributions. This requires comprehensive Z dependent simulations after the removal of the shortcomings of the present procedure, namely:

(a) the multiple scattering model used in the present version of Geant4 is not optimized for the positrons in the energy range considered.

(b) some parts of the target chamber had to be approximated by simpler geometries, particularly the modeling of the thin wire structure that closes the Faraday cage in COMSOL was impossible.

Furthermore, Geant4 could be used for an improvement of the target chamber or for the design of new, dedicated target stations optimized for different applications. The current target station was designed for measuring with the detector in the standard position below the target. In the limited available space, it contains a tungsten shield for the detector, a cryostat for measurements as a function of the temperature and also electrical connections to apply up to three voltages to the target. This reduces the count rate for coincidence measurements using the current side ports and also hinders to position the detectors closer to the sample without major modifications of the target station. A dedicated target station with small detectors closer to the target for low-background coincidence measurements could be designed by removing the cryostat.

Chapter 7

Technical improvements

In this chapter I will describe the modifications of the pulsing system. Section 7.1.1 and 7.1.2 show the improvements for a better time compression in the prebuncher and in the main buncher, respectively. In section 7.2 the hardware modification of the chopper and the adaption of the high frequency electronics for the extension of the time window from 20 ns to 40/80 ns are discussed.

7.1 Time resolution

7.1.1 Prebuncher

Figure 7.1 shows the prebuncher of PLEPS described in [2] and in section 3.2.2. As mentioned in sections 2.2.2 and 3.2.2, the prebuncher of PLEPS

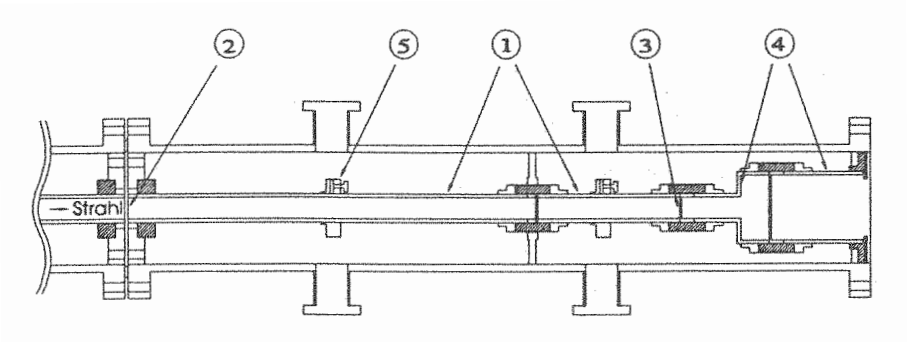

1) Drift tube
2) First buncher gap
3) Second buncher gap

Figure 7.1: Schematic view of the prebuncher (from [2]).

is operated with the sawtooth signal shown in 7.2. The rise time τ_{rise} is

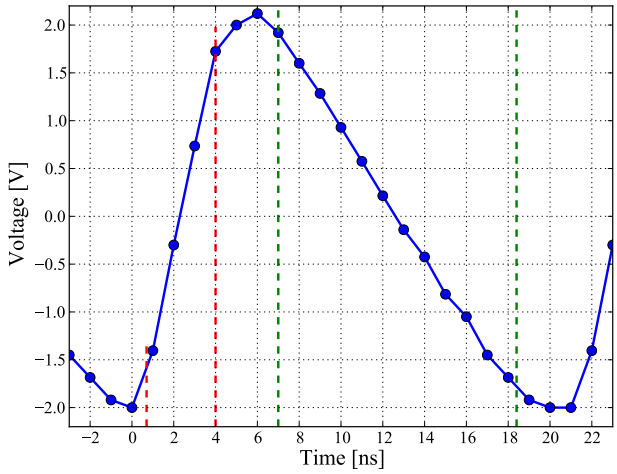

Figure 7.2: Output signal of the sawtooth generator used for the prebuncher of PLEPS. The rise time τ_{rise} and the linear part of the signal are marked by the red and green dashed lines, respectively.

highlighted by the red dashed lines and is about 3.5 ns. The effective rise time in the energy modulation τ_{eff} depends not only on τ_{rise}, but also on the transit time through the prebuncher gap $\tau_{transit} \approx D/v$, where D is the electrode diameter and v the positron velocity. In more detail, the effective rise time can be written as:

$$\tau_{eff} = \sqrt{\tau_{rise}^2 + \tau_{transit}^2} \tag{7.1}$$

and its effect is a reduction of the pulse compression efficiency of the prebuncher with respect to the ideal sawtooth signal. Eventually, a fraction $f = (\tau_{eff}/20\,ns)$ of the total intensity ends up in the background, whereas (1-f) contributes to the pulse of the prebunched beam.

Since the remoderated NEPOMUC beam has an energy E of 20 eV, the positrons travel through the prebuncher gap with a velocity of about 2.5 mm/ns. The existing prebuncher setup has an electrode diameter of 12 mm. This results in a transit time through the gap of $\tau_{transit} \approx 5$ ns, which is consistently higher than $\tau_{rise} \approx 3.5$ ns. Therefore, with an additional aperture the diameter in the first gap (see fig. 7.1) was reduced to 5 mm, resulting in a transit time $\tau_{transit} \approx 2$ ns.

7.1.2 Buncher

The time resolution of PLEPS operated with a laboratory source was about 230 ps, mainly due to the narrow longitudinal energy distribution of the incoming beam (FWHM of 0.42(4) ps [2]). As described in section 3.2, the remoderated NEPOMUC beam has a longitudinal energy distribution with a FWHM ΔE of about ~ 1 eV. As a consequence, to achieve a comparable time resolution a higher amplitude of the sine-wave signal of the buncher was required. Experimentally, it was possible to achieve a sufficient time resolution ((260 − 300) ps, see table 3.2) by lowering the constant voltage on the buncher to ~ -700 V. As already described in section 2.2.2, in a double - gap buncher a modulation occurs at both gaps if the transit time between the two gaps is a half period of the sine-wave signal, *i. e.* in our case 10 ns. A lower DC level (higher kinetic energy), reduces the transit time and thus, the reference particles do not cross the two gaps at the zero crossing of the high frequency signal. To compensate for this effect, the three electrodes of the main buncher were redesigned in order to set the DC voltage of each electrode independently. The entrance, central and exit electrodes (in the

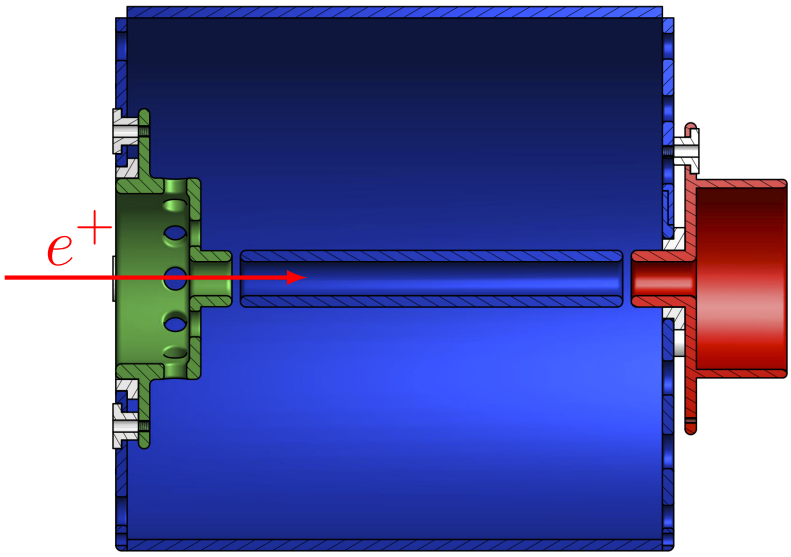

Figure 7.3: Cross section of the new buncher. The three electrodes (entrance in green, middle in blue and exit in red) are now electrically isolated allowing to apply different voltages to them. The central electrode together with a coil (not shown here) forms a 50 MHz resonator.

figure colored in green, blue and red, respectively) are now electrically iso-

lated as can be seen in figure 7.3, which shows the cross section of the new main buncher.

7.1.3 Test of the modified prebuncher and buncher

The first tests after the upgrades of the NEPOMUC source and PLEPS are encouraging. In particular, figures 7.4 show the measured positron annihilation lifetime spectra of the p-type SiC reference sample measured and 16 keV, 8 keV and 4 keV positron implantation energy. From this figure a peak-to-background ratio of about 18000:1 in the whole energy range can be inferred.

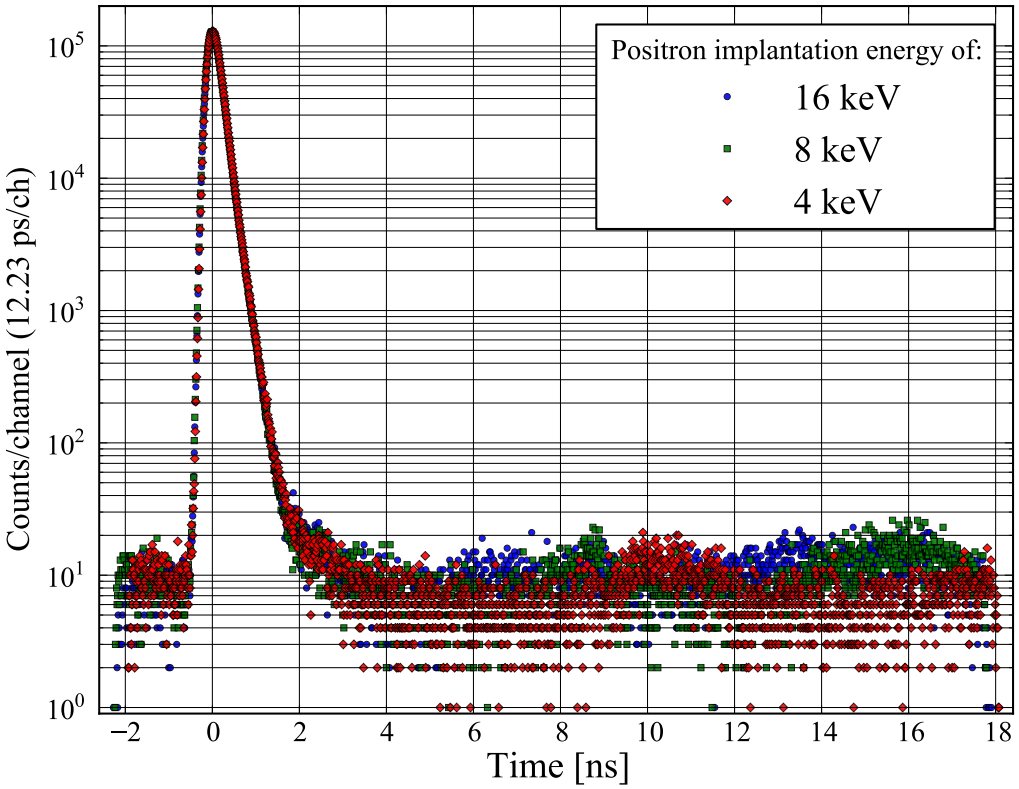

Figure 7.4: Positron annihilation lifetime spectra of the p-SiC reference sample measured at different positron implantation energies.

Already by the direct comparison of the region of the peak that is mainly determined by the instrument function (left side of the peak, see figure 7.5) a constant time resolution for the three spectra can be deduced. The deconvolution gives a time resolution of about 250 ps in the whole energy range, from 4 keV to 16 keV.

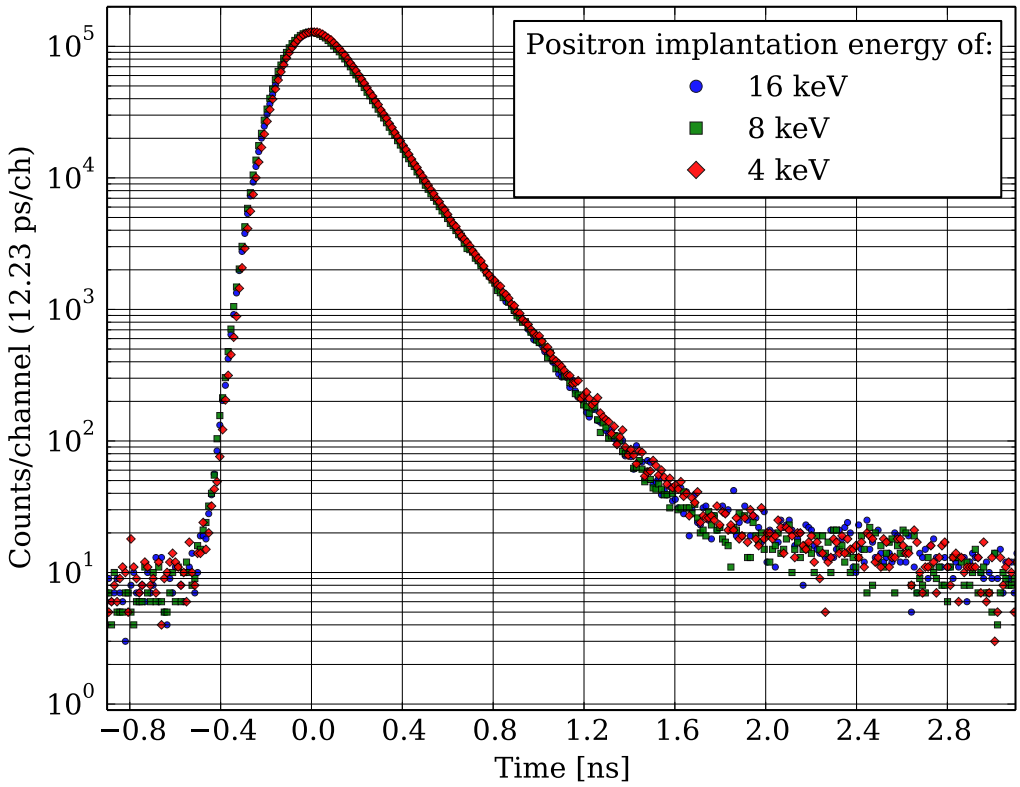

Figure 7.5: Positron annihilation lifetime spectra of the p-SiC reference sample measured at different positron implantation energies. A narrow region close to the lifetime peak is enlarged.

7.2 Extended time window

An extension of the time window by changing the master frequency of 50 MHz would imply a complete new construction of the bunching elements of the pulsing system. To overcome the limitation due to the short time window and at the same time to take advantage of the excellent performances of the existing system, a different approach was adopted. In particular, the solution described in the next section allows to extend the time window from the standard 20 ns time window to $(n \cdot 20)$ ns, $n = 2, 4, 8...$ with only minor changes in the setup and the adaption of the high frequency electronics.

7.2.1 Chopper

A schematic view of the chopper is given in figure 7.6. The new slit is highlighted in colors. When the chopper is operated with the standard 20 ns

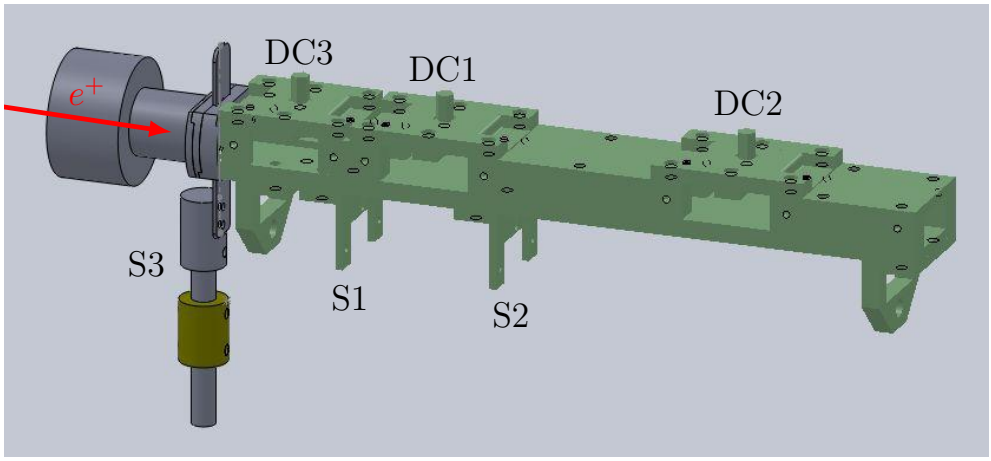

Figure 7.6: Schematic view of the chopper. Only the slits S1 and S2 and the deflection plates DC1 and DC2 are used in the standard operation mode (20 ns time window). For the time window extension the entrance slit S3 and plate DC3 are needed.

time window (given by the 50 MHz master clock), only the slits S1 and S2 are used and the high frequency signal is applied to the plates DC1 and DC2.

By applying a frequency locked signal with a lower frequency on the additional plate DC3 than on DC1 and DC2, the time window can be extended as shown schematically in figure 7.7. In particular, applying a 25 (12.5) MHz signal only every second (fourth) pulse can pass through the first slit giving a time window of 40 (80) ns.

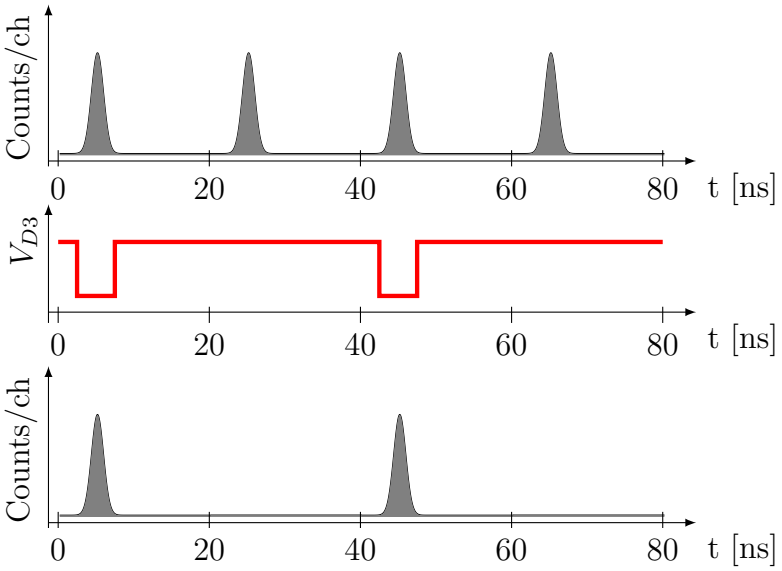

Figure 7.7: Working principle of the additional plate of the chopper. In the upper part the prebunched and chopped beam when the chopper is operated at 50 MHz is shown. If on the additional chopper plate the signal shown in the middle plot is applied, the time structure in the lower part is obtained.

7.2.2 High Freguency electronics

The operation with the additional plate needs also a modification of the high frequency electronics of the system. The HF circuit for the standard 20 ns time window is shown in black in figure 7.8 and is described in [3]. To extend the time window the signal from the master oscillator is sent to a frequency divider which than triggers the pulse module (both developed by [106]). This module gives a negative signal with an amplitude of about 20 V and a frequency of 25 MHz or 12.5 MHz depending on the settings of the divider. This signal is then applied to the additional deflection plates DC3 resulting in the time structure shown in the lower part of figure 7.7.

7.2.3 Prebuncher

In order to avoid the loss in count rate, a 25 MHz sawtooth generator (similar to the 50 MHz sawtooth generator for the standard time window) was developed by P. Sperr for the prebuncher.

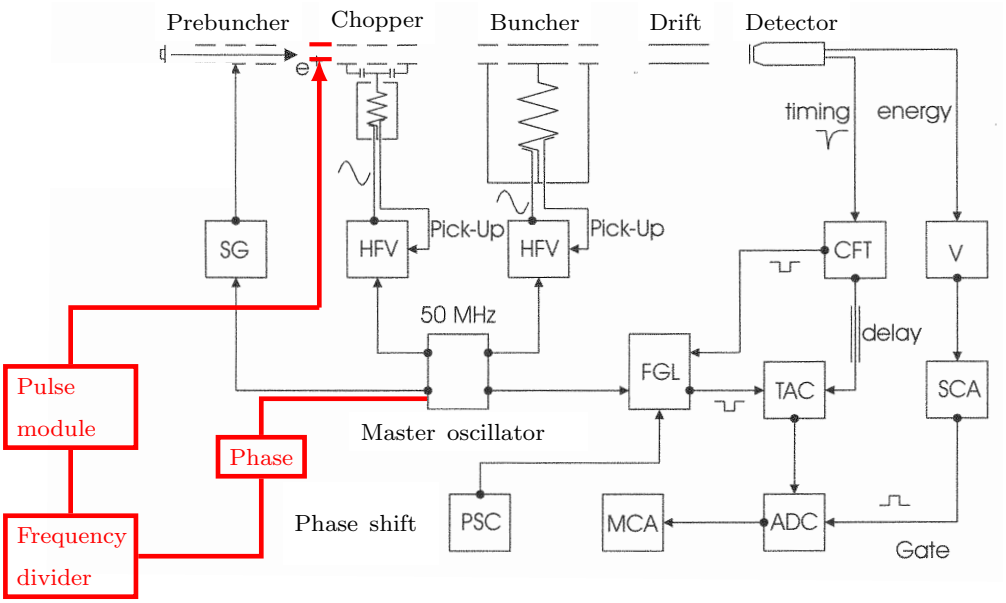

Figure 7.8: Scheme of the high frequency electronics of PLEPS (from [3]). In red the adaptions for the extension of the time window are illustrated.

7.2.4 Results of the first tests

Prebuncher: Figure 7.9 shows the spectrum of the prebunched beam. Comparing figure 7.9 with figure 3.7, it is evident that the pulse of the prebunched beam is wider (FWHM of 3.9 ns instead of 1.9 ns) when the prebuncher is operated with the new sawtooth generator. Therefore a slighlty worse time resolution has to be expected.

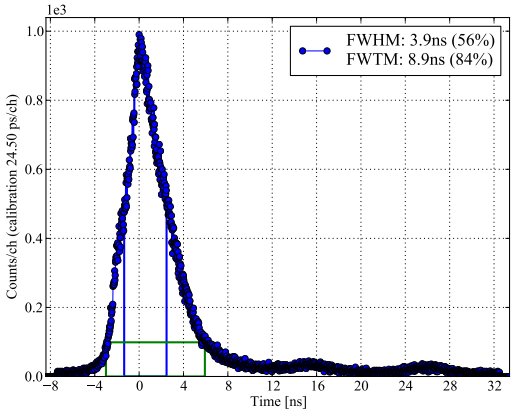

Figure 7.9: Pulse of the prebuncher operated with the 25 MHz sawtooth generator.

Entire system: The positron lifetime spectra of a p-type SiC sample at

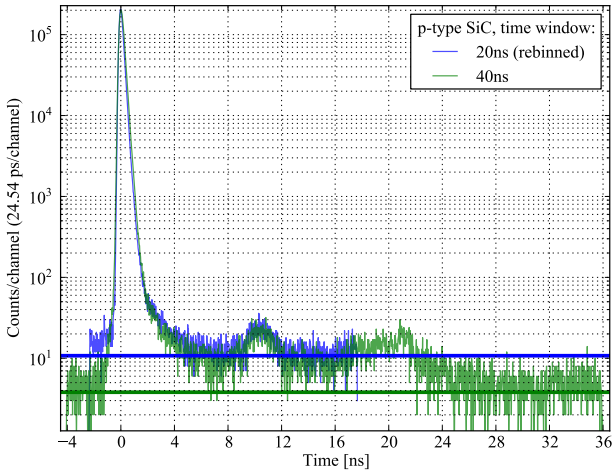

Figure 7.10: Positron lifetime spectra of p-type SiC at 4 keV positron implantation energy measured with the 20 ns and 40 ns time window.

4 keV positron implantation energy measured with the 20 ns and 40 ns time window are compared in figure 7.10. The 20 ns time window measurement

was re-binned in order to have the same channel width. No spurious peak due to the subsequent 50 MHz buncher can be observed in the green spectrum 20 ns after the lifetime peak. This means that the suppression of the unwanted pulses achieved with the modified chopper in combination with the new sawtooth generator is complete.

7.2.5 Application with long lifetimes

As pointed out in section 5, the main advantage of the extended time window is when long lifetimes are present in the lifetime spectrum. In figure 7.11 an example of lifetime spectra of two polymer systems,Teflon AF 1600 © and PIM (Polymer of Intrinsic Microporosity), is shown. This investigation resulted from a collaboration with K. Rätzke, T. Koschine and C. Ohrt (Christian-Albrecths-Universität zu Kiel, Germany). In particular, the blue

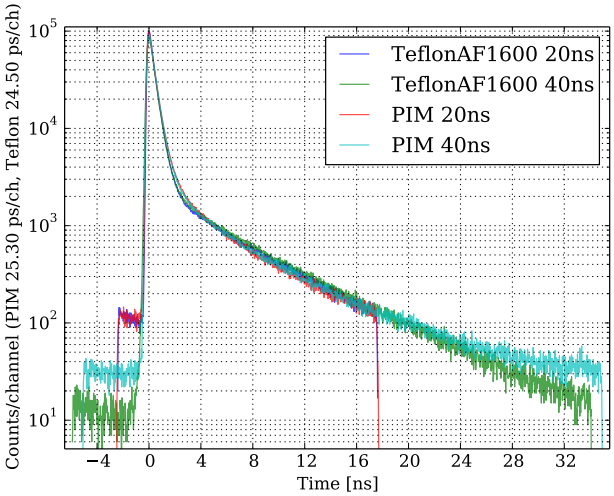

Figure 7.11: Positron lifetime spectra of PIM (Polymer with Intrinsic Microporosity) and Teflon AF 1600 © at 4 keV and 2 keV positron implantation energy, respectively, with 20 ns and 40 ns time window.

and red curves are the lifetime spectra measured with the standard time window of Teflon AF 1600 © and PIM samples measured at 2 keV and 4 keV, respectively. The energies were chosen such that all positrons were implanted in the polymer layer and also in this case the 20 ns measurements were re-binned. The same samples were measured with a time window of 40 ns and the results are shown in green and light blue for Teflon and PIM, respectively. From this plot it is evident that the high background (∼100 counts/ch) of the blue and red spectra is not the real background, but it is due to the folding

over of the long component. These measurements were analyzed by means of LT9 [92] and POSWIN [91], a modified version of POSITRONFIT [107]. Since the results from the two programs were in perfect agreement, only the ones obtained with POSWIN are summarized in table 7.1.

The background was estimated taking into account the value for the p-type SiC sample, since the average Z of these two materials is quite similar (∼17 for Teflon and 20 for SiC). The consistency of this procedure was tested by fixing the background at slightly higher values and only small changes in the lifetime components were observed.

TEFLON AF 1600 ©. First, the results on Teflon AF 1600 © will be discussed. With the 20 ns time window the fit variance is acceptable when fitting with three components ($\chi^2 = 1.176$) and little improvement is found by adding a fourth lifetime. A second lifetime component of about 440 ps with almost the same intensity is found in both cases. The four components fit shows a shorter τ_1 with a lower intensity and the long lifetime found in the three components fit, splits in this case into two parts. In particular, the weighted average of the lifetimes found with the four components fit is 5.58 ns in very good agreement with $\tau_3^{3\text{comp}} = 5.64\,ns$. This fact, together with the slightly better variance, points in direction of a four component fits, but no conclusive decision could be made at this point.

The situation is completely different when looking at the measurements performed with the 40 ns time window. In this case the fit with three components gives a poor variance and, analyzing also the fit residuals, a fourth lifetime component was clearly necessary. The four components fit shows a variance of $\chi^2 = 1.051$ and all the components are in perfect agreement with the 20 ns time window measurements. Since the background in the 40 ns time window measurement is not much higher than the one in SiC (10 counts/ch instead of 4 counts/ch), probably no component longer than $\tau_4^{4\text{comp}} = 6.63\,ns$ is present in Teflon.

Polymer of Intrinsic Microporosity. The results of the analysis of the PIM measurements are quite different from the situation in Teflon. In this case for both time window configurations the variance of the three components fit is very poor, indicating that an additional component is necessary. With a four components fit the variance decreases to $\chi^2_{20ns} = 1.041$ and $\chi^2_{40ns} = 1.089$ for the standard and for the extended time window, respectively, and therefore only this case will be discussed. A short lifetime component of about 76 ps and 216 ps is found for the 20 ns and 40 ns time window, respectively. This discrepancy could be due to the worse time resolution of the configuration with the 40 ns time window, that, in combination with the time calibration of 25 ps/ch (instead of 12.5 ps/ch), does not allow to resolve such short lifetimes. The second lifetime component is about 450 ps

Sample	Bg	τ_1	τ_2	τ_3	τ_4	I_1	I_2	I_3	I_4	Variance
Teflon 20 ns	5.0	190.1(7.0)	458.3(2.6)	—	5642(17)	14.8(0.9)	66.7(0.8)	—	18.56(0.04)	1.176
Teflon 20 ns	5.0	145.8(8.9)	434.5(3.1)	2437(438)	6220(188)	9.6(0.7)	70.8(0.6)	3.3(0.8)	16.34(0.89)	1.072
Teflon 40 ns	10.1	248.4(8.0)	485.6(5.2)	—	5869(12)	25.0(1.8)	55.1(1.8)	—	19.85(0.04)	1.277
Teflon 40 ns	4.0	148.0(8.8)	428.0(2.6)	2642(163)	6628(57)	9.1(0.6)	69.4(0.5)	4.6(0.3)	16.91(0.35)	1.051
PIM 20 ns	5.0	—	306.4(3.0)	680(9)	5240(21)	—	48.6(1.0)	34.1(1.0)	17.3(0.1)	2.056
PIM 20 ns	5.0	76.4(3.7)	427.8(2.0)	1800(65)	6364(110)	9.11(0.18)	67.19(0.18)	9.97(0.19)	13.73(0.28)	1.041
PIM 40 ns	4.2	—	410.2(0.7)	2507(31)	8845(73)	—	76.67(0.08)	12.73(0.11)	10.60(0.13)	1.989
PIM 40 ns	4.2	215(12)	469(6)	3120(70)	9370(180)	14.7(1.7)	63.9(1.6)	12.19(0.22)	9.15(0.28)	1.089

Table 7.1: Results of the fitting obtained with POSWIN for the measurements on Teflon AF 1600 © and PIM with 20 ns and 40 ns time window.

with an intensity of 65 % for both configurations.

The major differences between the 20 ns and 40 ns time window measurements are in the longer components. In particular, the measurement with the standard configuration shows a lifetime of 1.8 ns with an intensity of about 10 % and a longer component of 6.4 ns with ∼14 %, similar to τ_4 in Teflon. However, by analyzing the 40 ns time window measurement in PIM and comparing it with the Teflon case, it becomes clear that this decomposition is probably not accurate. In fact, both the lifetime components and intensities obtained by the fit of the 20 ns time window are very similar to those in Teflon, but the background in the 40 ns time window is about 3 times higher in PIM (∼30 counts/ch). Furthermore, considering that the background value in gold in the same condition was about 9 counts/ch, this is a clear indication of a presence of a lifetime longer than (6-7) ns. The decomposition of the measurement with the 40 ns time window shows two long lifetimes of 3.1 ns and 9.4 ns with intensities of about 12 % and 9 %, respectively. The weighted average lifetime obtained with these two components is about 5.8 ns, similar to τ_4 obtained in the 20 ns time window measurement.

7.2.6 Conclusions extension of the time window

These measurements on polymers with the standard and the extended time windows have shown that:

a) in Teflon AF 1600 © four components can be resolved with both configurations. With the 20 ns time window both fits with three and four components were acceptable and it was therefore difficult to resolve the question. The analysis of the measurement with the 40 ns time window permitted to decide between the two possible solutions, since not only the quality of the four components fit was very good, but also no acceptable fit was obtained with three lifetime components. This example demonstrated that for the 20 ns time window measurements not only the lifetime components, but also the corresponding intensities agree very well with the extended time window, if the longest component is about 6.6 ns. Furthermore, in this case if the background is fixed to a reasonable value (in this case the value of p-type SiC was good enough), the contribution of the folding over of the longer lifetimes is small and no renormalization of the intensities is necessary.
b) for PIM a four components fit was necessary for both the 20 ns and 40 ns time window measurements. The results of the two fits do not agree, the 20 ns time window results being very similar to those of Teflon and the 40 ns ones showing two long lifetimes of about 3.1 ns and 9.4 ns.

Considering that both, the backscattering of PIM and Teflon, and the measurement conditions, were similar (almost the same measuring time and background in the SiC reference spectrum), an almost equal background value was expected if the decomposition of the 20 ns measurement were correct. Since the spectrum measured with the 40 ns time window has a much higher background than Teflon, *i. e.* 30 counts/ch instead of 10 counts/ch (see figure 7.11), in PIM a longer lifetime component is expected. For this reason, the correct decomposition is most probably the one obtained with the 40 ns time window.

An additional result of this improvement concerns the background, which is almost 3 times lower in the measurement with the extended time window ($\sim$ 11 and $\sim$ 4 for the 20 ns and 40 ns time window, respectively). Moreover, the background structure that re-enters the time windows from the left side and is partially hidden under the lifetime peak with the standard time window, is moved in a region where the spectrum is already completely decayed.

Chapter 8

Summary and outlook

Although the current version of PLEPS at the NEPOMUC source represents the most productive positron lifetime system worldwide, its performance needs urgently further improvements, because of the growing demands in materials science. Initially, with the remoderated NEPOMUC beam count rates up to $10^4\,\mathrm{s}^{-1}$ were achieved, resulting in high quality positron lifetime spectra with peak-to-background ratios up to $3 \cdot 10^4$ in short measuring time (about 10 min with $\sim 4 \cdot 10^6$ counts per spectrum). The high count rate allowed to measure about 200 depth profiles in about 100 days of operation in a wide range of materials and for very different applications.

This was studied in three examples from different fields of current material science. Two investigations conducted with PLEPS prior the upgrade were discussed: a) defect characterization of strontium titanate thin layers deposited with Pulsed Laser Deposited (PLD) and strontium titanate crystals and b) void size determination in permanently densified silica glasses. In particular, the strontium titanate investigations allowed to identify the the A- and B-vacancy site ($V_{Ti} = 181\,\mathrm{ps}$ and $V_{Sr} \sim 280\,\mathrm{ps}$, respectively) in the PLD deposited thin layers, and to determine the ratio of their specific trapping rates $\mu_{V_{\mathrm{Ti}}}/\mu_{V_{\mathrm{Sr}}} \approx 3.6$. The analysis of the STO bulk crystals demonstrated the potential and the power of PLEPS for applications in complex materials. In particular, from lifetime measurements with PLEPS resulted that in commercially available STO crystals *a)* titanium vacancies are present with a concentration of (1.26 ± 0.16) ppm and *b)* upon annealing in the same conditions as in the PLD procedure these defects are still present and a layer of titanium-oxygen divacancies with a thickness of about 400 nm was introduced. These results of the PLEPS measurements led to a reevaluation of the Doppler broadening measurements and shed a new light on the unexpected results by Gentils *et al.* [87].

The second study on permanently densified silica glasses in combination with XRD measurements allowed to understand the change of the Medium Range Order upon densification. It was demonstrated that the average void radius obtained with the positron lifetime results permits to predict the shift of the first sharp diffraction peak of the static structure factor $S(Q)$ as a function of the density.

The measurements at NEPOMUC before the upgrade evidenced the limits of PLEPS. Measures for improvement had to be studied mainly in parallel to the normal user operation. At first, the background was simulated in order to understand the provenience of the satellite structures caused by backscattered positrons. The simulations were performed using the Geant4 toolkit in combination with COMSOL Multiphysics. Although the total backscattering probability simulated with the release 9.5 of Geant4 is overestimated compared to the experimental values, a rather good agreement between the simulations and the measured spectra was observed. In particular, since the minima of the simulated and measured backgrounds agreed, regions with only random background could be identified. As a consequence: *a)* some possible countermeasures to reduce or even suppress the structured background could be envisaged and *b)* the current partial treatment of background in the analysis software POSWIN is justified. If in the new version of Geant4 (release 10) a better model for the multiple scattering will be implemented, in the near future it should be even possible to quantitatively model the background in the spectra and subtract it from the measured positron lifetime spectra. This could lead to totally background - free spectra or at least drastically reduce the influence of the satellite structures on the fitted positron lifetimes and intensities. These results have demonstrated that Geant4 can be used in the near future also in the developing of new, dedicated target stations, *e. g.* a target station for coincidence measurements with two small detectors in opposing position close to the sample to maximize the count rate at low background.

During the shutdown period of NEPOMUC it was also necessary to dismantle PLEPS and in this occasion some of the hardware improvements in the pulsing system derived from the aforementioned investigations could be accomplished. Since the remoderated NEPOMUC beam has a longitudinal energy distribution with a FWHM about 2 times higher than with the laboratory source, before the upgrade it was not possible to achieve the same time resolution (best value at NEPOMUC was about 260 ps compared to 230 ps with the laboratory source). To compensate for the broader energy distribution and achieve a better time compression: *a)* A new aperture was mounted at the first buncher gap of the prebuncher to increase the effective

range of the accelerating field. *b)* The three electrodes of the main buncher were separated and electrically isolated, to improve the time compression of the buncher. Already in the first tests a time resolution of about 250 ps for positron implantation energies from 18 keV down to 4 keV was achieved.

The time window extension was successfully tested in a third study with Teflon AF© and PIM. This investigation clearly demonstrated that for samples containing only one, long lifetime, as in the case of Teflon AF, it is possible to use the 20 ns time window if the background is kept fixed to a reasonable value in the analysis of the data. In the case of PIM the measurement with the 40 ns time window showed the presence of two different long lifetimes of about 3 and 10 ns that could not be resolved using the 20 ns time window. The time window extension permits not only to better analyze the lifetime spectra of samples containing long lifetimes, but it is also useful for shifting some of the satellite structures due to the backscattered positrons in regions were they do no harm. The time resolution was about (270-280) ps at 4 keV positron implantation energy. Considering that no loss in count rate was observed, the better peak-to-background ratio and the advantage of having an almost structure - free background in the region of the positron lifetime peak, in the near future a time window of 40 ns should be routinely employed.

It is expected that, with further, systematic optimization of the setting parameters of the pulsing system (DC and high frequency voltages of the electrodes), also with the 40 ns time window a resolution comparable to the standard time window can be achieved.

There are important corollaries for the further development of PLEPS as well. The current version of PLEPS is now at its performance limit. Further progress needs a better positron beam from NEPOMUC and/or a completely new designed PLEPS system. As far as the NEPOMUC beam is concerned, less than 1% of the positrons are currently used in PLEPS. The least expensive measure for greater improvements is thus a better remoderator stage and beam transport from NEPOMUC to PLEPS.

In a completely renewed PLEPS the deficiencies of the present version, as identified in this work, could be prevented from the beginning. Furthermore, in the present work was shown, that with current simulation software the entire behaviou of all components of PLEPS can be predicted in advance. Therefore, there is still room for positron annihilation experiments to comply with further growing demands from materials science.

Appendices

Appendix A

Standard Trapping Model (STM)

Hautojrvi and Corbel [22] developed a model that describes the positron trapping in homogeneous solids with N type of defects and based on the assumptions that:

- at time $t = 0$ all the positrons are in a delocalized bulk state
- the trapping rate is proportional to the defect concentration:

$$\kappa = \mu_D c_D$$

  where μ_D is the specific trapping rate for the defect D
- the positrons can be detrapped from the defect with a rate δ.

With this assumptions and calling n_B and n_{D_j} the probabilities that a positron annihilate from the bulk state or after being trapped in the defect D_j, respectively, one obtains the following set of kinetic equations:

$$\frac{\mathrm{d}n_B}{\mathrm{dt}} = -\left(\lambda_B + \sum_{j=1}^{N} \kappa_{D_j}\right) n_B + \sum_{j=1}^{N} \delta_{D_j} n_{D_j} \tag{A.1a}$$

$$\frac{\mathrm{d}n_{D_j}}{\mathrm{dt}} = \kappa_{D_j} n_B - \left(\lambda_{D_j} + \delta_{D_j}\right) n_{D_j} \tag{A.1b}$$

with $j = 1 \ldots N$. Using the boundary condition stated in the first assumption ($n_B(t = 0) = 1\,,\ n_{D_j}(t = 0) = 0$), the system of equation can be solved, giving the probability that a positron is alive at time t:

$$n(t) = n_B(t) + \sum_{j=1}^{N} n_{D_j} = \sum_{j=1}^{N+1} I_j e^{-\lambda_j t} \tag{A.2}$$

and the lifetime spectrum, i.e. the probability that a positron annihilates at time t, is:

$$-\frac{\mathrm{d}n(t)}{\mathrm{dt}} = \sum_{j=1}^{N+1} I_j \lambda_j e^{-\lambda_j t} \,. \tag{A.3}$$

If no detrapping occurs, the system of equation A.1 can be written as:

$$\frac{\mathrm{d}n_B}{\mathrm{dt}} = -\left(\lambda_B + \sum_{j=1}^{N} \kappa_{D_j}\right) n_B \tag{A.4a}$$

$$\frac{\mathrm{d}n_{D_j}}{\mathrm{dt}} = \kappa_{D_j} n_B - \lambda_{D_j} n_{D_j} \tag{A.4b}$$

and this system can be analytically solved. Solving Eq. A.4a with the initial condition $n_B(t=0)=1$, the probability that a positron annihilate from the bulk state $n_B(t)$ can be found:

$$n_B(t) = \exp\left[-\left(\lambda_B + \sum_{j=1}^{N} \kappa_{D_j}\right) t\right] \,. \tag{A.5}$$

From Eq. A.4b, the probability of annihilation in the defect state, with boundary condition $n_D(t=0)=0$, is:

$$n_{D_j}(t) = \frac{\kappa_{D_j}}{\lambda_B + \lambda_{D_j} + \kappa_{D_j}} \cdot \left[\exp\left[-\lambda_{D_j} t\right] - \exp\left[-\left(\lambda_B + \sum_{j=1}^{N} \kappa_{D_j}\right) t\right]\right] \,. \tag{A.6}$$

Inserting the two probabilities $n_B(t)$ and $n_D(t)$ in Eq. A.2, one obtains the solution:

$$\lambda_1 = \lambda_B + \sum_{j=1}^{N} \kappa_{D_j}, \qquad I_1 = 1 - \sum\nolimits_{j=1}^{N} I_{j+1} \tag{A.7}$$

$$\lambda_2 = \lambda_{D_1}, \qquad I_2 = \kappa_{D_1} / \left(\lambda_B - \lambda_{D_1} + \sum\nolimits_{j=1}^{N} \kappa_{D_j}\right) \tag{A.8}$$

$$\lambda_{N+1} = \lambda_{D_N}, \qquad I_{N+1} = \kappa_{D_N} / \left(\lambda_B - \lambda_{D_N} + \sum\nolimits_{j=1}^{N} \kappa_{D_j}\right) \tag{A.9}$$

One type of defect

Often only one type of defect is considered and in this simplest case the system of equations A.9 become:

$$\lambda_1 = \lambda_B + \kappa_D, \qquad I_1 = 1 - I_2 \tag{A.10}$$

$$\lambda_2 = \lambda_D, \qquad I_2 = \kappa_D / (\lambda_B - \lambda_D + \kappa_D) \tag{A.11}$$

From this set of equations, some useful relations can be found:

$$\lambda_B = \lambda_1 I_1 + \lambda_2 I_2 \tag{A.12}$$

$$\tau_1 = \frac{\tau_D - \tau_{Av}}{\tau_D - \tau_B}\tau_B \tag{A.13}$$

$$\kappa_D = \frac{I_2}{I_1}(\lambda_B - \lambda_D) = I_2(\lambda_1 - \lambda_D) = \left(\frac{\tau_{Av} - \tau_B}{\tau_D - \tau_{Av}}\right)\frac{1}{\tau_B} \tag{A.14}$$

The validity of the trapping model can be tested using eq. A.12 with the annihilation rates and intensity found by the decomposition and comparing the experimental value λ_B with the theoretical annihilation rate. If the discrepancy is bigger than 5 ps, then probably more than one trapping center is present in the sample. Also equation A.13 can be used as a test, since in this formula the only experimental value is the average lifetime, which does not depend strongly on the deconvolution. Therefore, using the experimental value for τ_{Av}, one can calculate τ_1 and compare it to the measured one.

Bibliography

[1] Schödlbauer D., *Aufbau und Inbetriebnahme einer gepulsten Positronenquelle für Lebensdauermessungen*. Ph.D. thesis, Universität der Bundeswehr München, Fakultät für Luft- und Raumfahrttechnik, Institut für Nukleare Festkörperphysik (1987).

[2] Willutzki P., *Verbesserung und Erweiterung des gepulsten Positronenstrahlsystems für temperaturabhängige Lebensdauermessungen von Positronen in Festkörpern*. Ph.D. thesis, Universität der Bundeswehr München, Fakultät für Luft- und Raumfahrttechnik, Institut für Nukleare Festkörperphysik (1994).

[3] Bauer-Kugelmann W., *Technische Weiterentwicklungen am gepulsten Positronenstrahlsystem PLEPS*. Ph.D. thesis, Universität der Bundeswehr München, Fakultät für Luft- und Raumfahrttechnik, Institut für Nukleare Festkörperphysik (2000).

[4] Suzuki R., Kobayashi Y., Mikado T., Ohgaki H., Chiwaki M., Yamazaki T. and Tomimasu T., *Japanese Journal of Applied Physics*, **30** (1991) L352.

[5] Wang B., Ma Y., Wang P., Cao X., Qin X., Zhang Z., Yu R. and Wei L., *Chinese Physics C*, **32** (2008) 156.

[6] Maekawa M. and Kawasuso A., *Nuclear Instruments and Methods in Physics Research Section B: Beam Interactions with Materials and Atoms*, **270** (2012) 23.

[7] Jungmann M., Haeberle J., Krause-Rehberg R., Anwand W., Butterling M., Wagner A., Johnson J.M. and Cowan T.E., *Journal of Physics: Conference Series*, **443** (2013) 012088.

[8] Laakso A., *Construction of a Pulsing System for Low-Energy Positrons*. Ph.D. thesis (2005).

[9] Varghese C., *Study of near surface defects using positrons and development of a pulsed positron beam system*. Ph.D. thesis (2013).

[10] Ohnishi T., Shibuya K., Yamamoto T. and Lippmaa M., *Journal of Applied Physics*, **103** (2008) 103703.

[11] Keeble D.J., Wicklein S., Dittmann R., Ravelli L., Mackie R.A. and Egger W., *Physical Review Letters*, **105** (2010) 226102.

[12] Zanatta M., Baldi G., Brusa R., Egger W., Fontana A., Gilioli E., Mariazzi S., Monaco G., Ravelli L. and Sacchetti F., *Physical Review Letters*, **112** (2014) 045501.

[13] Nieminen R. and Oliva J., *Reviews of Modern Physics*, **66** (1994) 841.

[14] Schultz P.J. and Lynn K.G., *Reviews of Modern Physics*, **60** (1988) 701.

[15] Dirac P., *Proceedings of the Royal Society of London A*, **117** (1928) 610.

[16] Dirac P., *Proceedings of the Royal Society of London A*, **126** (1930) 360.

[17] Anderson C.D., *Science*, **76** (1932) 238.

[18] Anderson C.D., *Physical Review*, **43** (1933) 491.

[19] Mohorovicic S., *Astronomische Nachrichten*, **253** (1934) 93.

[20] Deutsch M., *Physical Review*, **82** (1951) 455.

[21] Hugenschmidt C., *Positron sources and positron beams*. In *Physics with many positrons: Proceedings of the International School of Physics "Enrico Fermi" Course CLXXIV*, edited by R. Brusa, A. Dupasquier and A. jr Mills, p. 399 (IOS Press, Amsterdam, 2010).

[22] Hautojrvi P. and Corbel C., *Positron spectroscopy of defects in metals and semiconductors*. In *Positron spectroscopy of solids: Proceedings of the international school of physics "E. Fermi"*, edited by A. Dupasquier and A. jr Mills, p. 563 (IOS Press, Amsterdam, 1995).

[23] Groce D., Costello D., McGowan J.W. and Herring D., *Bulletin of the American Physical Society*, **13** (1968) 1397.

[24] Hugenschmidt C., Piochacz C., Reiner M. and Schreckenbach K., *New Journal of Physics*, **14** (2012) 055027.

[25] Hawari A.I., Gidley D.W., Moxom J., Hathaway A.G. and Mukherjee S., *Journal of Physics: Conference Series*, **262** (2011) 012024.

[26] Schut H., van Veen A., de Roode J. and Labohm F., *Materials Science Forum*.

[27] Wada K., Hyodo T., Yagishita A., Ikeda M., Ohsawa S., Shidara T., Michishio K., Tachibana T., Nagashima Y. *et al.*, *The European Physical Journal D*, **66** (2012) 1.

[28] O'Rourke B.E., Oshima N., Kinomura A., Ohdaira T. and Suzuki R., *Materials Science Forum*, **733** (2013) 285.

[29] Krause-Rehberg R., Brauer G., Jungmann M., Krille A., Rogov A. and Noack K., *Applied Surface Science*.

[30] Jackson J.D., *Classical Electrodynamics* (New York, 1999), 3^{rd} edition.

[31] Goldstein H., Poole C. and Safko J., *Classical Mechanics* (Addison Wesley, 2002), 3^{rd} edition.

[32] Whiteway F.E., *Atomic Weapons Research Establishment Report*, **0-12**.

[33] Lynch F., Lewis R., Bollinger L., Henning W. and Despe O., *Nuclear Instruments and Methods*, **159** (1979) 245 .

[34] Sperr P., Willutzki P. and Maier M., *Materials Science Forum*, **175-178** (1995) 993.

[35] Perkins A. and Carbotte J., *Physical Review B*, **1** (1970) 101.

[36] Nieminen R. and Oliva J., *Physical Review B*, **22** (1980) 2226.

[37] Kubica P. and Stewart A., *Canadian Journal of Physics*, **61** (1983) 971.

[38] Knights A.P., Overton N., Goodyear A. and Coleman P.G., *Applied Surface Science*, **85** (1995) 54.

[39] Knights A. and Coleman P., *Journal of Physics: Condensed Matter*, **7** (1995) 6477.

[40] Nieminen R., *Electronic structure and positron spectroscopy of solids and surfaces*. In *Positron spectroscopy of solids: Proceedings of the international school of physics "E. Fermi"*, edited by A. Dupasquier and A. jr Mills, p. 443 (IOS Press, Amsterdam, 1995).

[41] Egger W., *Positron sources and positron beams*. In *Physics with many positrons: Proceedings of the International School of Physics "Enrico Fermi" Course CLXXIV*, edited by R. Brusa, A. Dupasquier and A.P. jr Mills, p. 419 (IOS Press, Amsterdam, 2010).

[42] Valkealathi S. and Nieminen R., *Applied Physics A*, **35** (1984) 51.

[43] Vehanen A., Saarinen K., Hautojärvi P. and Huomo H., *Physical Review B*, **35** (1987) 4606.

[44] Algers J., Sperr P., Egger W., Kögel G. and Maurer F., *Physical Review B*, **67** (2003) 125404.

[45] Brandt W. and Paulin R., *Physical Review Letters*, **21** (1968) 193.

[46] Canter K., jr Mills A. and Berko S., *Physical Review Letters*, **33** (1974) 7.

[47] Tao S., *Journal of Chemical Physics*, **56** (1972) 5499.

[48] Eldrup M., Lightbody D. and Sherwood J., *Chemical Physics*, **63** (1981) 51.

[49] Goworek T., *Chemical Physics Letters*, **366** (2002) 184.

[50] Gidley D., Frieze W., Dull T., Yee A., Ryan E. and Ho H.M., *Physical Review B*, **60** (1999) R5157.

[51] Consolati G., *Journal of Chemical Physics*, **117** (2002) 7279.

[52] Asoka-Kumar P., Alatalo M., Gosh V., Kruseman A., Nielsen B. and Lynn K., *Physical Review Letters*, **77** (1996) 2097.

[53] van Veen A., Schut H., de Vries J., Hakvoort R.A. and Ijpma M.R., *AIP Conference Proceedings*, **218** (1991) 171.

[54] Robles J.C., Ogando E. and Plazaola F., *Journal of Physics: Condensed Matter*, **19** (2007) 176222.

[55] Störmer J., *Positronenlebensdauerspektroskopie in oberflächennahen Bereichen von Silizium- und Siliziumkarbid-Halbleiterstrukturen mit monoenergetischen Positronen*. Ph.D. thesis, Universität der Bundeswehr München, Fakultät für Luft- und Raumfahrttechnik, Institut für Nukleare Festkörperphysik (1995).

[56] Checchetto R., Bazzanella N., Kale A., Miotello A., Mariazzi S., Brusa R.S., Mengucci P., Macchi C., Somoza A. *et al.*, *Physical Review B*, **84** (2011) 054115.

[57] Kögel G., *Applied Physics A*, **63** (1996) 227.

[58] Egger W., Sperr P., Kögel G. and Dollinger G., *Physica Status Solidi C*, **4** (2007) 3969.

[59] Sperr P., Egger W., Kögel G., Dollinger G., Hugenschmidt C., Repper R. and Piochacz C., *Applied Surface Science*, **255** (2008) 35.

[60] Hugenschmidt C., Kögel G., Repper R., Schreckenbach K., Sperr P., Straer B. and Triftshäuser W., *Nuclear Instruments and Methods in Physics Research Section B: Beam Interactions with Materials and Atoms*, **221** (2004) 160.

[61] Piochacz C., *Generation of a high-brightness pulsed positron beam for the Munich scanning positron microscope*. Ph.D. thesis, Technische Universität München, Fakultät für Physik (2009).

[62] Piochacz C., Kögel G., Egger W., Hugenschmidt C., Mayer J., Schreckenbach K., Sperr P., Stadlbauer M. and Dollinger G., *Applied Surface Science*, **255** (2008) 98.

[63] Bauer-Kugelmann W., Sperr P., Kögel G. and Triftshäuser W., *Materials Science Forum*, **363-365** (2001) 529.

[64] Keeble D.J., Mackie R.A., Egger W., Löwe B., Pikart P., Hugenschmidt C. and Jackson T.J., *Physical Review B*, **81** (2010) 064102.

[65] Keeble D.J., Jalan B., Ravelli L., Egger W., Kanda G. and Stemmer S., *Applied Physics Letters*, **99** 232905.

[66] Calloni A., Ferragut R., Dupasquier A., von Känel H., Guiller A., Rutz A., Ravelli L. and Egger W., *Journal of Applied Physics*, **112** 024510.

[67] Eijt S., Leegwater H., Schut H., Anastasopol A., Egger W., Ravelli L., Hugenschmidt C. and Dam B., *Journal of Alloys and Compounds*, **509** (2011) S567 .

[68] Macchi C., Maurizio C., Checchetto R., Mariazzi S., Ravelli L., Egger W., Mengucci P., Bazzanella N., Miotello A. *et al.*, *Physical Review B*, **85** (2012) 214117.

[69] Keeble D.J., Major J.D., Ravelli L., Egger W. and Durose K., *Physical Review B*, **84** (2011) 174122.

[70] Rauch C., Reurings F., Tuomisto F., Veal T.D., McConville C.F., Lu H., Schaff W.J., Gallinat C.S., Koblmüller G. *et al.*, *Physica Status Solidi (A)*, **207** (2010) 1083.

[71] Reurings F., Tuomisto F., Egger W., Löwe B., Ravelli L., Sojak S., Liliental-Weber Z., Jones R.E., Yu K.M. *et al.*, *Physica Status Solidi (A)*, **207** (2010) 1087.

[72] Sojak S., Slugen V., Egger W., Ravelli L., Petriska M., Stancek S., Sahul M., Skarba M., Priputen P. *et al.*, *Journal of Physics: Conference Series*, **443** (2013) 012036.

[73] Harms S., Rätzke K., Zaporojtchenko V., Faupel F., Egger W. and Ravelli L., *Polymer*, **52** (2011) 505 .

[74] Harms S., Rätzke K., Faupel F., Chaukura N., Budd P.M., Egger W. and Ravelli L., *The Journal of Adhesion*, **88** (2012) 608.

[75] Cano-Odena A., Vandezande P., Hendrix K., Zaman R., Mostafa K., Egger W., Sperr P., J. De B. and Vankelecom I., *The Journal of Physical Chemistry B*, **113** (2009) 10170.

[76] Li X., Fustin C., Lefevre N., Gohy J., S. De F., J. De B., Egger W. and Vankelecom I., *Journal of Materials Chemistry*, **20** (2010) 4333.

[77] Mariazzi S., DiNoto L., Ravelli L., Egger W. and Brusa R.S., *Journal of Physics: Conference Series*, **443** (2013) 012061.

[78] Ferragut R., Calloni A., Dupasquier A., Consolati G., Quasso F., Giammarchi M.G., Trezzi D., Egger W., Ravelli L. *et al.*, *Journal of Physics: Conference Series*, **225** (2010) 012007.

[79] Szot K., Speier W., Bihlmayer G. and Waser R., *Nature Materials*, **5** (2006) 312.

[80] Mannhart J. and Schlom D., *Science*, **26** (2010) 1607.

[81] Akhtar M., Akhtar Z., Jackson R.A. and Catlow C.R.A., *Journal of the American Ceramic Society*, **78** (1995) 421.

[82] Son J., Moetakef P., Jalan B., Bierwagen O., Wright N., Engel-Herbert R. and Stemmer S., *Nature Materials*, **9** (2010) 482.

[83] Crawford J. and Jacobs P., *Journal of Solid State Chemistry*, **144** (1999) 423.

[84] Mackie R.A., Singh S., Laverock J., Dugdale S.B. and Keeble D.J., *Physical Review B*, **79** (2009) 014102.

[85] Torsti T., Eirola T., Enkovaara J., Hakala T., Havu P., Havu V., Hynlnmaa T., Ignatius J., Lyly M. *et al.*, *Physica Status Solidi B*, **243** (2006) 1016.

[86] Ohnishi T., Lippmaa M., Yamamoto T., Meguro S. and Koinuma H., *Applied Physics Letters*, **87** (2005) 241919.

[87] Gentils A., Copie O., Herranz G., Fortuna F., Bibes M., Bouzehouane K., Jacquet E., Carretero C., Basletic M. *et al.*, *Physical Review B*, **81** (2010) 144109.

[88] Uedono A., Shimoyama K., Kiyohara M., Chen Z.Q., Yamabe K., Ohdaira T., Suzuki R. and Mikado T., *Journal of Applied Physics*, **91** (2002) 5307.

[89] Zanatta M., *Vibrational dynamics in strong glasses: the cases of densified v-SiO_2 and v-$SiSe_2$*. Ph.D. thesis, Universitá degli Studi di Trento (2011).

[90] Elliot S., *Nature*, **354** (1991) 445.

[91] Bochert D., *Optimierte Analyse von Lebenszeitspektren aus Positronenstrahlsystemen*. Master's thesis, Universität der Bundeswehr München (2004).

[92] Kansy J., *Nuclear Instruments and Methods in Physics Research Section A: Accelerators, Spectrometers, Detectors and Associated Equipment*, **374** (1996) 235.

[93] Elliott S., *Physical Review Letters*, **67** (1991) 711.

[94] Inamura Y., Arai M., Otomo T., Kitamura N. and Buchenau U., *Physica B: Condensed Matter*, **284** (2000) 1157.

[95] Polity A., Huth S. and Lausmann M., *Physical Review B*, **59** (1999) 10603.

[96] Istratov A.A. and Vyvenko O.F., *Review of Scientific Instruments*, **70** (1999) 1233.

[97] Mäkinen J., Palko S., Martikainen J. and Hautojärvi P., *Journal of Physics: Condensed Matter*, **4** (1992) L503.

[98] Coleman P.G., Albrecht L., Jensen K.O. and Walker A.B., *Journal of Physics: Condensed Matter*, **4** (1992) 10311.

[99] Dahl D. and Delmore J., *Idaho National Engeneering Laboratory.*

[100] Agostinelli S. *et al.*, *Nuclear Instrument and Methods in Physics Research A*, **506** (2003) 250, URL `http://geant4.cern.ch/`.

[101] Allison J. *et al.*, *IEEE Transactions on Nuclear Science*, **53** (2006) 270.

[102] *Comsol multiphysics* ©. URL `http://www.comsol.com`.

[103] Ravelli L., Löwe B., Egger W., Kögel G., Sperr P. and Dollinger G., *Journal of Physics: Conference Series*, **443** (2013) 012096.

[104] Dryzek J. and Horodek P., *Nuclear Instrument and Methods in Physics Research B*, **266** (2008) 4000.

[105] Sempau J., Fernndez-Varea J., Acosta E. and Salvat F., *Nuclear Instruments and Methods in Physics Research B*, **207** (2003) 107.

[106] Hegewisch, *Firma Hegewisch, Garching.*

[107] Kirkegaard P. and Eldrup M., *Computer Physics Communications.*

List of publications

1. Structural evolution and medium range order in permanently densified vitreous SiO_2
   M. Zanatta, G. Baldi, R.S. Brusa, W. Egger, A. Fontana, E. Gilioli, S. Mariazzi, G. Monaco, **L. Ravelli**, F. Sacchetti,
   Physical Review Letters **112** (2014) 045501.
2. Geant4 simulation of the effect of backscattered positrons on the lifetime spectra of PLEPS
   L. Ravelli, B. Löwe, W. Egger, G. Kögel, P. Sperr, G. Dollinger,
   Journal of Physics: Conference Series **443** (2013) 012096.
3. Study of Positronium formation in nano-channelled silicon as a function of sample temperature
   S. Mariazzi, L. DiNoto, **L. Ravelli**, W. Egger, R.S. Brusa,
   Journal of Physics: Conference Series **443** (2013) 012061.
4. Development of a new time and position resolving detector for the pulsed low energy positron system PLEPS
   U. Ackermann, W. Egger, P. Sperr, B. Löwe, **L. Ravelli**, G. Kögel, G. Dollinger, O. Jagutzki,
   Journal of Physics: Conference Series **443** (2013) 012095.
5. PLEPS study of ion implanted and annealed $Fe - 11.62\%Cr$ alloys
   S. Sojak, V. Slugen, W. Egger, **L. Ravelli**, M. Petriska, S. Stancek, M. Sahul, M. Skarba, P. Priputen, M. Stacho, J. Veternikova, R. Hinca, V. Sabelova,
   Journal of Physics: Conference Series **443** (2013) 012036.
6. Surfaces of colloidal PbSe nanocrystals probed by thin-film positron annihilation spectroscopy
   L. Chai, W. Al-Sawai, Y. Gao, A.J. Houtepen, P.E. Mijnarends, B. Barbiellini, H. Schut, L.C. van Schaarenburg, M.A. van Huis, **L. Ravelli**, W. Egger, S. Kaprzyk, A. Bansil, S.W.H. Eijt,
   Applied Physics Letters Materials **1** (2013) 022111.
7. Niobium aggregation and vacancylike defect evolution in

nanostructured Nb-doped Mg: Their role in the kinetics of the hydride-to-metal phase transformation
C. Macchi, Maurizio, C. , R. Checchetto, S. Mariazzi, **L. Ravelli**, W. Egger, P. Mengucci, N. Bazzanella, A. Miotello, A. Somoza, R.S. Brusa,
Physical Review B **85** (2012) 214117.

8. Characterization of vacancy-type defects in heteroepitaxial GaN grown by low-energy plasma-enhanced vapor phase epitaxy
A. Calloni, R. Ferragut, A. Dupasquier, H. von Känel, A. Guiller, A. Rutz, **L. Ravelli**, W. Egger,
Journal of Applied Physics **112** (2012) 024510.
9. Aging and Free Volume in a Polymer of Intrinsic Microporosity (PIM-1)
S. Harms, K. Rätzke, F. Faupel, N. Chaukura, P.M. Budd, W. Egger, **L. Ravelli**,
The Journal of Adhesion **88** (2012) 608.
10. Different chromium content and thermal annealing influence on ions implanted Fe-Cr model alloys
S. Sojak, V. Slugen, V. Krsjak, W. Egger, **L. Ravelli**, M. Petriska, S. Stancek, M. Skarba, P. Priputen, K. Vitazek, M. Stacho, J. Veternikova, V. Sabelova,
Physics Procedia **35** (2012) 80.
11. Enhanced kinetics of hydride-metal phase transition in magnesium by vacancy clustering
R. Checchetto, N. Bazzanella, A. Kale, A. Miotello, S. Mariazzi, R.S. Brusa, P. Mengucci, C. Macchi, A. Somoza, W. Egger, **L. Ravelli**,
Physical Review B **84** (2011) 054115.
12. Vacancy defects in CdTe thin films
D.J. Keeble, J.D. Major, **L. Ravelli**, W. Egger, K. Durose,
Physical Review B **84** (2011) 174122.
13. Suppression of vacancy defects in epitaxial La-doped $SrTiO_3$ films
D.J. Keeble, B. Jalan, **L. Ravelli**, W. Egger, G. Kanda, S. Stemmer,
Applied Physics Letters **99** (2011) 232905.
14. Free volume distribution at the Teflon AF©/silicon interfaces probed by a slow positron beam
S. Harms, K. Rätzke, V. Zaporojtchenko, F. Faupel, W. Egger, **L. Ravelli**,
Polymer **52** (2011) 505.
15. Layer-resolved study of the Mg to MgH2 transformation in Mg–Ti films with short-range chemical order

S.W.H. Eijt, H. Leegwater, H. Schut, A. Anastasopol, W. Egger, **L. Ravelli**, C. Hugenschmidt, B. Dam,
Journal of Alloys and Compounds **509** (2011) S567.

16. Identification of A- and B-site cation vacancy defects in perovskite oxide thin film
D. J. Keeble, S. Wicklein, R. Dittmann, **L. Ravelli**, R. A. Mackie, W. Egger,
Physical Review Letters **105** (2010) 226102.
17. Study of defects in implanted silica glass by depth profiling Positron Annihilation Spectroscopy
R.S. Brusa, S. Mariazzi, **L. Ravelli**, P. Mazzoldi, G. Mattei, W. Egger, C. Hugenschmidt, B. Löwe, P. Pikart, C. Macchi, A. Somoza,
Nuclear Instruments and Methods in Physics Research Section B **268** (2010) 3186.
18. Positronium formation in porous materials for antihydrogen production
R. Ferragut, A. Calloni, A. Dupasquier, G. Consolati, F. Quasso, M. G. Giammarchi, D. Trezzi, W. Egger, **L. Ravelli**, M. P. Petkov, S. M. Jones, B. Wang, O. M. Yaghi, B. Jasinska, N. Chiodini, A. Paleari,
Journal of Physics: Conference Series **225** (2010) 012007.
19. Irradiation-induced defects in InN and GaN studied with positron annihilation
F. Reurings, F. Tuomisto, W. Egger, B. Löwe, **L. Ravelli**, S. Sojak, Z. Liliental-Weber, R.E. Jones, K.M. Yu, W. Walukiewicz, W.J. Schaff,
Physica Status Solidi (A) **207** (2010) 1087.
20. In-vacancies in Si-doped InN
C. Rauch, F. Reurings, F. Tuomisto, T.D. Veal, C.F. McConville, H. Lu, W.J. Schaff, C.S. Gallinat, G. Koblmüller, J.S. Speck, W. Egger, B. Löwe, **L. Ravelli**, S. Sojak,
Physica Status Solidi (A) **207** (2010) 1083.
21. Direct evidence by positron annihilation spectroscopy of defect distributions deeper than R_p in Ar^+ implanted silica glass
P. Mazzoldi, G. Mattei, **L. Ravelli**, W. Egger, S. Mariazzi, R.S. Brusa,
Journal of Physics D: Applied Physics **42** (2009) 115418.

Acknowledgements

There are many people that helped me during this year of my Ph.D. and that contributed to this work. In particular I would like to thank:

Prof. Günther Dollinger that accepted me during my Master Thesis's work and afterward for giving me the great opportunity of doing the PhD in a very stimulating environment and in one of the most advanced facilities for positron research worldwide.

My supervisor, Dr. Werner Egger, not only for teaching me a lot about physics and for the patience in answering all my questions, but also for the interesting discussions and tales about almost everything, from history to politics, to soccer. I am very thankful also for the big effort in correcting this work in such a short time.

Dr. Gottfried Kögel and Dr. Peter Sperr for the useful discussions and the precious comments about everything concerning positrons, PLEPS and the physics in general.

Mr. Wolfgang Engl not only for the production and modifications of many of the improved parts of PLEPS described in this work, but also for teaching me a lot of new edible (or at least most of them...) species of mushrooms.

Benjamin Löwe for the great help about all my computer-related questions and for introducing me to Python and Geant4. Thanks to his assistance I managed to perform the simulations described in chapter 6.

Tönjes Koschine (Uni Kiel) who developed the new control software for PLEPS and implemented a lot of new features (and many of them "on the fly" during the beam times) making the optimization work so much easier.

Dr. Christoph Hugenschmidt, Dr. Christian Piochacz and Mr. Sebastian Vohburger for the great help during the beam times and for the dismantling and remounting operation of PLEPS.

All the colleagues of both the Universität der Bundeswehr München (especially Ulrich Ackermann and Marcel Dickmann for the great help during the last beam times) and of NEPOMUC for the useful, interesting discussions and for the nice working atmosphere.

Dr. Aurelie Gentils, Prof. Roberto S. Brusa, Dr. David J. Keeble, Prof.

Dr. Klaus Rätzke, Dr. Marco Zanatta, Tönjes Koschine, and Christian Ohrt for providing such interesting samples and for the fruitful collaboration that ultimately culminated in the measurements illustrated in sections 4.1, 4.2 and 7.2. Obviously also all the other users are gratefully acknowledged.

Ms Martina Falter for the great help in the solution of bureaucratic issues of all kind.

My family for giving me the possibility of studying this fascinating, but sometimes also *very* complicated subject, that is physics. Without their encouragement this entire work would have been not possible.

Last, but not least. My beloved Sara, not only for the love and support during these four and a half years, but also for the invaluable help in the revision of the bibliography and for the modification of figure 6.6.